Spin-orbit interaction in ballistic nanowire devices

Kammhuber, Jakob

Important note
To cite this publication, please use the final published version (if applicable).
Please check the document version above.

SPIN-ORBIT INTERACTION IN BALLISTIC NANOWIRE DEVICES

SPIN-ORBIT INTERACTION IN BALLISTIC NANOWIRE DEVICES

Proefschrift

ter verkrijging van de graad van doctor
aan de Technische Universiteit Delft,
op gezag van de Rector Magnificus prof. ir. K.C.A.M. Luyben,
voorzitter van het College voor Promoties,
in het openbaar te verdedigen op vrijdag 16 Juni 2017 om 12:30 uur

door

Jakob KAMMHUBER

Master of Science in Physics,
Eidgenössische Technische Hochschule (ETH) Zürich, Zwitserland,
geboren te Burghausen, Duitsland.

Dit proefschrift is goedgekeurd door de promotor:

Prof. dr. ir. L. P. Kouwenhoven

Samenstelling promotiecommissie:

Rector Magnificus,	Voorzitter
Prof. dr. ir. L. P. Kouwenhoven	Technische Universiteit Delft, promotor

Onafhankelijke leden:

Prof. dr. ir. L. M. K. Vandersypen	Technische Universiteit Delft
Prof. dr. J. M. van Ruitenbeek	Universiteit Leiden
Prof. dr. D. Loss	University of Basel
Dr. A. F. Otte	Technische Universiteit Delft
Prof. dr. Y. M. Blanter,	Technische Universiteit Delft, reservelid

Overige leden:

Dr. M. T. Wimmer	Technische Universiteit Delft

'T ain't what you do, it's the place that you do it,
'T ain't what you do, it's the time that you do it,
'T ain't what you do, it's the way that you do it,
That's what gets results!

James "Trummy" Young & Sy Oliver

CONTENTS

Similar to their charge, electrons also posses an intrinsic magnetic moment called spin. When moving through an electric field, electrons experience and effective magnetic field in their restframe which will interact with the spin and influence its direction. This spin-orbit interaction creates a measurable shift in the splitting of atomic energy levels and in the energy bands of solid state systems. Recently it has been proposed that systems with strong spin-orbit interaction can be used to engineer novel topological states of matter which are predicted to host non-abelian quasi particles. These could generate robust quantum states which are protected against decoherence. The research in this thesis focuses on indium antimonide (InSb) nanowires which combine exceptionally strong spin-orbit interaction with large g-factors and high electron mobilities. This makes them one of the most promising systems for realizing topological qubits based on Majorana zero modes (MZM).

At the start of this thesis, the quality of such InSb nanowire devices is studied and improved. Because of their reduced dimensionality, nanowires have a large surface to volume ratio and can be very sensitive to the environment. The choice of gate dielectric, surface adsorbents and the nanowire contact interface all have a strong influence on the final device quality. Following these results, environmental noise is minimized to demonstrate ballistic electron transport through nanowire quantum point contacts (QPC). Measurements of the evolution of individual subbands in a magnetic field reveal the strong influence of orbital effects and demonstrate the emergence of an orbital degeneracy at finite magnetic field. Next nanowire QPCs are used to search for a helical gap, one of the main building blocks for engineering MZMs. Because the experimental visibility of the helical gap depends strongly on device geometry it has so far not been observed unambiguously. By combining the correct thickness of gate dielectric with systematic variations in the QPC length, we are able to detect signatures of a helical state in conductance measurements. Additionally we study the evolution in a linear and rotating magnetic field, which allows us to clearly attribute our experimental signatures to spin-orbit interaction and to exclude other effects. The extracted spin-orbit energy of 6.5 meV is significantly stronger than the values extracted in earlier experiments.

The final part of the thesis focuses on interactions between microwave radiation and mesoscopic systems. Coplanar superconducting microwave resonators are an attractive platform for these measurements because of their small mode volume, high quality factors and established fabrication process. Precise positioning of InSb nanowires close to the electric field antinodes of a resonator maximizes the electric field along the wire without compromising the intrinsic quality factor of the cavity. A double quantum dot inside the nanowire then interacts with the microwave field through its dipole moment at a charge cavity coupling rate $g_c = 150$ MHz which is larger than most comparable experiments. In a very similar experiment, the nanowire double dot is replaced by a superconducting Josephson junction. A dc voltage bias applied across the junction

provides a source of microwave photons, and non-linearities in the circuit allows for efficient down-conversion of higher order Josephson frequencies to the fundamental cavity mode. Embedded inside a cavity this provides a coherent source of microwave radiation which is easy to fabricate and can be integrated on-chip.

Both experimental systems studied in this thesis are important building blocks in proposals for topological qubits based on Majorana zero modes. Beyond that they also demonstrate significant progress in the control and quality of nano-structures and pave the way towards several interesting follow-up experiments. Some suggestions for such experiments are given in the final chapter of this thesis.

SAMENVATTING

Net als elektrische lading bezitten elektronen een intrinsiek magnetisch moment genaamd spin. Wanneer elektronen door een elektrisch veld bewegen, ondervinden deze een effectief magnetisch veld in hun referentiekader dat koppelt aan het magnetisch moment en de richting van het elektron zal beïnvloeden. Deze spin-baaninteractie creëert een meetbare verschuiving in de splitsing van atomische energiebanden in vaste stoffen. Recentelijk is voorgesteld dat systemen met sterke spin-baankoppeling gebruikt kunnen worden om een nieuwe topologische toestand in materialen tot stand te brengen. Er is voorspeld dat deze topologische toestand plaats kan bieden aan niet-Abelse quasideeltjes, die robuuste kwantumtoestanden genereren die beschermd zijn tegen decoherentie. Het onderzoek in dit proefschrift richt zich op indiumantimonide (InSb) nanodraden, waarin een buitengewoon sterke spin-baankoppeling met hoge g-factor en hoge elektronmobiliteit samenkomen. Dit maakt het een van de meest veelbelovende systemen om topologische qubits te realiseren die gebaseerd zijn op Majorana-quasideeltjes.

Voor dit proefschrift is als eerste de kwaliteit van zulke InSb-nanodraadapparaten bestudeerd en verbeterd. Vanwege de nagenoeg 1-dimensionale aard van de nanodraden is de oppervlakte/volume-verhouding groot, met een gevoeligheid voor de omgeving tot gevolg. De materiaalkeuze voor gate-elektrode-diëlectrikum, de keuze voor gebruikte absorberende stoffen en de aansluiting van het contact op de nanodraad zijn allen van grote invloed op de uiteindelijke kwaliteit van het apparaat. Naar aanleiding van de resultaten minimaliseren we de omgevingsruis en demonstreren we ballistisch elektronentransport door nanodraad-kwantumpuntcontacten (nanodraad-QPC). Metingen van de evolutie van individuele elektrische subbanden in een magnetisch veld tonen de grote invloed van spin-baankoppelingeffecten en laten het ontstaan van meervoudige ontaarding bij eindige magneetvelden zien. Vervolgens zijn nanodraad-QPC's gebruikt in de zoektocht naar een helische energiekloof, een van de hoofdingrediënten voor het tot stand brengen van Majorana-quasideeltjes. Omdat de experimentele zichtbaarheid van de helische energiekloof sterk afhangt van het ontwerp van de chip, was deze tot op heden nog niet onomstotelijk aangetoond. Door de juiste dikte van gate-elektrode-diëlectrikum te combineren met een systematische variatie in QPC-lengte, hebben we tekens van de helische toestand kunnen detecteren in geleidingsmetingen. Daarnaast bestuderen we de evolutie van de toestand in een lineair magnetisch veld onder rotatie. Dit stelt ons in staat om de signalen ontegenzeggelijk toe te wijzen aan spin-baaninteractie en overige oorzaken uit te sluiten. Bovendien is de uit de metingen onttrokken spin-baaninteractie van 6.5 meV is significant sterker dan voorgaande literatuurwaardes.

Het laatste deel van dit proefschrift onderzoekt de interactie tussen microgolfradiatie en mesoscopische systemen. Supergeleidende coplanaire golfgeleiderresonatoren in het microgolfregime bieden een aantrekkelijk platform voor deze metingen vanwege hun smalle lijnbreedte, hoge kwaliteitsfactoren en het bewezen fabricageproces. Pre-

cieze positionering van de InSb-nanodraad bij een van de maxima van het elektrisch veld vergroot het elektrisch veld over de draad zonder de intrinsieke kwaliteitsfactor van de resonator te verminderen. Bij het tot stand brengen van een dubbele kwantumdot in de nanodraad is er interactie met het elektromagnetisch veld via het dipoolmoment opgewekt tussen beide dots. Een lading-holtekoppeling van $g_C = 150$ MHz is bereikt, welke groter is dan de meeste vergelijkbare experimenten. In een zeer vergelijkbaar experiment is de nanodraad met dubbele kwantumdot vervangen door een supergeleidende Josephson-junctie. Een gelijkspanning aangebracht over de junctie genereert een bron van microgolf-fotonen, waarbij niet-lineariteiten in het circuit efficiënte conversie van de boventonen van de Josephson-junctie naar de grondtoon van de resonator mogelijk maken. Geïntegreerd in een microholte, leidt dit tot coherente emissie van microgolf-licht die makkelijk en *on-chip* te fabriceren is. Beide experimentele systemen bestudeerd in dit proefschrift zijn belangrijke bouwstenen in voorstelde ontwerpen tot topologische qubits, gebaseerd op Majorana-quasideeltjes. Bovendien demonstreren ze significante vooruitgang in de beheersing en kwaliteit van nanostructuren, waardoor een weg is vrijgemaakt voor verscheidene interessante vervolgexperimenten. Enkele suggesties voor zulke vervolgexperimenten worden benoemd in het laatste hoofdstuk van dit proefschrift.

1

INTRODUCTION

1

1.1. MORE IS DIFFERENT

The 20th century has revolutionized our understanding of the physical world. The laws of quantum mechanics were developed to describe the behavior of particles at very small scales and those laws predicted many counterintuitive phenomena such as superposition, entanglement and the particle-wave duality. Initially, these predictions created large debates but by now, they have been confirmed with extreme accuracy. State of the art experiments can routinely create, manipulate and entangle quantum states and many researchers work on translating this progress into new quantum technologies.

The theoretical understanding of such experiments typically works well for systems involving only a small number of particles. Descriptions of larger systems such as complicated molecules quickly become very complicated. In condensed matter systems, the number of particles $\sim 10^{22}$ is so extremely large that finding exact solutions becomes impossible. Nevertheless, many theories have been able to realistically describe physical systems even though they involve great simplifications. One prominent example of such a theory is the electronic band structure of solids, pioneered by Felix Bloch [1]. It considers a single electron moving through the electric potential of a infinite periodic crystal. If the individual atoms in the crystal are close enough, the individual atomic energy levels overlap and merge into continuous energy bands which can be interrupted by forbidden energy ranges, as illustrated in Fig. 1.1. This theory gives a strongly simplified description and ignores most microscopic details, yet it successfully explains the optical and electrical properties of many different materials. More complex materials such as amorphous solids, or systems with strong correlations, go beyond the validity of band structure models and are much more difficult to describe correctly. This does not only mean that it is hard to get quantitative prediction of individual material properties. Often such materials can be the source of entirely new and surprising behaviors which require a completely new understanding. This phenomenon of newly emergent behavior was discussed by Phillip Anderson in his article *'More is different'* [2]:

> *"The behavior of large and complex aggregates of elementary particles, it turns out, is not to be understood in terms of a simple extrapolation of the properties of a few particles. Instead, at each level of complexity entirely new properties appear, and the understanding of the new behaviors requires research which I think is as fundamental in its nature as any other."*

One of the main examples Anderson uses to support his argument is Landaus theory of phase transitions. The theory showed that different phases of matter can be classified by understanding the symmetries of each system and that phase transitions are related to spontaneously broken symmetries. The predicted behavior close to phase transitions applies to a large variety of systems because it is purely based on local symmetries, without relying on the microscopic origin of those symmetries. Over the past decades however, it has become clear that despite its almost universal applicability, Landaus theory is not enough. A completely new theory has emerged which classify different states of matter through topology.
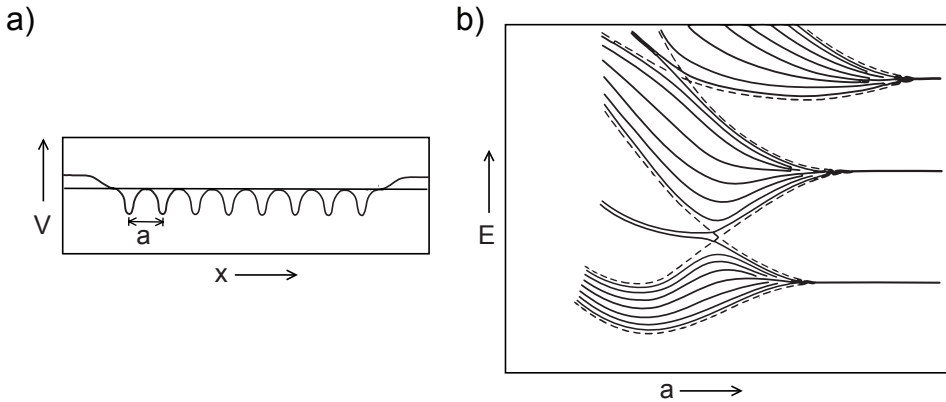
Figure 1.1: Electron band structure of a 1D atom chain. **a)** Atoms distributed evenly along x-direction with spacing a produce a periodic potential V. **b)** At decreasing spacing a the discrete energy levels of individual atoms overlap and merge into continuous energy bands. Figure adapted from references 3 and 4.

1.2. TOPOLOGICAL STATES OF MATTER

One of the first experimental examples of a topological phase transition emerged from the discovery of the quantum Hall effect and its extremely precise quantization [5]. It was realized [6, 7] that the quantization is closely related to the chern-number C, which is a topological invariant that can only take integer values. This developed into a entirely new way of classifying matter through the topology of their bandstructure. Two phases are considered topologically equivalent, if their Hamiltonians can be continuously transformed into one another without closing any energy gaps. Phase transitions between two different topological states are accompanied by a closing and reopening of an energy gap and they are possible, even if all symmetries are conserved. Most known materials, however, are topologically trivial. This started a long search for new systems which could exhibit non-trivial phases [8–10].

1.3. TOPOLOGICAL SUPERCONDUCTORS

A non-trivial topological state has also been predicted for superconductors with p-wave symmetry. These may host solid state representations of Majorana fermions. Unfortunately however, no existing materials with p-wave superconductivity are known. In 2008 L. Fu and C. Kane, realized that topological superconductors could also be engineered by combining a topological insulator with a conventional s-wave superconductor [11]. Soon after that in 2010, two different proposals were presented which simplified the design even more [12, 13]. The combination of a superconductor with spin-orbit interaction in a magnetic field, can drive a topological phase transition and create a region with inverted band structure and localized Majorana zero modes at its ends. Because in two dimensions, such Majorana modes are predicted to possess non-abelian exchange statistics [14] they could be used to create topological qubits, which suppress decoherence by storing information non-locally [15]. The strong intrinsic spin-orbit interaction

a) $B < B_C$
trivial

b) $B = B_C$
transition

c) $B > B_C$
non-trivial

d)
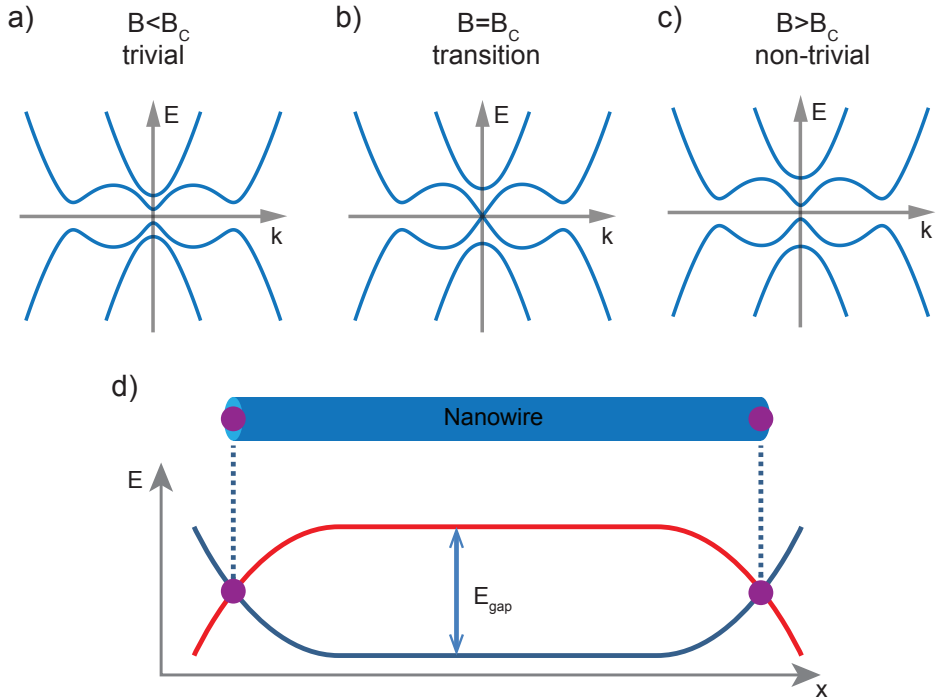
Figure 1.2: **a)** The combination of spin-orbit interaction and superconductivity produce a subband structure which is symmetric and gapped around E_F. **b)** When the magnetic field is increased to B_C the energy gap closes at $k = 0$. **c)** At $B > B_C$ the band gap reopens and the system transitions to a topologically non trivial state with inverted bandstructure. **d)** In the topological phase the inverted energy bands cross back to their trivial non inverted state at each end of the nanowire and Majorana zero modes emerge at the band crossing. Figure adapted from reference 19

of InAs and InSb makes them very promising candidates to engineer MZMs and existing fabrication techniques had already demonstrated induced superconductivity. Therefore experimental evidence of Majorana zero modes followed quickly after the first proposals [16–18].

1.4. OUTLINE OF THIS THESIS

This thesis focuses on different building blocks which are necessary to transition from the initial MZM signatures to a working topological Qubit.

- Chapter 2 briefly introduces the theoretical background required for the experimental chapters. It starts with a description of conductance quantization in quantum point contacts and explains how this quantization is modified in the presence of spin-orbit interaction. Additionally it describes the basic properties of quantum dots and their interaction with a microwave cavity.

- Chapter 3 describes the most important fabrication and measurement techniques used in this thesis.

- Chapter 4 discusses the influence of the nanowire environment, fabrication and post-processing on the final device quality.

- Chapters 5 and 6 are strongly related. The demonstration of ballistic transport in nanowire quantum point contacts in chapter 5 is a basic requirement to demonstrate transport through a helical gap, which is presented in chapter 6.

- Chapter 7 uses a superconducting microwave resonator to measure a double quantum dot in an InSb nanowire. The high sensitivity of these measurements demonstrates the advantage of microwave measurements which could be essential to read out topological Majorana qubits.

- Chapter 8 demonstrates the coherent emission of microwave radiation from a Josephson junction embedded inside a microwave cavity. As an on-chip microwave source it can be extremely useful for read-out and control of classical as well as topological qubits.

- Chapter 9 summarizes and discusses the experimental results and proposes future experiments.

REFERENCES

[1] F. Bloch, "Über die Quantenmechanik der Elektronen in Kristallgittern," *Zeitschrift für Physik A: Hadrons and Nuclei*, vol. 52, no. 7, pp. 555–600, 1929.

[2] P. W. Anderson *et al.*, "More is different," *Science*, vol. 177, no. 4047, pp. 393–396, 1972.

[3] C. Beenakker, "Search for majorana fermions in superconductors," *Annu. Rev. Condens. Matter Phys.*, vol. 4, no. 1, pp. 113–136, 2013.

[4] W. Shockley, "On the surface states associated with a periodic potential," *Physical review*, vol. 56, no. 4, p. 317, 1939.

[5] K. v. Klitzing, G. Dorda, and M. Pepper, "New method for high-accuracy determination of the fine-structure constant based on quantized hall resistance," *Physical Review Letters*, vol. 45, no. 6, p. 494, 1980.

[6] R. B. Laughlin, "Quantized hall conductivity in two dimensions," *Physical Review B*, vol. 23, no. 10, p. 5632, 1981.

[7] D. Thouless, M. Kohmoto, M. Nightingale, and M. Den Nijs, "Quantized hall conductance in a two-dimensional periodic potential," *Physical Review Letters*, vol. 49, no. 6, p. 405, 1982.

[8] M. Z. Hasan and C. L. Kane, "Colloquium: topological insulators," *Reviews of Modern Physics*, vol. 82, no. 4, p. 3045, 2010.

[9] S.-Y. Xu, I. Belopolski, N. Alidoust, M. Neupane, G. Bian, C. Zhang, R. Sankar, G. Chang, Z. Yuan, C.-C. Lee, *et al.*, "Discovery of a weyl fermion semimetal and topological fermi arcs," *Science*, vol. 349, no. 6248, pp. 613–617, 2015.

[10] L. Lu, Z. Wang, D. Ye, L. Ran, L. Fu, J. D. Joannopoulos, and M. Soljačić, "Experimental observation of weyl points," *Science*, vol. 349, no. 6248, pp. 622–624, 2015.

[11] L. Fu and C. L. Kane, "Superconducting proximity effect and majorana fermions at the surface of a topological insulator," *Physical review letters*, vol. 100, no. 9, p. 096407, 2008.

[12] R. M. Lutchyn, J. D. Sau, and S. D. Sarma, "Majorana fermions and a topological phase transition in semiconductor-superconductor heterostructures," *Physical review letters*, vol. 105, no. 7, p. 077001, 2010.

[13] Y. Oreg, G. Refael, and F. von Oppen, "Helical liquids and majorana bound states in quantum wires," *Physical review letters*, vol. 105, no. 17, p. 177002, 2010.

[14] A. Stern, "Non-abelian states of matter," *Nature*, vol. 464, no. 7286, pp. 187–193, 2010.

[15] C. Nayak, S. H. Simon, A. Stern, M. Freedman, and S. D. Sarma, "Non-abelian anyons and topological quantum computation," *Reviews of Modern Physics*, vol. 80, no. 3, p. 1083, 2008.

[16] V. Mourik, K. Zuo, S. M. Frolov, S. R. Plissard, E. P. A. M. Bakkers, and L. P. Kouwenhoven, "Signatures of majorana fermions in hybrid superconductor-semiconductor nanowire devices," *Science*, vol. 336, no. 6084, pp. 1003–1007, 2012.

[17] H. O. H. Churchill, V. Fatemi, K. Grove-Rasmussen, M. T. Deng, P. Caroff, H. Q. Xu, and C. M. Marcus, "Superconductor-nanowire devices from tunneling to the multichannel regime: Zero-bias oscillations and magnetoconductance crossover," *Phys. Rev. B*, vol. 87, p. 241401, Jun 2013.

[18] S. M. Albrecht, A. Higginbotham, M. Madsen, F. Kuemmeth, T. S. Jespersen, J. Nygård, P. Krogstrup, and C. Marcus, "Exponential protection of zero modes in majorana islands," *Nature*, vol. 531, no. 7593, pp. 206–209, 2016.

[19] K. Zuo and V. Mourik, *Signatures of Majorana Fermions in Hybrid Superconductor-Semiconductor Nanowire Devices*. PhD thesis, TU Delft, Delft University of Technology, 2016.

2

THEORY

This chapter introduces the underlying theoretical concepts of the experimental results presented the in the later chapters. It begins with a short introduction to spin-orbit coupling in semiconductors, followed by a description of conductance quantization in ballistic one dimensional systems. The presence of spin-orbit coupling modifies the electron dispersion in a ballistic system which creates a clear experimental signature under the right conditions. The final part introduces quantum dots, narrow islands confined in all three dimensions. Embedded inside a microwave cavity, quantum dots strongly influence the transmission through the cavity.

2.1. SPIN-ORBIT INTERACTION

Spin-orbit interaction (SOI) couples the motion of electrons with the orientation of their spin. It was originally discovered in atomic physics to explain energy shifts of valence electrons in spectroscopy experiments. Electrons moving in the electric field of an atom experience an effective magnetic field $\vec{B}$ in their rest frame, which is oriented perpendicular to the electrons velocity ($\vec{v}$) and the electric field $\vec{E}$

$$\vec{B} = -\frac{1}{c^2}\vec{v} \times \vec{E}. \tag{2.1}$$

This leads to an energy shift which can be derived from a nonrelativistic approximation of the Dirac equation [1, 2]

$$H_{SO} = -\frac{\hbar}{4m_0^2 c^2}\sigma \cdot p \times (\nabla V_0), \tag{2.2}$$

with m_0 the free electron mass, c the speed of light, $\sigma = (\sigma_x, \sigma_y, \sigma_z)$ the pauli spin matrices, p the momentum operator and V_0 the electric potential of the atom core. This includes the Thomas factor 1/2 which renormalizes the SOI due to relativistic effects. Because the interaction strength depends on the gradient of the electric potential it increases with the mass of the nucleus and heaver elements have stronger SOI.

2.1.1. SOI IN SEMICONDUCTORS

Similar to the orbits of single atoms, electrons moving through the crystal lattice of a solid can also experience SOI. To understand how it arises in semiconductors we look at the energy bands of electrons $E(k)$ and some simple symmetry considerations. If spin and momentum are independent the energy will only depend on momentum and electron spin is not a good quantum number,

$$E(k) = E_\downarrow(k) = E_\uparrow(k). \tag{2.3}$$

This degeneracy arises from the combination of two different symmetries [3]. The conservation of time reversal symmetry, giving $E_\uparrow(k) = E_\downarrow(-k)$ together with the conservation of inversion symmetry in the crystal lattices, giving $E_{\uparrow,\downarrow}(k) = E_{\uparrow,\downarrow}(-k)$. Breaking of time reversal symmetry, for example with an external magnetic field, defines a spin quantization axis and splits electrons of opposite spin by the Zeeman energy. Similarly, broken inversion symmetry creates a non vanishing electric field which transforms into a momentum dependent magnetic field $B_{SO}(k)$ in the rest frame of an electron. $B_{SO}(k)$ also defines a spin quantization axis, with changing direction at different spatial position and for different electron momentum. Importantly, electrons of opposite spin are still degenerate if time reversal symmetry is conserved. SOI is therefore expected to emerge in any semiconductor with broken inversion symmetry and there are two different ways how it can be broken, each giving rise to a specific type of SOI. The first type, called Dresselhaus SOI [4] is caused by bulk inversion asymmetry in crystals which lack a center of inversion in their unit cell for example in zinc-blende or wurtzite crystals. The full Hamiltonian of Dresselhaus SOI in bulk crystals has cubic dependence on the wave vector [2, 4] but in two-dimensional (2D) electron systems this reduces to a linear term:

$$H_D^{2D} = \beta_D \cdot \left(k_x \sigma_x - k_y \sigma_y\right). \tag{2.4}$$

$\sigma_{x,y,z}$ are the Pauli matrices and $k_{x,y}$ the electron wave vector. The Dresselhaus parameter β_R is material dependent and characterizes the strength of the spin-orbit interaction. The second type, Rashba SOI, emerges due to structural inversion asymmetry (SIA) [5] for example through asymmetries of the electron confinement potential or through asymmetric external electric fields. In 2D it is also linear with $k_{x,y}$ and described by:

$$H_R^{2D} = \alpha_R \cdot \left(k_x \sigma_y - k_y \sigma_x \right). \tag{2.5}$$

The Rashba coupling constant α_R is also material specific and tunable with an external electric field. Both Dresselhaus in Rashba SOI appear independently or in combination and cancel each other or add up in strength, depending on the sign of β_D and α_R. Quantitative estimates of their relative strength can be calculated with tight binding models or $\mathbf{k} \cdot \mathbf{p}$ theory [2] and similar to atomic physics heavier elements, in particular InAs and InSb, are expected to have stronger SOI . It is also possible to define an energy E_{SO} and length l_{SO} related to the strength of SOI, for example for Rashba SOI:

$$l_{SO} = \frac{\hbar^2}{m\alpha_R} \tag{2.6}$$

$$E_{SO} = \frac{m\alpha_R^2}{2\hbar^2} \tag{2.7}$$

2.1.2. SOI IN INSB NANOWIRES

One of the main reasons our group is working with InSb is its exceptionally strong spin-orbit interaction [2]. Our nanowires grow with zinc-blende crystal structure [6] and are expected to have a combination of both Dresselhaus and Rashba interaction. Typically we focus on Rashba interaction because of the strong tunability with electric field. Often it is assumed that Dresselhaus SOI is negligible in our nanowires since it is expected to vanish for electrons moving in the [111] crystal direction [2] along which our nanowires are grown. However, this approximation is only strictly true in two dimensional systems and the confinement down to one dimension could cause the reemergence of a finite Dresselhaus component.The Rashba Hamiltonian in a 1D nanowire extending along x-direction reduces to

$$H_R^{1D} = \alpha_R p_x \sigma_y. \tag{2.8}$$

This induces a spin-orbit field B_{SO} perpendicular to the electric field and the electron momentum

$$B_{SO} \propto \alpha_R (\vec{k}_x \times \vec{E}). \tag{2.9}$$

2.2. CONDUCTANCE QUANTIZATION

Quantization of conductance is a classical example how, at nanoscale dimensions, electron transport is influenced by quantum effects. It was first observed in 1989 in GaAs 2DEGs [7, 8] and has, since then, become a fundamental tool for studying mesoscopic structures. Measurements of Quantum Point Contacts (QPC) have been done in many different material systems [9–11] and most of the theory behind QPCs is understood very
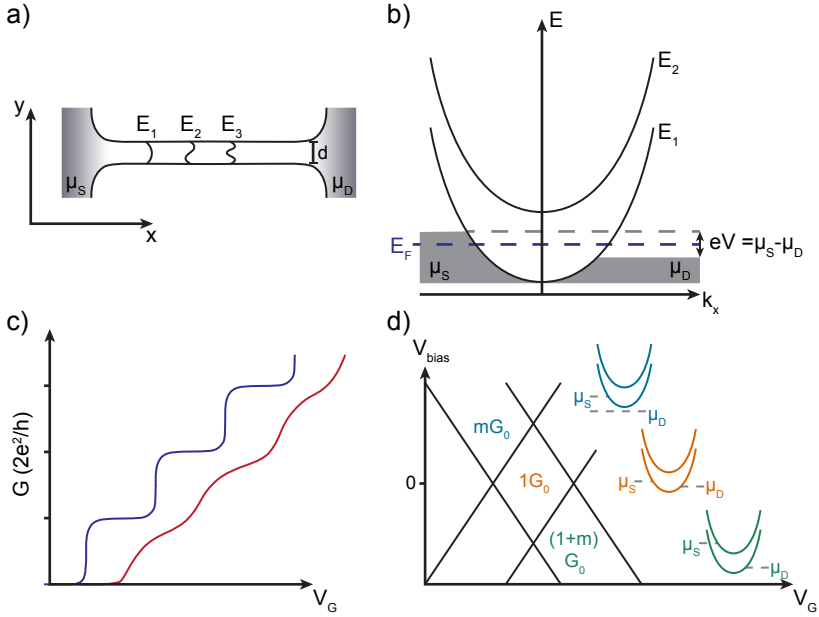
Figure 2.1: **a)** 1D wire of width d and length L connected to source and drain contacts with chemical potential μ_D and μ_S. Electron motion is ballistic along x and confinement along y gives discrete transverse modes E_n. **b)** Energy dispersion for electrons in a) with quantized subbands parabolic in k_x. Positive (negative) momentum states are filled up to μ_D (μ_S). A voltage $eV = \mu_S - \mu_D$ induces current in the wire. **c)** Sketch of the conductance through the 1D wire for low temperature $4k_bT \ll E_n$ (blue) and high temperature $4k_bT \sim E_n$ (red). **d)** Voltage bias spectroscopy: increasing voltage across the wire gives triangles of constant conductance symmetric around 0. This can be used to extract the subband spacing E_n and gate lever arm ν.

well [12]. However even after more than 25 years of research there are still open questions, in particular about the influence of e-e interactions [13, 14]. QPCs have an important role in this thesis because they are a direct proof of ballistic electron transport, which is essential for the existence of Majorana zero modes [15]. Additionally, deviations from the simple conductance quantization are expected in materials with strong spin-orbit interaction [16]. First we explain the emergence of conductance steps in 1D systems following the Landau-Buttiker formalism [12, 17]. Starting with an idealized system, we then include the influence of finite length, temperature and voltage. We will look at differences between QPCs defined in 2DEGs and QPCs in nanowires as well as the effect of an external magnetic field. Finally, we discuss how the conductance through at QPC is modified in the presence of strong spin-orbit interaction.

2.2.1. CONDUCTANCE THROUGH A LONG 1-DIMENSIONAL CHANNEL

Consider a long channel as depicted in Fig. 2.1a) with length L and width d ($L \gg d$) comparable to the Fermi wavelength λ_F. Ballistic electron motion along x gives an energy dispersion parabolic in k_x and confinement along y creates quantized energy modes of energy E_n. Inside the channel the energy dispersion reduces to n discrete, parabolic

subbands $E_n(k_x)$, each with a 2-fold spin degeneracy:

$$E_n(k_x) = E_n + \frac{\hbar^2 k_x^2}{2m^*},\qquad(2.10)$$

with effective electron mass m^*. If no external voltage is applied states with positive and negative momentum are equally occupied up to the Fermi level E_F. A small voltage V creates an imbalance around E_F, $eV = \mu_S - \mu_D$ which induces a current through the channel [18, 19]

$$I = e \sum_{n=1}^{N} \int_{\mu_S}^{\mu_D} \frac{1}{2} \cdot \rho_n^{1D}(E) \cdot v_n(E) \cdot T_n(E) dE.\qquad(2.11)$$

Here T_n is channel transmission, $v_n = (dE_n/dk_x)/\hbar$ the effective electron velocity and $\rho_n^{1D} = 2/\pi \cdot (dE_n/dk_x)^{-1}$ is the 1D density of states. The energy dependencies of v_n and ρ^{1D} cancel out giving a conductance $G = I/V$

$$G = \frac{2e^2}{h} \sum_{n=1}^{N} T_n(E).\qquad(2.12)$$

If we assume ideal transmission between the contacts and the 1D wire, $T_n(E) = 1$, every occupied subband $E_n(k_x = 0) < E_F$ contributes exactly one conductance quantum $G_0 = 2e^2/h$ to the overall conductance. By changing E_F inside the channel, for example with a local gate, we measure a stepwise increase in conductance whenever E_F aligns with the bottom of a new subband.

2.2.2. FINITE TEMPERATURE AND VOLTAGE

The effect of finite temperature can be included by introducing the Fermi-Dirac distribution $f(E,T) = (1 + exp(\frac{E-\mu}{k_B T}))^{-1}$ into the QPC conductance,

$$G = \frac{2e^2}{h} \sum_{n=1}^{N} \int \frac{df}{dE} T_n(E) dE.\qquad(2.13)$$

Now the sharpness of the conductance steps is given by the width of $df/dE \sim 4k_b T$. At low temperatures $4k_b T << E_n$ the conductance steps will be well resolved. With increasing temperature they smear out until the quantization is lost around $4k_b T \sim E_n$ (Fig. 2.1c)). Similarly, finite bias voltages will also smooth the measured conductance [20]. If, however, the voltage becomes comparable to the subband spacing $eV \sim E_n$ the simple picture described before breaks down and additional plateaus appear in between the integer plateaus at $N \cdot G_0$. This is illustrated in Fig. 2.1d). If the applied voltage $eV = \mu_S - \mu_D$ is large enough the chemical potentials of the contacts can rise (μ_S) or drop (μ_D) over a subband edge. Then the highest subband only has electron states of one momentum occupied giving a conductance quantized to $(N + m) \cdot 2e^2/h$. The parameter m has a value between 0 and 1 depending on the symmetry of the voltage drop across the QPC [21, 22]. This creates diamond shaped region of constant conductance and measurements of the conductance as function of bias and gate voltage allow the extraction of the level spacing of individual subbands as well as the gate lever arm (Fig. 2.1d).

2.2.3. Realistic QPC Potentials

So far we have assumed a long ($d \ll L$) 1D channel with perfect transmission to the leads. For a more realistic model we can set up a Hamiltonian which includes an arbitrary QPC potential $V(x, y)$

$$H = \frac{p^2}{2m^*} + V(x, y).$$
(2.14)

Assuming adiabatic transition from the current leads to the QPC along x, and a parabolic confinement potential along y, $V(y) = 1/2 m^* w_0^2 y^2$, we can explicitly solve the subband energy spacing [18]

$$E_n = \left(n - \frac{1}{2}\right)\hbar w_0 + \frac{\hbar^2 k_x^2}{2m^*}.$$
(2.15)

At low temperatures we also recover our previous result for the conductance

$$G = \frac{2e^2}{h} \sum_{n=1}^{N} T_n(E).$$
(2.16)

The effect of the QPC potential on the conductance is now included in the subband specific and energy dependent transmission coefficient $T_n(E)$, which can cause substantial deviations from the ideal quantization. Smooth profiles provide high transmission for almost all modes, while abrupt profiles create a mode mismatch between energy bands inside and outside the QPC. This increases the chance of backscattering for electrons entering the QPC which reduces the height of the conductance steps. Resonances in the transmission, as well as local defects cause additional dips and peaks within a plateau. The simple parabolic potential provides a good description for gate defined QPCs in 2DEGs and shows that conductance quantization can be preserved even for short QPCs with a length comparable to their width. More complicated gate profiles can describe realistic potential profiles and even include disorder in the QPC channel.

2.2.4. Nanowire QPCs

Most QPC experiments so far have been performed with Gate defined constrictions in 2D electron or hole gases. Those systems all have very strong confinement along the z-direction effectively restricting the carrier motion to the x-y plane. In a QPC the confinement along z and y will be very asymmetric giving two separate axes of quantization. Because of the big difference in the energy spacings, E_n^y and E_l^z, one can neglect the higher modes in z direction. Experimentally the system remains in the ground state E_1^z and only the quantization E_n^y along y is measured. This is different in nanowires. Here the confinement along the z and y axis is comparable and both have to be taken into account. As simple approximation we can assume a cylindrical confinement potential and find analytical solutions. The eigenmodes of such a potential are described by cylindrical Bessel functions. An example of the lowest five subbands is shown in Fig. 2.2a). One key difference compared to the parabolic potential considered before is the subband energy spacing. Instead of subbands with constant energy spacing it is now possible to have additional orbital subband degeneracies, e.g. between subbands E_2, E_3 or E_4, E_5. This new degeneracy is caused by the rotational symmetry and will give conductance steps of $4e^2/h$ instead of $2e^2/h$.
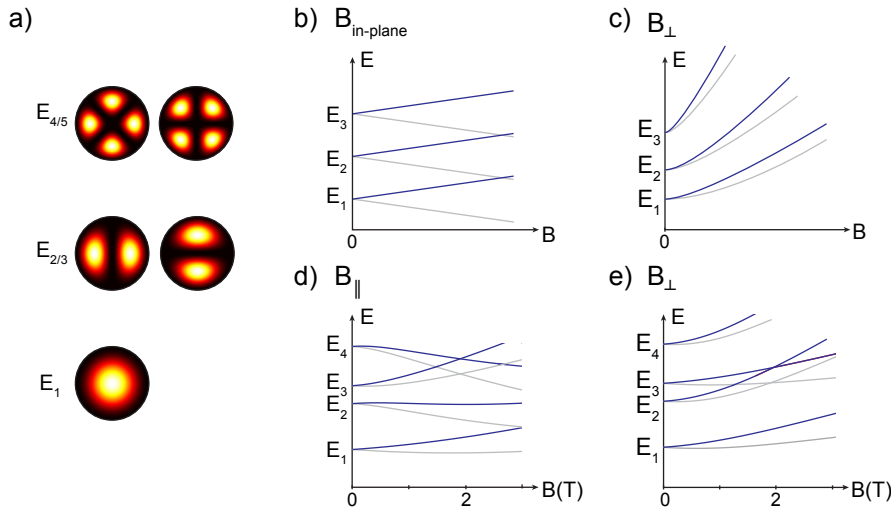
Figure 2.2: **a)** Wavefunction of the five lowest subbands in a nanowire with cylindrical confinement potential. Rotational symmetry causes degeneracies between subbands with identical orbital angular momentum, e.g. $E_{2,3}$ and $E_{4,5}$. **b)** An in-plane magnetic field lifts spin degeneracy leading to a a linear Zeeman splitting between subbands with opposite spin. **c)** A perpendicular magnetic field modifies the subband confinement adding a B-field dependent, non-linear energy splitting to the Zeeman splitting. **d),e)** Numerical simulations of the subband dispersion in hexagonal nanowires for parallel (d) and perpendicular (e) orientation.

Another difference between 2DEGs and nanowires is the length of the electron mean free path μ_e. In 2 dimensional systems it is on the order of µm, much larger than the size of the QPC constriction. This means that ohmic contacts can be placed far from the QPC and will not affect its potential profile. In nanowires however, the mean free path is only around 100 nm–200 nm. Because of this the contacts have to be very close to the QPC and will significantly contribute to the QPC potential. Using the software package Kwant [23] more realistic tight binding simulations can be performed which take the hexagonal cross section of our nanowires into account as well as asymmetries induced by the contacts and gate electrodes.

2.2.5. ZEEMAN SPLITTING AND ORBITAL EFFECTS

Adding an external magnetic field, B, breaks time reversal symmetry and lifts the spin degeneracy of each subband. The individual spin subbands $E_n^\pm$ split by the Zeeman energy which increases linearly with magnetic field (Fig. 2.2b).

$$E_n^\pm(B) = E_n(0T) \pm \frac{1}{2} g \mu_B B. \tag{2.17}$$

Here μ_B is the Bohr magneton and g is the electron g-factor. In conductance measurements this causes the appearance of half plateaus at $(N + 1/2) \cdot G_0$. For QPC defined in 2DEGs this simple model agrees well with experimental observations when B is applied in the x-y plane. Different materials and QPC potentials will influence the exact value and amount of anisotropy of the g-factor, but the subband splitting remains linear up

to high values of magnetic field [24, 25]. In contrast, a magnetic field aligned along z, perpendicular to the 2DEG, will give a very different subband evolution. To see this we explicitly include the vector potential in equation (2.14) by substituting $p \rightarrow (p - eA)$, with $A = (0, Bx, 0)$

$$H = \frac{(p - eA)^2}{2m^*} + V(x, y) + \frac{1}{2} g \mu_B B.$$

(2.18)

For a parabolic confinement potential, this can be solved explicitly [22] and we get

$$E_n(k_x) = (n - 1/2)\hbar\omega + \frac{\hbar^2 k_x^2}{2m} + \frac{1}{2} g \mu_B B.$$

(2.19)

With the cyclotron frequency $\omega_C = eB/m^*$, $\omega = \sqrt{\omega_0^2 + \omega_C^2}$ and $m = m^* \omega^2/\omega_0^2$. Without QPC confinement the perpendicular magnetic field creates quantized Landau levels with energy $E_n^B = (n - 1/2)\hbar\omega_C$, well known from the quantum Hall effect [19]. In QPCs it causes additional confinement which combines with the QPC potential $V(x, y)$. This leads to the emergence of hybridized magnetoelectric subbands with non linear B-field dependent energy spacing, often called orbital effects [24–26]. Simulations for a realistic QPC potential can for example be found in reference 24 (Fig. 2.2c). In nanowires QPCs the effect of a magnetic field will be similar to this. Detailed numerical simulations of the subband dispersion in realistic hexagonal nanowires are shown in Fig. 2.2d,e). Because of the radial confinement strong orbital effects are now expected for magnetic fields oriented both along y and z direction. Even the subband splitting for magnetic fields aligned along the nanowire is no longer linear as shown in Fig. 2.2d) [27].

2.3. HELICAL GAP

In one dimensional systems with strong SOI, magnetic fields can induce an energy gap in the dispersion relation. This energy gap, called helical gap, or spin-orbit induced Zeeman gap, is an essential ingredient for the creation of topological superconductors with induced Majorana bound states. QPC measurements can reveal such a gap because of its very distinctive signature in conductance measurements, which we will explain in the following paragraphs. First, we discuss how the combination of spin-orbit Interaction and magnetic field opens an energy gap and how it modifies the conductance through a QPC. Next we look at the evolution of the gap in a rotating magnetic field and finally we see how the experimental visibility of the helical gap is influence by the shape of the QPC potential. This explains why helical gap signatures have so far been difficult to observe experimentally.

Similar to reference 16 we consider a system with ballistic electron transport along x direction, confinement potential $V(z)$ and a magnetic field in the x-y plane causing Zeeman splitting $\frac{1}{2} g \mu_B B$. Neglecting the influence of Dresselhaus SOI, we only consider the Rashba term $H_{SO} = i\alpha_R(\sigma_x \frac{\partial}{\partial y} - \sigma_y \frac{\partial}{\partial x})$, which simplifies further because electron motion is restricted to the x-direction $H_{SO}^{1D} = -i\alpha_R \sigma_y \frac{\partial}{\partial x}$. Using $p_x = i\hbar\frac{\partial}{\partial x}$ we get the Hamiltonian,

$$\begin{aligned}
H &= H_{QPC} + H_{Zeeman} + H_{SO} \\
&= \frac{p_x^2}{2m^*} + V(y) + \frac{1}{2} g \mu_B \vec{\sigma} \cdot \vec{B} + \frac{\alpha_R}{\hbar} p_x \sigma_y,
\end{aligned}$$

(2.20)

a) $B = 0T$

b) $B \perp B_{SO}$

c) $B \parallel B_{SO}$

d) $E_Z \gg E_{SO}$
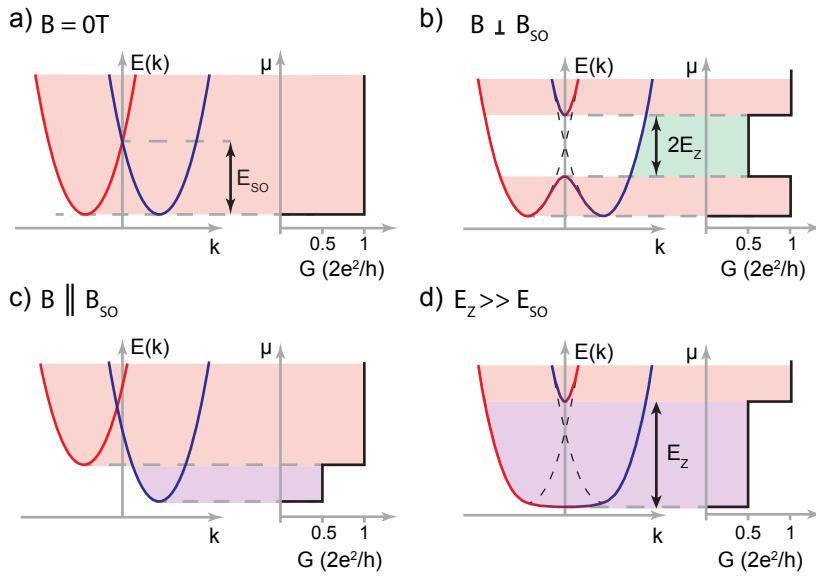
Figure 2.3: Emergence of the helical gap. **a)** Rashba SOI couples electron spin and momentum and splits the spin subbands horizontally. Spin degeneracy remains conserved and conductance measurements are identical to the case without SOI. **b)** A magnetic field $B \perp B_{SO}$ induces an anticrossing and opens an energy gap $E_{gap} = g\mu_B B$ around $k_x = 0$. In conductance measurements the gap appears as a dip from $2e^2/h$ down to e^2/h. **c)** For B parallel B_{SO} the gap closes. **d)** At large magnetic fields $E_Z \gg E_{SO}$ the subband dispersion approaches 2 spin split subbands without SOI.

One important note is that the magnetic field does not enter through the vector potential A as earlier in equation (2.18) and therefore orbital effects will not be described correctly. It is, however, still instructive to solve this simple model. The spin-orbit field $\vec{B}_{SO} = \frac{2\alpha_R}{\hbar}(\vec{k} \times \vec{z})$ is oriented along the y-direction since electron motion is restricted to $\vec{x}$ and the electric field from the confinement potential is oriented along $\vec{z}$. Solutions to this Hamiltonian are of the form $\Psi = e^{ik_x}\Phi(y)\binom{\varphi_\uparrow}{\varphi_\downarrow}$, with the transverse wavefunction $\Phi(y)$ and spinors $\varphi_{\uparrow,\downarrow}$ representing electrons with spin up and spin down. The subband energies are then given by

$$E_n^\pm = \frac{\hbar^2 k^2}{2m^2} \pm E_n\sqrt{\left(\frac{g\mu_B B}{2}\right)^2 + g\mu_B\alpha_R kB\cos(\theta) + \left(\alpha_R k\right)^2}. \qquad (2.21)$$

$\pm$ denotes the energy of spin up and spin down states and θ is the angle of the external magnetic field $\vec{B}$ with respect to the y-axis (and $\vec{B}_{SO}$). This subband spectrum is drawn in Fig. 2.3 for different magnetic fields. At $B = 0$ the Rashba SOI breaks subband spin degeneracy and splits the two bands horizontally (Fig. 2.3a). If a finite magnetic field is applied along x-direction we get an energy dispersion for the first subband (Fig. 2.3b)

$$E^\pm = \frac{\hbar^2 k_x^2}{2m^*} \pm \sqrt{\left(\frac{g\mu_B B}{2}\right)^2 + \left(\alpha_R k_x\right)^2}. \qquad (2.22)$$

Because the external magnetic field is perpendicular to B_{SO} it couples the subbands with opposite spin and induces an anticrossing at $k_x = 0$ with an energy gap $E_{gap} = g\mu_B B$. In contrast, if the magnetic field is parallel to $\vec{B}_{SO}$ it will only create an energy shift but no coupling between the subbands with opposite spin (Fig. 2.3c)

$$E^\pm = \frac{\hbar^2 k_x^2}{2m^*} \pm \left(\alpha_R k_x + \frac{g\mu_B B}{2}\right). \qquad (2.23)$$

2.3.1. SIGNATURE IN CONDUCTANCE MEASUREMENTS

To understand the effect of the spin-orbit gap on QPC conductance measurements we first consider the case of perfect transmission $T_n(E) = 1$. We then get [16]

$$G = \frac{e^2}{h}\sum_{n,s}\sum_i \beta_i^{(n,s)} f(E_i^{(n,s)}). \qquad (2.24)$$

The first sum runs over all subbands n and spins s and the second sum counts all extrema i of the subbands. $\beta_i^{(n,s)}$ is $+1$ for a minimum and -1 for a maximum. The resulting conductance traces are shown next to the subband dispersions in Fig. 2.3. At Zero magnetic field SOI splits the spin subbands in momentum space, but both subbands are still degenerate in energy which gives conductance steps at multiples of $2e^2/h$ identical to the situation without SOI. Similarly if B_{ext} is aligned with B_{SO} each subband will be split by the Zeeman energy giving conductance steps at multiples of e^2/h. The most interesting case is for a magnetic field B_{ext} that is not perfectly aligned with B_{SO}. First we discuss the case of a perpendicular magnetic field and then move on to arbitrary angles θ (Fig. 2.4). At perpendicular magnetic field both spin subbands still have a minimum at identical
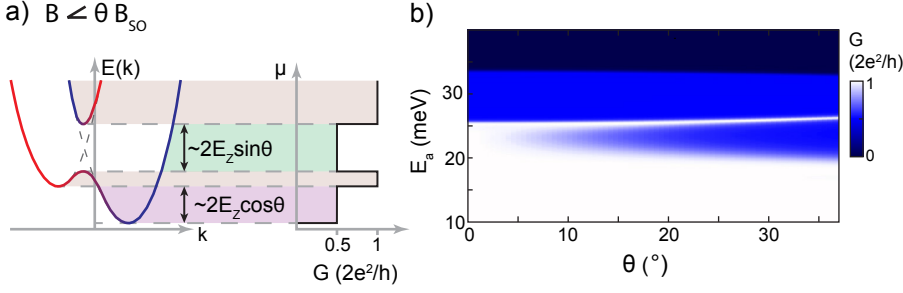
Figure 2.4: Angle dependence of the helical gap. **a)** A magnetic field at arbitrary angles θ creates a combined contribution of Zeeman splitting and anticrossing. The conductance now shows both an initial plateau at $0.5\,G_0$ as well as a dip from $1\,G_0$ down to $0.5\,G_0$. The width of each of feature depends on θ as indicated. **b)** Simulations of the angle dependent conductance.

energies and the conductance will go to $2e^2/h$. However, when the chemical potential μ enters the spin-orbit gap it crosses a local maximum and the conductance will drop to e^2/h before returning to $2e^2/h$. The spin-orbit gap will show up as a dip in the first plateau with a width determined by the strength of the external magnetic field. Inside this gap only the two outer states are occupied giving electrons with opposite momentum nearly opposite spin orientation - hence the name helical gap. The size of the gap is determined by E_Z and for large perpendicular magnetic fields $E_Z \gg E_{SO}$ when the influence of the SOI becomes small, the subband dispersion approaches the normal case with only Zeeman splitting (Fig. 2.3d).

2.3.2. ANGLE DEPENDENCE OF THE SPIN-ORBIT GAP

The difference in the subband structures of Fig. 2.3b,c) demonstrates the strong angle dependence of the helical gap size with respect to the external magnetic field. Checking this angle dependence is an important confirmation that an experimentally observed conductance dip is actually related to the spin-orbit interaction. Generalizing the Hamiltonian (2.20) we get [16]

$$H = \frac{p^2}{2m^*} + \frac{\alpha}{\hbar} p\sigma_y + \frac{1}{2} E_Z \big(\sin(\theta)\sigma_x + \cos(\theta)\sigma_y\big) \tag{2.25}$$

With the Zeeman energy $E_Z = g\mu_B B$ and assuming a magnetic $\vec{B}$-field oriented in the $x - y$ plane at an angle θ relative to $\vec{B}_{SO}$. The resulting bandstructure is shown in Fig. 2.4a) and now has two B-field induced features. The energy gap $E_{Z,1}$ opening at around the band crossing and the Zeeman shift between the two band minima $E_{Z,2}$. Their angle dependence is given by

$$E_{Z,1} \approx E_Z \sin(\theta) \tag{2.26a}$$

$$E_{Z,2} \approx E_Z \cos(\theta). \tag{2.26b}$$

When rotating the magnetic field the subband dispersion in Fig. 2.3b) gradually transitions to the one in Fig. 2.3c). If we increase the angle starting from $\vec{B} \parallel \vec{y}$ the size of the
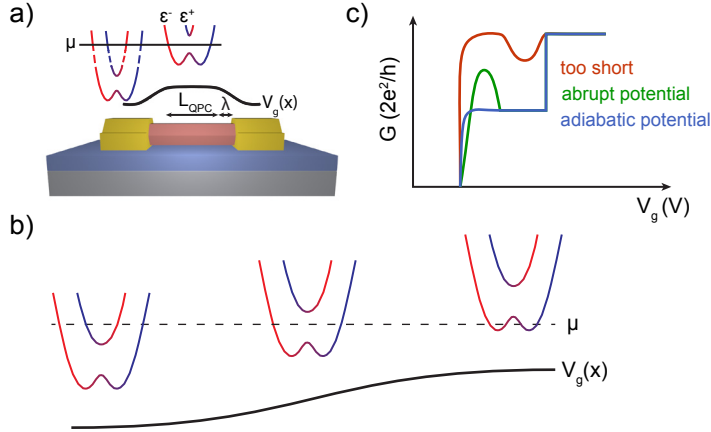
Figure 2.5: **a)** Sketch of a realistic nanowire QPC. A hexagonal nanowire (red) with metallic contacts (yellow) lying on top of a backgate (grey) with gate dielectric (blue). The QPC potential is drawn above the nanowire. It sets on over a length λ reducing the actual QPC length to L_{QPC}. **b)** Spacial variation of the subband energy because of the gate potential. States of high momentum below the metallic contacts need to tunnel through the energy gap to end up in low energy states at the bottom of the first subband inside the QPC. **c)** The onset length λ strongly influences the visibility of the helical gap.

helical gap decreases with $\sin(\theta)$ and both subbands shift vertically by $cos(\theta)$ creating an initial $0.5 \cdot G_0$ plauteau in conductance measurements.

2.3.3. GAP VISIBILITY IN REALISTIC DEVICES

In our discussion of the helical gap and its signature in conductance measurements we have so far assumed perfect transmission to the contacts $T_n(E) = 1$. Any realistic device, especially QPCs in nanowires, will be far from this ideal case. Because of screening from the metallic contacts the QPC potential only sets on gradually and the actual QPC length will always be shorter than the contact spacing. The width of the region over which the chemical potential is tuned inside the helical gap depends on the actual length of the QPC (Fig. 2.5a). In very short QPCs electrons have a high change of tunneling through the gapped region which causes the conductance dip to be suppressed or even invisible. To avoid this, the QPC length should be as long as possible, at least a few times l_{SO}. At the same time the maximum QPC length is limited by the electron mean free path. If the channel is too long, disorder will dominate the conductance plateaus and destroy the necessary quantization. This sets an upper and lower limit on the QPC length necessary for the observation of a helical gap. Detailed simulations performed in Ref [28, 29] show that finite size effects, finite temperature and in particular the shape of the QPC potential will also have dramatic influence on the visibility of the spin-orbit gap in transport measurements. Here we briefly summarize and discuss those results and relate them to our nanowire devices presented in chapter 6. The simulations are performed with tight binding simulations with a model similar to equation (2.20), but with a more realistic

confinement potential

$$V_g(x) = V_g^N + \frac{V_g^0 - V_g^N}{2}\left[\tanh\left(\frac{x - x_0}{\lambda}\right)\right].\tag{2.27}$$

This gives a smooth variation from the potential under the metallic contacts V_g^N to the potential in the wire V_g^0 with a linear slope around x_0 given by $\Delta V_g/\lambda$. A sketch of this is included in Fig. 2.5b). As the simulations show, the exact value of λ dominates the conductance. If λ is small the QPC potential will set on very abruptly and if λ is large it will set on adiabatically. An abrupt onset causes strong mode mismatch increasing the chance for back reflection. The reflection is stronger for the low momentum states which strongly suppresses the initial $2e^2/h$ peak as sketched in Fig. 2.5c). This could be avoided by having an adiabatic potential onset. Fig. 2.5b) sketches shifted subbands at different spatial position along the QPC. In the contacts the Fermi level is high and states with large momentum are occupied while inside the QPC the situation is reversed. Especially at the onset of each subband, the high momentum states under the leads are connected to low momentum states in the center of the constriction. On the way they have to tunnel through a region gapped by the helical gap. Now if the potential onset is too slow this will again strongly suppress the initial peak to $2e^2/h$. To maximize the visibility of the helical gap, the potential profile therefore has to be finely tuned to an optimal length scale. The authors of [28] find an optimum length for the potential onset $\lambda^* = \frac{\hbar v_F}{\Delta_Z} \approx \sqrt{\frac{E_{SO}m^*}{2\hbar^2}}/\Delta_Z$. Notice that λ^* depends on v_F and B so it is changed by the gate potential as well as the magnetic field. Including finite size effects and disorder in the simulations confirms this basic observation but also shows that Fabry-Perot oscillations can lead to an even stronger suppression of the $2e^2/h$ peak and that too much disorder will also destroy the signature of the helical gap.

2.3.4. CONCLUSIONS

We have seen that the predicted signature of a helical gap can, in practice, only be observed over a narrow parameter range which is very challenging to realize experimentally;

- The QPC should be as long as possible, to clearly see the reentrant feature of the helical gap, at the same time transport still has to be ballistic.

- The shape of the QPC potential onset has to be close to the ideal length scale λ^*. While this can be varied for individual devices, for example by changing the thickness of the gate dielectric, λ^* depends on E_{SO} which is only roughly known.

Apart from the helical gap, other effects related to disorder or interference can also cause anomalous conductance features. Examples for this are Fabry-Perot oscillations or, the Kondo and Fano effects. To unambiguously show that a conductance dip is caused by a helical gap, it is necessary to measure the evolution in magnetic field and confirm both the linear increase in magnetic field, as well as the correct evolution in a rotating magnetic field.
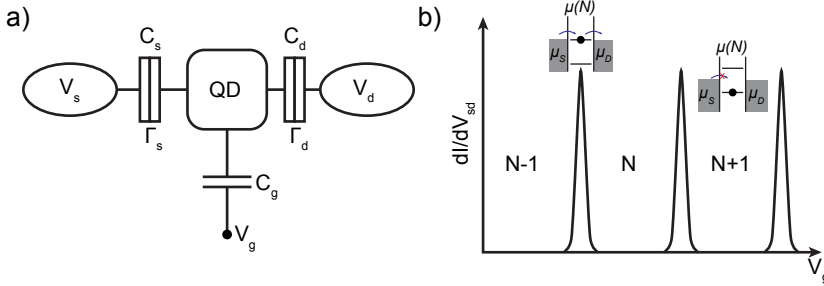
Figure 2.6: **a)** Simple model of a quantum dot. A small island (QD) is connected to source (V_s) and drain (V_d) contacts with capacitance $C_{s,d}$ and tunnel rate $\Gamma_{s,d}$. A capacitively coupled gate voltage controls the charge induced on the island. **b)** Conductance through the quantum dot is normally suppressed and only allowed when one of the energy levels inside the dot $\mu(N)$ is aligned with the chemical potential of the source and drain contacts. This leads to discrete conductance peaks.

2.4. QUANTUM DOTS

Quantum dots are small islands that confine electrons in all 3 dimensions. This creates discrete quantized energy levels similar to single atoms. There are different ways of creating such islands, for example self assembled quantum dots [30], gate defined quantum dots in 2D electron gases [31, 32], carbon nanotubes [33] and nanowires [34, 35]. Having such a large choice of materials and confinement size means that the energy spacings of QDs can be varied from ~eV in the optical range down to ~μeV in low temperature conductance measurements. In the following sections we will briefly explain some of the unique signatures of single and double quantum dots in conductance measurements. Additionally we will see how superconducting microwave resonators provide an alternative readout method of high sensitivity.

2.4.1. SINGLE QUANTUM DOT

To understand the basic properties of a gate defined quantum dot we model it as a small island connected to source and drain contacts through tunnel barriers and capacitively coupled to a gate electrode as shown in Fig. 2.6a). The total energy of a quantum dot with N electrons , $U(N)$ can be calculated with the constant interaction model. [36, 37] This model assumes that the energy level spacing is independent of the number of electrons N and that the coulomb energy felt by an individual electron is described by a single constant capacitance $C = C_s + C_d + C_g$. The number of electrons then changes linearly with V_{gate} and we can define an effective electrochemical potential in the quantum dot

$$\mu(N) = U(N) - U(N-1)$$

The spacing between different energy levels $E_{add} + \Delta E$ is the sum of the charging energy required to overcome coulomb repulsion for adding and extra electron and the level spacing ΔE caused by the confinement. Note that $\Delta E = 0$ is possible, for example when adding electrons to partially occupied degenerate energy levels. With a small bias voltage, electron transport will be allowed if an energy level inside the QD is aligned with $\mu_{s,d}$ and forbidden if it is misaligned. Changes in V_g tune the relative alignment of the
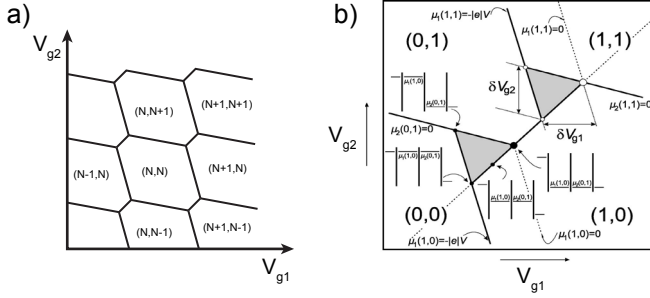
Figure 2.7: **a)** Sketch of a double dot charge stability diagram. Current through the dot is plotted as function of the two plunger gates V_{g1} (V_{g2}) which control the occupancy of the left (right) dot and map out hexagonal regions of constant charge occupancy in the double dot system. At each triple point where three hexagons meet, the levels of both dots are aligned with each other and with the contacts allowing current flow. **b)** At finite bias voltage the triple point expand into triangular regions over which current flow is possible. Picture adapted from Ref. [37].

energy levels and lead to discrete peaks in the conductance as individual QD levels pass through energy window given by the bias voltage (Fig. 2.6b).

2.4.2. DOUBLE QUANTUM DOT

Next we look at two Quantum dots connected in series. The occupation of each dot can be controlled individually by 2 gates and the conductance as function of the two gate voltages V_{g1} and V_{g2} shows a hexagonal pattern (Fig. 2.7a). Inside one hexagon both dots are in coulomb blockade with a constant number of electrons (N_L, N_R). On the edge of a hexagon one or both dots change their occupation by one electron. Electron transport through both dots is only allowed at the points connecting three hexagons, where the chemical potential of both dots is aligned with the potential in the contacts. At finite bias voltage these triple points expand into triangular regions of conductance (Fig. 2.7b).

2.5. MICROWAVE READOUT OF DOUBLE QUANTUM DOTS

A double quantum dot embedded inside a high quality microwave cavity can be modeled with a Jaynes-Cummings Hamiltonian. It models the interactions between a two level emitter and quantized electromagnetic radiation, which is well known from the field of quantum optics and described in many textbooks, [38, 39]

$$H = H_{cavity} + H_{QD} + H_{QC}. \tag{2.28}$$

The first term describes the radiation inside a cavity. It is the sum of all cavity modes n, each with resonance frequency $\omega_n/2\pi$, photon creation an annihilation operators $\hat{a}_n^\dagger$, $\hat{a}_n$ and photon number operator $\hat{n}_n$

$$H_{cavity} = \sum_n \hbar\omega_n(\hat{a}_n^\dagger \hat{a}_n + \frac{1}{2}) = \sum_n \hbar\omega_n(\hat{n}_n + \frac{1}{2}). \tag{2.29}$$

2

For the quantum dot we assume one electron is shared between the two dots so it can be modeled as a two level charge qubit with level spacing $\Omega = \sqrt{\epsilon^2 + 4t^2}$ using the detuning ϵ, interdot tunnel coupling t_C and Pauli matrices $\sigma_{x,y,z}$

$$H_{QD} = \frac{\hbar\Omega}{2}\sigma_z + t_C\sigma_x. \tag{2.30}$$

The two level quantum dot interacts with the fundamental cavity mode ω_c at coupling strength g_C. Assuming the quantum dot is tuned near to the fundamental cavity frequency $\Omega \approx \omega_0$ and $g_C \gg \omega_0, \Omega$ we can perform the rotating wave approximation (RWA) and get the Jaynes-Cummings Hamiltonian

$$H = \frac{\hbar\Omega}{2}\sigma_z + \hbar\omega_0\hat{a}^\dagger\hat{a} + \hbar g_C\frac{T}{\Omega}(a^\dagger\sigma_- + a\sigma_+). \tag{2.31}$$

The RWA neglects the quickly oscillating terms, $\Omega + \omega_c$, and only keeps the low frequency terms, $\Omega - \omega_c$, which means it considers only energy conserving terms and ignores all higher order terms, for example two photon processes. This is similar to the two level approximation which also ignores any higher order processes into additional excited states of the quantum dot. Energy conservation also means that equation 2.31 cannot describe absorption in or emission from the closed cavity-dot system. To capture this, we use a Master equation approach following ref [40]. Moving into the rotating frame of the external probe field $g_C(ae^{-i\omega_R t} + a^\dagger e^{i\omega_R t})$ with the detunings $\Delta_\Omega = \Omega/\hbar - \omega_R$ and $\Delta_C = \omega_c - \omega_R$ we get the effective Hamiltonian ($g_{eff} = g_C\frac{2t_C}{\Omega}$)

$$H = \hbar\Delta_C a^\dagger a + \frac{\hbar\Delta_\Omega}{2}\sigma_z + \hbar g_{eff}(a\sigma_+ + a\sigma_-) \tag{2.32}$$

With this we can derive the time evolution of the operators. Assuming the quantum dot stays near its ground state ($\sigma_z \sim -1$) we get

$$\dot{a} = -i\Delta_C a - \frac{\kappa}{2}a + \sqrt{\kappa_1}a_{in,1} + \sqrt{\kappa_2}a_{in,2} - ig_{eff}\sigma_- \tag{2.33}$$

$$\dot{\sigma}_- = -i\Delta_\Omega\sigma_- - \frac{\gamma}{2}\sigma_- + \sqrt{\gamma}\mathcal{F} - ig_{eff}a \tag{2.34}$$

with the cavity decay $\kappa = \kappa_i + \kappa_1 + \kappa_2$, a combination of internal photon decay κ_i as well as the decay through the in(out)put port $\kappa_{1(2)}$ and the quantum noise terms $a_{in,2}$ and $\mathcal{F}$. Neglecting the latter two noise terms and assuming a simple, classical input field $a_{in,1} \rightarrow \alpha$ simplifies the cavity output to $a_{out,2} = \sqrt{\kappa_2}a - a_{in,2}$. The output at port 2 is proportional to the cavity photon state scaled by the output rate (κ_2) minus the losses through the first port. Transmission through the cavity is now simply the ratio $a_{out,2}/\alpha$ and we can reconstruct the cavity transmission T

$$T = \left|\frac{a_{out,2}}{\alpha}\right|^2 \tag{2.35}$$

and the phase

$$\Delta\Phi = -arg\left(\frac{a_{out,2}}{\alpha}\right) \tag{2.36}$$

In the steady state, $\frac{a_{out,2}}{\alpha}$ can be expressed as

$$\frac{a_{out,2}}{\alpha} = -\frac{i\sqrt{\kappa_1 \kappa_2}}{\Delta_C - i\kappa/2 + g_{eff}\chi},$$

(2.37)

2

with the double dot susceptibility $\chi = \frac{g_{eff}}{-\Delta_\Omega + i\gamma/2}$. To include the effect of charge noise acting on the quantum dot, we additionally convolute this with a Gaussian distribution of linewidth σ.

REFERENCES

[1] L. H. Thomas, "I. the kinematics of an electron with an axis," *The London, Edinburgh, and Dublin Philosophical Magazine and Journal of Science*, vol. 3, no. 13, pp. 1–22, 1927.

[2] R. Winkler, S. Papadakis, E. De Poortere, and M. Shayegan, *Spin-Orbit Coupling in Two-Dimensional Electron and Hole Systems*, vol. 41. Springer, 2003.

[3] C. Kittel and C.-y. Fong, *Quantum theory of solids*, vol. 33. Wiley New York, 1963.

[4] G. Dresselhaus, "Spin-orbit coupling effects in zinc blende structures," *Phys. Rev.*, vol. 100, pp. 580–586, Oct 1955.

[5] E. I. Rashba, "Properties of semiconductors with an extremum loop. 1. cyclotron and combinational resonance in a magnetic field perpendicular to the plane of the loop," *Sov. Phys. Solid State*, vol. 2, no. 6, pp. 1109–1122, 1960.

[6] S. R. Plissard, D. R. Slapak, M. A. Verheijen, M. Hocevar, G. W. G. Immink, I. van Weperen, S. Nadj-Perge, S. M. Frolov, L. P. Kouwenhoven, and E. P. A. M. Bakkers, "From insb nanowires to nanocubes: Looking for the sweet spot," *Nano Lett.*, vol. 12, no. 4, pp. 1794–1798, 2012.

[7] D. A. Wharam, T. J. Thornton, R. Newbury, M. Pepper, H. Ahmed, J. E. F. Frost, D. G. Hasko, D. C. Peacock, D. A. Ritchie, and G. A. C. Jones, "One-dimensional transport and the quantisation of the ballistic resistance," *J. Phys. C*, vol. 21, no. 8, p. L209, 1988.

[8] B. J. van Wees, H. van Houten, C. W. J. Beenakker, J. G. Williamson, L. P. Kouwenhoven, D. van der Marel, and C. T. Foxon, "Quantized conductance of point contacts in a two-dimensional electron gas," *Phys. Rev. Lett.*, vol. 60, pp. 848–850, Feb 1988.

[9] H. T. Chou, S. Lüscher, D. Goldhaber-Gordon, M. J. Manfra, A. M. Sergent, K. W. West, and R. J. Molnar, "High-quality quantum point contacts in gan/algan heterostructures," *Appl. Phys. Lett.*, vol. 86, no. 7, 2005.

[10] D. Többen, D. A. Wharam, G. Abstreiter, J. P. Kotthaus, and F. Schaffler, "Ballistic electron transport through a quantum point contact defined in a si/si 0.7 ge 0.3 heterostructure," *Semicond. Sci. Technol.*, vol. 10, no. 5, p. 711, 1995.

[11] S. J. Koester, B. Brar, C. R. Bolognesi, E. J. Caine, A. Patlach, E. L. Hu, H. Kroemer, and M. J. Rooks, "Length dependence of quantized conductance in ballistic constrictions fabricated on inas/alsb quantum wells," *Phys. Rev. B*, vol. 53, pp. 13063–13073, May 1996.

[12] C. Beenakker and H. van Houten, "Quantum transport in semiconductor nanostructures," *Solid state physics*, vol. 44, pp. 1–228, 1991.

[13] M. J. Iqbal, R. Levy, E. J. Koop, J. B. Dekker, J. P. De Jong, J. H. M. van der Velde, D. Reuter, A. D. Wieck, R. Aguado, Y. Meir, and C. H. van der Wal, "Odd and even kondo effects from emergent localization in quantum point contacts," *Nature*, vol. 501, no. 7465, pp. 79–83, 2013.

[14] F. Bauer, J. Heyder, E. Schubert, D. Borowsky, D. Taubert, B. Bruognolo, D. Schuh, W. Wegscheider, J. von Delft, and S. Ludwig, "Microscopic origin of the/0.7-anomaly/'in quantum point contacts," *Nature*, vol. 501, no. 7465, pp. 73–78, 2013.

[15] R. M. Lutchyn, T. D. Stanescu, and S. Das Sarma, "Search for majorana fermions in multiband semiconducting nanowires," *Phys. Rev. Lett.*, vol. 106, p. 127001, Mar 2011.

[16] Y. V. Pershin, J. A. Nesteroff, and V. Privman, "Effect of spin-orbit interaction and in-plane magnetic field on the conductance of a quasi-one-dimensional system," *Phys. Rev. B*, vol. 69, p. 121306, Mar 2004.

[17] M. Büttiker, "Absence of backscattering in the quantum hall effect in multiprobe conductors," *Phys. Rev. B*, vol. 38, pp. 9375–9389, Nov 1988.

[18] L. P. Kouwenhoven, "Quantum adiabatic electron transport in ballistic conductors," in *Physics of Low-Dimensional Semiconductor Structures*, pp. 463–498, Springer, 1993.

[19] T. Ihn, *Semiconductor Nanostructures: Quantum states and electronic transport*. Oxford University Press, 2010.

[20] P. F. Bagwell and T. P. Orlando, "Landauer's conductance formula and its generalization to finite voltages," *Phys. Rev. B*, vol. 40, pp. 1456–1464, Jul 1989.

[21] L. P. Kouwenhoven, B. J. van Wees, C. J. P. M. Harmans, J. G. Williamson, H. van Houten, C. W. J. Beenakker, C. T. Foxon, and J. J. Harris, "Nonlinear conductance of quantum point contacts," *Phys. Rev. B*, vol. 39, pp. 8040–8043, Apr 1989.

[22] H. van Houten, C. Beenakker, and B. Van Wees, "Quantum point contacts," *Semiconductors and Semimetals*, vol. 35, pp. 9–112, 1992.

[23] C. W. Groth, M. Wimmer, A. R. Akhmerov, and X. Waintal, "Kwant: a software package for quantum transport," *New J. Phys.*, vol. 16, no. 6, p. 063065, 2014.

[24] K. Kolasiński, A. Mreńca-Kolasińska, and B. Szafran, "Transconductance and effective landé factors for quantum point contacts: Spin-orbit coupling and interaction effects," *Phys. Rev. B*, vol. 93, p. 035304, Jan 2016.

[25] F. Nichele, S. Chesi, S. Hennel, A. Wittmann, C. Gerl, W. Wegscheider, D. Loss, T. Ihn, and K. Ensslin, "Characterization of spin-orbit interactions of gaas heavy holes using a quantum point contact," *Phys. Rev. Lett.*, vol. 113, p. 046801, Jul 2014.

[26] T. P. Martin, A. Szorkovszky, A. P. Micolich, A. R. Hamilton, C. A. Marlow, R. P. Taylor, H. Linke, and H. Q. Xu, "Field-orientation dependence of the zeeman spin splitting in (in,ga)as quantum point contacts," *Phys. Rev. B*, vol. 81, p. 041303, Jan 2010.

[27] B. Nijholt and A. R. Akhmerov, "Orbital effect of magnetic field on the majorana phase diagram," *arXiv:1509.02675*, 2015.

[28] D. Rainis and D. Loss, "Conductance behavior in nanowires with spin-orbit interaction: A numerical study," *Phys. Rev. B*, vol. 90, p. 235415, Dec 2014.

[29] J. Cayao, E. Prada, P. San-Jose, and R. Aguado, "Sns junctions in nanowires with spin-orbit coupling: Role of confinement and helicity on the subgap spectrum," *Physical Review B*, vol. 91, no. 2, p. 024514, 2015.

[30] R. J. Warburton, "Single spins in self-assembled quantum dots," *Nature materials*, vol. 12, no. 6, pp. 483–493, 2013.

[31] L. P. Kouwenhoven, C. M. Marcus, P. L. McEuen, S. Tarucha, R. M. Westervelt, and N. S. Wingreen, "Electron transport in quantum dots," in *Mesoscopic electron transport*, pp. 105–214, Springer, 1997.

[32] R. Hanson, L. P. Kouwenhoven, J. R. Petta, S. Tarucha, and L. M. K. Vandersypen, "Spins in few-electron quantum dots," *Rev. Mod. Phys.*, vol. 79, pp. 1217–1265, Oct 2007.

[33] E. A. Laird, F. Kuemmeth, G. A. Steele, K. Grove-Rasmussen, J. Nygård, K. Flensberg, and L. P. Kouwenhoven, "Quantum transport in carbon nanotubes," *Rev. Mod. Phys.*, vol. 87, pp. 703–764, Jul 2015.

[34] S. Nadj-Perge, S. M. Frolov, E. P. A. M. Bakkers, and L. P. Kouwenhoven, "Spin-orbit qubit in a semiconductor nanowire," *Nature*, vol. 468, no. 7327, pp. 1084–1087, 2010.

[35] J. W. G. Van den Berg, S. Nadj-Perge, V. S. Pribiag, S. R. Plissard, E. P. A. M. Bakkers, S. M. Frolov, and L. P. Kouwenhoven, "Fast spin-orbit qubit in an indium antimonide nanowire," *Phys. Rev. Lett.*, vol. 110, no. 6, p. 066806, 2013.

[36] M. Devoret and H. Grabert, "Introduction to single charge tunneling," in *Single Charge Tunneling*, pp. 1–19, Springer, 1992.

[37] W. G. van der Wiel, S. De Franceschi, J. M. Elzerman, T. Fujisawa, S. Tarucha, and L. P. Kouwenhoven, "Electron transport through double quantum dots," *Rev. Mod. Phys.*, vol. 75, pp. 1–22, Dec 2002.

[38] E. T. Jaynes and F. W. Cummings, "Comparison of quantum and semiclassical radiation theories with application to the beam maser," *Proceedings of the IEEE*, vol. 51, no. 1, pp. 89–109, 1963.

[39] A. Imamoglu and Y. Yamamoto, "Mesoscopic quantum optics," 1999.

[40] K. D. Petersson, L. W. McFaul, M. D. Schroer, M. Jung, J. M. Taylor, A. A. Houck, and J. R. Petta, "Circuit quantum electrodynamics with a spin qubit," *Nature*, vol. 490, no. 7420, pp. 380–383, 2012.

2

3

FABRICATION AND MEASUREMENT TECHNIQUES

This chapter gives a brief overview of the most important fabrication steps as well as the DC and microwave measurements setup used in this thesis.
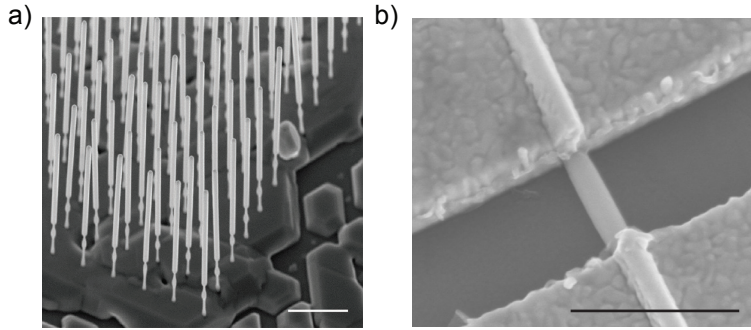
Figure 3.1: **a)** Scanning electron microscope (SEM) image of a nanowire growth chip. InSb nanowires grow vertically on top of InP/InAs stems. **b)** SEM image of a finished nanowire device. A single nanowire was transferred on a $n++$ Si-substrate and contacted with Cr/Au. Scale bar in a) and b) corresponds to 500 nm
.

3.1. DEVICE FABRICATION

This chapter first introduces the practical steps which are necessary to create a working device and prepare it for measurements. This is followed by a short overview of the measurement setups used in this thesis. There are extensive descriptions about the basics of nanofabrication in earlier theses [1, 2] and in literature [3]. The explanations are therefore kept short and only cover the steps, which are most crucial for the fabrication of high quality QPC devices.

3.1.1. NANOWIRE GROWTH AND DEPOSITION

The InSb nanowires used in this thesis were grown with metal organic vapor phase epitaxy (MOVPE) using vapor-liquid-solid (VLS) growth [4]. Au droplets are deposited on an InP substrate and act as catalysts for the growth. During growth the substrate is heated until the Au melts and then exposed to metalorganic precursors. These precursors will decompose close to the Au-catalyst, releasing their metallic atoms which dissolve into the droplets. When the concentration of metals inside the liquid catalysts reaches saturation, single crystal layers deposit one by one at the bottom. Direct growth of InSb nanowires is challenging because of the large lattice mismatch between InP (substrate) and InSb (nanowire). To circumvent this problem, short stems of InP and InAs are grow first, before switching to InSb. This results in high quality InSb nanowires free of stacking faults with zinc-blende crystal structure and oriented along the [111] crystal direction. Typical diameters of these nanowires are 60–120 nm with a length of 1–3 µm and more details about the growth can be found in ref 5. The finished growth chip contains a dense forest of vertically aligned nanowires from which individual wires have to be separated and contacted to measure their electrical properties. Early experiments [6] used cleanroom tissues to transfer nanowires. While this method worked fine in principle, it wasted a large proportion of the nanowires on the growth chip and deposited the wires at random points. A huge improvement was achieved by using a nanomanipulator [7]. Here, a fine needle under an optical microscope is used to pick up individual wires

from the growth chip and place them deterministically on the Si-substrate. Although this method can take quite some time to learn, it guarantees high yield of nanowire transfer and precise alignment both in angle and position with accuracies of less than 5° and 1 µm. Nanowires are typically deposited on top of a degenerately doped $n++$ Si-substrate, which can act as backgate or on top of pre-defined bottom gates.

3.1.2. CONTACT FABRICATION

After deposition, electrical contacts to the nanowire are defined with ebeam lithography. Typically Au is used for metallic contacts and Al or NbTiN for superconducting contacts. Between growth and contact fabrication the nanowires are exposed to air and a thin layer of insulating surface oxide forms. To achieve transparent contacts this layer has to be removed before metal deposition and in our group there are two different methods in use. Either a diluted ammonium polysulfide $(NH_4)_2S_x$ solution which chemically etches and passivates the nanowire surface [8], or alternatively the surface is etched physically with a plasma or a directional beam of atoms. While both methods succeed in creating ohmic contacts, they differ in important details. A well calibrated chemical etch is gentle and self-terminating and removes only a few nm of the nanowire surface. Additionally it leaves a thin passivating sulfur layer on the surface. This layer prevents an immediate reoxidation when the wires are transferred to the metal evaporator and it induces surface doping which can help with maximizing contact transparency [9]. However, the homogeneity of this sulfur layer is unknown and it is necessary to rinse the chip and reexpose it to air during the transfer into an evaporator. These factors can limit the cleanliness of the contact interface. In contrast to this, physical etching can be performed in situ directly before contact deposition which guarantees a pristine nanowire surface. The main disadvantages of this approach are the strong directionality of the etch and the possibility that ions or atoms not only etch the surface but can also penetrate deeper into the nanowire and induce additional defects. A major improvement of the contact quality was achieved by using a combination of both processes. First the surface oxide is removed with sulfur passivation and then a very short and gentle in-situ ion etch is added immediately before contact deposition. A more detailed investigation about the influence of individual process parameters is given in chapter 4 and reference 10.

3.1.3. POSTPROCESSING

After fabrication, the chip is glued on a printed circuit board (PCB) and electrically connected with thin Al-wires. Because of the small dimensions and high resistance of nanowire devices they are very sensitive to electrostatic discharge and great care has to be taken to avoid the destruction of devices. The PCB is then connected to a copper piece which is in direct contact with the mixing chamber of a dilution refrigerator (DR). All measurements presented in this thesis were performed in DR's with base temperatures ranging from 20 to 100 mK.

3.2. DC MEASUREMENT SETUP

To minimize electron temperature and noise all wires are thermally anchored at multiple points inside the DR and pass through several stages of filtering. Most of the electronics
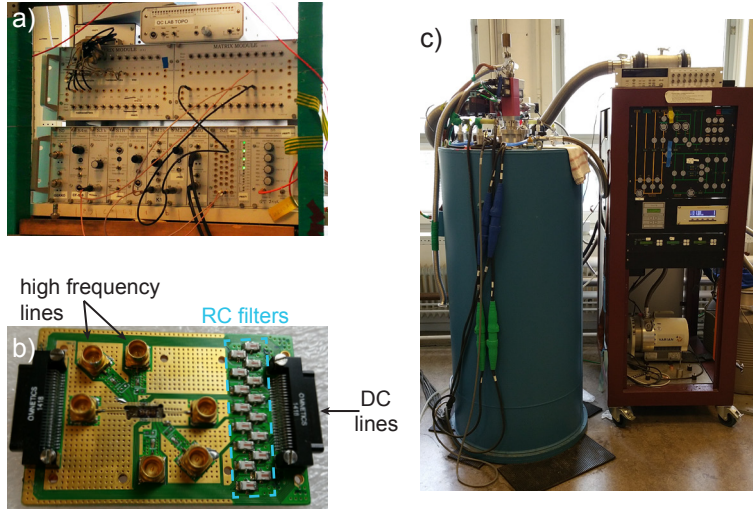
3

Figure 3.2: Dilution refrigerator and measurement setup. **a)** Battery powered IVVI rack with voltage and current sources and measurement modules. **b)** PCB board with with microwave and dc connectors designed for the measurements in chapter 7. **c)** One of the dilution refrigerators used for the measurements in this thesis.

and filtering are developed in house by Raymond Schouten. To galvanically isolate the measurement electronics they are battery operated and communicate with the measurement computer through an optical link only. At room temperature, π filters are used to filter the intermediate frequency range (10 MHz-10 GHz) and additional copper powder and RC filters are added on the cold finger for the remaining higher and lower frequency range. This not only reduces the noise but also helps with absorbing high energy electrons. Conductance measurements were performed with standard lock-in techniques at (quasi) DC , typically operated at $50-100\,\mathrm{Hz}$ with a voltage excitation $dV \sim 5-100\,\mu\mathrm{V}$.

3.3. SUPERCONDUCTING MICROWAVE RESONATORS

The microwave resonators used in this thesis are coplanar waveguides defined in thin superconducting NbTiN films. Fig. 3.3 sketches the basic layout of such a resonator. It consists of a thin stripline of width W, separated by a small gap from two ground planes. Two cuts, interrupting the stripline, define a cavity which is capacitatively coupled to the input and output lines. The small mode volume of such a cavity generates very high field gradients, which are maximized at each end close to the coupling capacitors. The resonance frequency ν_0 is set by the cavity length l, capacitance C and inductance L.

$$\nu_0 = \frac{1}{2l\sqrt{LC}}. \tag{3.1}$$

Typical values for ν_0 are $4-8\,\mathrm{GHz}$ which can be changed by varying the resonator length. The capacitance is extracted from simulations, but the inductance L is considerably modified by the kinetic inductance L_k of our thin NbTiN films $L = L_g + L_k$. Small varia-
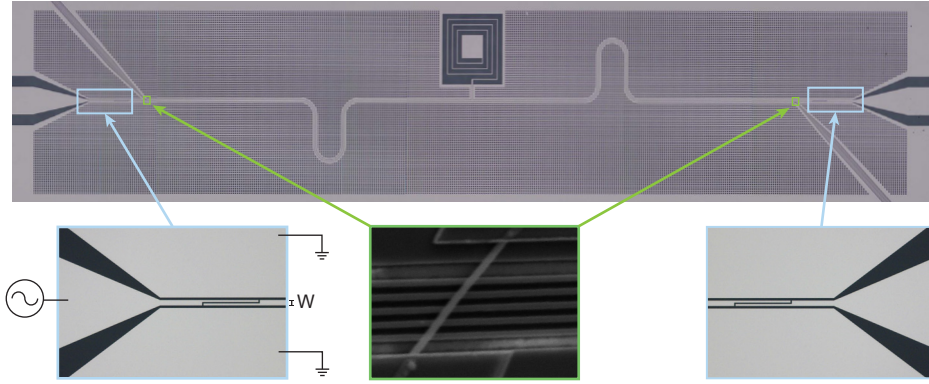
Figure 3.3: Optical image of the coplanar microwave image used in this thesis. A central stripline out of NbTiN (light gray) is separated from two groundplanes by a small gap (dark gray). Insets (light blue) show capacitors at each end which act as semitransparent mirrors and define a $\lambda/2$ cavity. The central inset (green) shows an InSb nanowire, placed close to the resonator ends as described in more detail in chapter 7. Holes in the groundplane are added to increase the magnetic field compatibility of the resonator.

tions of the films thickness are enough to change the resonance frequency.

Resonators are a way to engineer the vacuum energy spectrum and only allow emission into a narrow bandwidth $\delta \nu$ which is correlated to the decay rate κ and the quality factor Q of a cavity. The measured quality factor of a resonator, called loaded quality factor Q_L will be a combination of internal losses in the cavity Q_{int} and losses through the input and output ports Q_{ext}.

$$\frac{1}{Q_L} = \frac{1}{Q_{int}} + \frac{1}{Q_{ext}} \tag{3.2}$$

$$Q_L = \frac{\nu_0}{\delta \nu} \tag{3.3}$$

$$\kappa = 2\pi \frac{\nu_0}{Q_L}. \tag{3.4}$$

Several mechanism are responsible for the internal losses of a resonator, for example defects in the surrounding dielectric, radiative losses, or vortices and quasiparticles in the superconducting film. External losses can be engineered and optimized for individual measurements. Resonators with small coupling capacitances, called undercoupled, maximize the photon lifetime, but decrease the signal emitted from the resonator. Overcoupled resonators artificially decrease the photon lifetime inside the resonator and increase the signal allowing faster measurements.

3.4. MICROWAVE MEASUREMENT SETUP

After fabrication the resonator is glued on a printed circuit board (PCB) equipped dc lines and with coaxial connectors for the microwave signals. The PCB is enclosed inside a tight copper box to shield it from electromagnetic radiation and mounted on the cold finger of a DR. At a base temperature of 20mK the remaining thermal energy is much
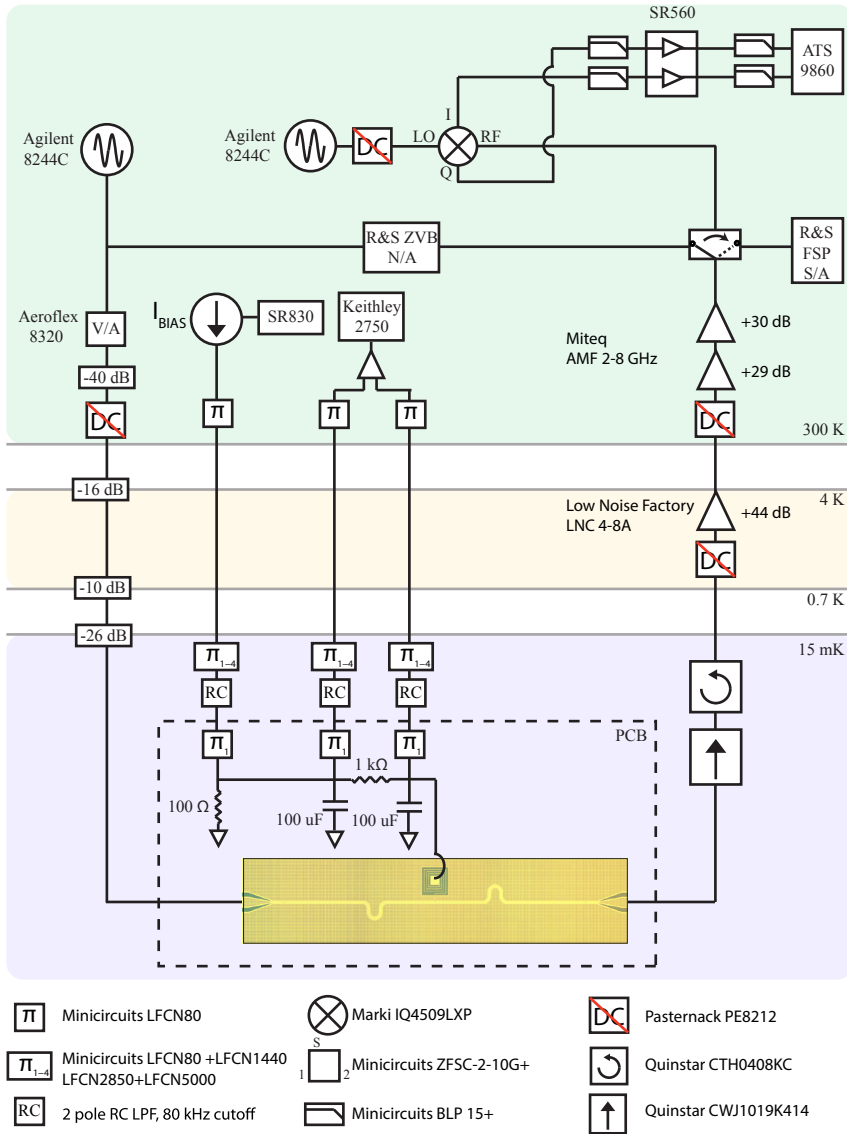
3

Figure 3.4: Circuit schematic of the measurement setup used in chapter 8.

smaller than the single photon energy inside the resonator ($5\,\text{Ghz} \sim 240\,mK$). The DC lines are identical to the setup described above and a sketch of the microwave setup is shown in Fig. 3.4. On the input line attenuators are added at different temperature plates of the fridge (at 4K, 0.7K, 15mK). These are essential to suppress thermal radiation through the coax cables. Additionally they help with thermalizing the cables at each stage. At the output port the signal passes first through an isolator to prevent radiation leaking back into the cavity. Then it is amplified with a cryogenic HEMT amplifier. At room temperature the signal is multiplied with a local oscillator in an IQ mixer to convert it to lower frequencies. The I and Q components (note that here, Q does not refer to the quality factor), then pass a low pass filter and are amplified again before being digitized with a fast Alazar 9850 acquisition card. From the $I\text{-}Q$ components the amplitude and phase can be reconstructed via

$$
\begin{aligned}
A(t) &= \sqrt{I(t)^2 + Q(t)^2} \\
\phi(t) &= \arctan\left(\frac{Q(t)}{A(t)}\right).
\end{aligned}
\tag{3.5}
$$

REFERENCES

[1] I. van Weperen. PhD thesis, TU Delft, 10 2014.

[2] K. Zuo and V. Mourik, *Signatures of Majorana Fermions in Hybrid Superconductor-Semiconductor Nanowire Devices*. PhD thesis, TU Delft, Delft University of Technology, 2016.

[3] M. Stepanova and S. Dew, *Nanofabrication: techniques and principles*. Springer Science & Business Media, 2011.

[4] S. R. Plissard, D. R. Slapak, M. A. Verheijen, M. Hocevar, G. W. G. Immink, I. van Weperen, S. Nadj-Perge, S. M. Frolov, L. P. Kouwenhoven, and E. P. A. M. Bakkers, "From insb nanowires to nanocubes: Looking for the sweet spot," *Nano Lett.*, vol. 12, no. 4, pp. 1794–1798, 2012.

[5] D. Car, *Synthesis of InSb nanowire architectures: building blocks for Majorana devices*. PhD thesis, 2016.

[6] J. W. W. Van Tilburg, *Electron spins in nanowire quantum dots*. PhD thesis, TU Delft, Delft University of Technology, 2010.

[7] K. Flöhr, M. Liebmann, K. Sladek, H. Y. Günel, R. Frielinghaus, F. Haas, C. Meyer, H. Hardtdegen, T. Schäpers, D. Grützmacher, and M. Morgenstern, "Manipulating inas nanowires with submicrometer precision," *Rev. Sci. Instrum.*, vol. 82, no. 11, p. 113705, 2011.

[8] D. B. Suyatin, C. Thelander, M. T. Björk, I. Maximov, and L. Samuelson, "Sulfur passivation for ohmic contact formation to inas nanowires," *Nanotechnology*, vol. 18, no. 10, p. 105307, 2007.

[9] H. Zhang, Ö. Gül, S. Conesa-Boj, K. Zuo, V. Mourik, F. K. de Vries, J. van Veen, D. J. van Woerkom, M. P. Nowak, M. Wimmer, *et al.*, "Ballistic majorana nanowire devices," *arXiv preprint arXiv:1603.04069*, 2016.

[10] Ö. Gül, H. Zhang, F. K. de Vries, J. van Veen, K. Zuo, V. Mourik, S. Conesa-Boj, M. Nowak, D. van Woerkom, M. Quintero-Perez, M. Cassidy, A. Geresdi, S. Koelling, D. Car, S. Plissard, E. P. Bakkers, and L. P. Kouwenhoven, "Hard superconducting gap in insb nanowires," *Nano Letters*, vol. 17, no. 4, pp. 2690–2696, 20107.

3

4

OPTIMIZATION OF NANOWIRE QPC DEVICES

To achieve the results presented in chapters 5 and 6, significant improvements in device fabrication were necessary. Conductance measurements of nanowire devices respond sensitively to changes in the contact interface and in the nanowire environment. Careful optimization and control of different processes and device parameters is therefore very important. In this chapter, I present a more detailed investigation of changes in different process parameters to emphasize their importance and to hopefully provide a point of reference for future device generations.

4.1. INTRODUCTION

InSb nanowires have attracted great interest because they combine large electron mobilities [1], high g-factors [2–5] and strong spin-orbit coupling [6–8]. Initial experiments focused on qubits [5, 9, 10] which was soon followed by attempts to realize topological superconductors in hybrid superconductor-nanowire systems [11–14]. However, the large surface to volume ratio and the increased chance of backscattering in one dimensional systems, limit device performance. Until recently, ballistic transport could only be observed at high magnetic fields where scattering is strongly suppressed. Reliable confirmation of ballistic electron transport as discussed in chapter 5, was only possible by combining low noise dielectrics with an improved contact recipe. This demonstrated that the nanowire environment as well as the nanowire-metal interface crucially impact device performance. To make good electrical contact with a nanowire, the intrinsic surface oxide has to be removed first. In our group there are two methods for doing this, Ion milling or sulfur passivation. Physical etching, for example with Ar-ions, can be done in situ directly before contact deposition which guarantees a pristine nanowire surface with a minimal amount of residues. It requires careful calibration to avoid excessive damage of the exposed nanowire surface [15] and high energy ions are a potential source of crystal defects in the nanowire. In comparison, sulfur passivation is a chemical etch which is isotropic and self terminating and removes only around 5 nm of the nanowire surface. After the etching a thin passivation layer of sulfur is left on the surface which is important to prevent immediate re-oxidation when the nanowire is transferred into the metal evaporator. These residues will additionally affect the electrical contact quality through local surface doping and as a possible source of inhomogeneities and contaminations.

Both etching methods generated ohmic contacts of decent but varying quality. Surprisingly, however, using them in combination showed significant improvements over each method individually. This new contact recipe starts with sulfur passivation followed by a very short and gentle ion etch (Ar or He), immediately before contact deposition. While the first etch removes any surface oxide, the second etch helps to remove inhomogeneities and residues left from previous fabrication step and, importantly, is short enough to avoid excess damage of the nanowire. In this chapter, we use simple nanowire quantum point contact (QPC) devices to study the influence of various steps in the fabrication and post processing on the low temperature device performance.

4.2. DEVICE LAYOUT

InSb nanowires with diameters of 70 to 120 nm, grown by MOVPE, are deposited on top of a n++ Si substrate covered by a ~ 20 nm thick Si_3N_4 dielectric. Electrical contacts made of Cr/Au (10/100 nm) are defined by electron beam lithography with a contact spacing of 150 to 450 nm. Immediately before contact deposition the nanowire surface is prepared using the following recipe:

1. Resist development for 60 s in MIBK:IPA, rinsing for 30 s in IPA.

2. O_2-plasma descum for 90 s at 200 sccm flow with 100 W power.

3. Sulfur passivation for 30 min at 60 °C in a saturated ammonium polysulfide solution.
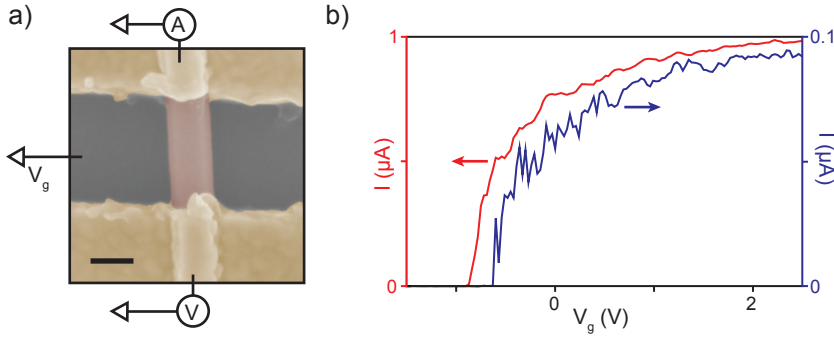
Figure 4.1: Device layout and characterization. **a)** False color SEM image of a nanowire QPC. The nanowire (red) is deposited on n^{++}-silicon covered by 20 nm Si_3N_4 dielectric. Bias voltage V_{sd} is applied via two Cr/Au electrodes (yellow). **b)** Current, I, as function of back gate voltage, V_g, at a bias voltage of 1 mV (blue) and 10 mV (red). Measurements are performed at $T \sim 100$ mK.

4. Chip transfer to evaporator in a non-transparent beaker filled with DI-water followed by 40 min evacuation in the evaporator load lock

5. He-etch for 30 s

6. Contact deposition

A false color Scanning electron microscope picture of a typical device is shown in Fig. 4.1a). The finished devices are mounted inside a dilution refrigerator, evacuated for 12 to 72 h and cooled down to a base temperature of ~ 100 mK. Measurements of the differential conductance dI/dV are performed with standard lock-in techniques at 73 Hz with an excitation $V_{RMS} = 70\mu V$ applied on top of a fixed bias voltage V_{sd} across the two contacts. Conductance through the nanowire is controlled by the gate voltage V_g applied to the Si-substrate, resulting in pinch-off traces as shown in Figure 4.1b). High quality is indicated by a steep rise of the conductance, a large saturation current at high V_g, and a small amount of conductance fluctuations along the trace. Often pinch-off traces are measured at 10 mV bias voltage [1, 3, 16] which causes significant averaging of the conductance [17]. Measurements at lower bias voltage $V_{sd} = 1$ mV are more sensitive. Figure 4.1b) illustrates this and shows a direct comparison of two conductance traces measured at 1 mV and 1 mV on the same device.

4.3. CONTACT INTERFACE

Because of the increased chance of electron backscattering in 1D systems [3] and the short mean free path in nanowires, metallic contacts have to be placed in close proximity and form an essential part of any nanowire device. Different to QPCs in 2D electron gases, the contacts can therefore significantly influence device performance. This is particularly relevant in InSb, where an intrinsic surface depletion layer [18] makes it difficult to achieve homogeneous and transparent contacts. The Sulfur residues dope the nanowire surface and help to avoid a depletion layer [19]. The thickness and homo-
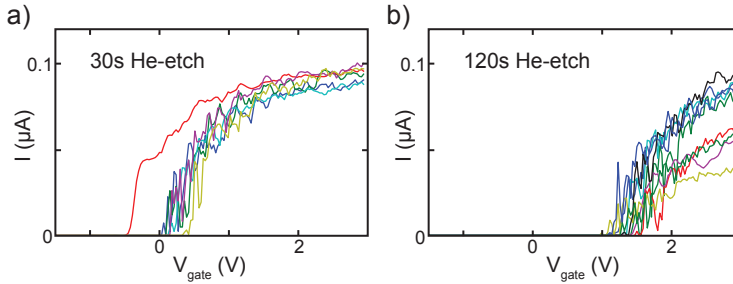
Figure 4.2: Pinch-off traces taken at $V_{sd} = 1\,\text{mV}$ show the influence of variations in the He dry-etch step. Longer etch times clearly shift $V_{threshold}$ to more positive values. **a)** 30 s **b)** 120 s.

geneity of this doping layer are influenced by the the dry etch processes before and after sulfur passivation (step 2 and 5).

4.3.1. HE-ETCH

The He-etch in step 5 has a very low etch rate and is selective enough to clean exposed surfaces without excessively damaging the nanowire and without fully removing the sulfur doping layer. Figure 4.2 directly compares two device batches fabricated with a 30 s and a 120 s long He-etch, while all other steps remained fixed. Longer etch times shift V_{th} by ~ 1 V to positive voltages which indicates a strong reduction of the surface doping layer. Additionally the spread of the saturation current is significantly increased after 2 min etching and reduces for some devices to more than half the value found for 30 s. This confirms the importance of the sulfur layer and demonstrates that shorter etching times are preferable.

4.3.2. DESCUM

PMMA resist will always leave small residues inside exposed areas even for a well calibrated development recipe. It is important to remove these residues before contact preparation and the use of an O_2 plasma is a common way of doing this. The plasma creates mono-atomic oxygen which reacts strongly with the organic resist molecules. A well configured process etches the resist uniformly at a slow rate (1–2 nm/min). This is enough to remove residues and at the same time sufficiently slow to preserve any patterns in the resist and to avoid excessive oxidation of exposed surfaces. On a Si_3N_4 dielectric the oxidation creates a hydrophilic surface which makes resist adhesion difficult and causes cracks to appear which shorted a large number of devices. To circumvent the adhesion problems two different approaches have been tried.

Figure 4.3 shows the effect of replacing the O_2-plasma by Ar-plasma, a mix of Ar and O_2-plasma (ratio of 4 : 1), and He milling. These alternative methods etch physically (Ar and He) or combine reactive with physical etching (Ar/O_2) and therefore reduce the surface oxidation of Si_3N_4. However, they also influence the device performance especially for Ar and Ar/O_2 etching (Fig. 4.3a,b). Some devices show a quality comparable to the original recipe (Fig. 4.2a), but for most devices V_{th} is shifted by several volt and I_s is reduced. Using a He-etching (Fig. 4.3c) shows a device performance which is almost com-

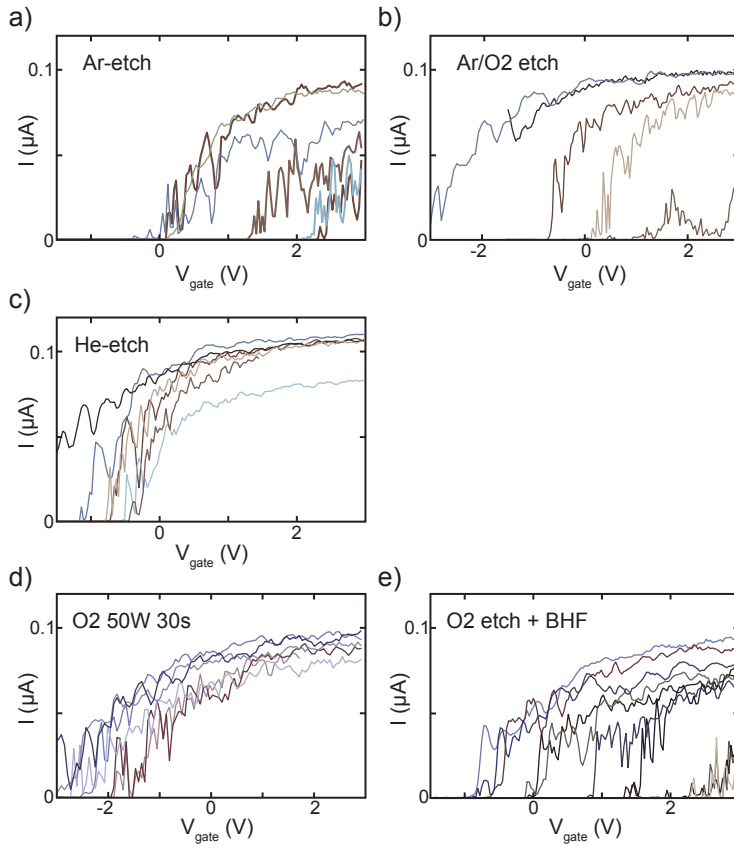Figure 4.3: Variations in the O_2 descum. Pinch-off traces show how changes in the descum step influence pinch-off traces. **a)** O_2 descum for 60 s, 100 W power and 200 sccm flow. **b)** O_2 descum for 30 s, 50 W power and 200 sccm flow. **c)** O_2 descum for 60 s, 100 W power and 200 sccm flow followed by a 30 s dip in buffered Hydrofluoric acid (BHF) to remove SiO_2 from the substrate surface.

parable to the original O_2-plasma recipe. While V_{th} is varying more than in Fig. 4.2a), the saturation current I_s is very homogeneous and conductance fluctuations at higher gate voltage are reduced. As a second approach changes to the O_2-plasma were investigated. Reducing the power and etch time gives comparable results with a more negative V_{th} (Fig. 4.3d). Buffered hydrofluoric acid (BHF) selectively etches SiO_2. Adding a 30 s etch after the normal O_2-plasma successfully prevented resist delamination, but it also caused a deteriorated device performance (Fig. 4.3e). In summary only the He-etch could produce results comparable to the original O_2-plasma recipe. This comes at the cost of longer process time because the He-etching step involves longer pumping times (~ 30 min).

4.4. NANOWIRE CHANNEL

A clean nanowire metal interface helps to maximize the transmission probability between the contacts and individual nanowire subbands. Surface states along the QPC channel provide another source of electron scattering [20–22]. Because of the high surface to volume ratio of 1D structures, electrons are very sensitive to the surrounding environment. Defects in the nanowire oxide, charge fluctuations in the gate dielectric, fabrication residues, and surface adsorbents all influence the final device quality. Additionally, polar molecules such as adsorbed water which rearrange when changing V_g, contribute to gate jumps and gate hysteresis [1, 20, 23].

4.4.1. GATE DIELECTRIC

To prevent shorts between the back-gate and the nanowire, a dielectric with low leakage current and high break through voltage is necessary. A high dielectric constant helps additionally by increasing the gate efficiency. Materials with rough surfaces can trap fabrication residues and defects inside the dielectric will act as a source of charge noise. Figure 4.4 shows a comparison of three QPCs fabricated on different dielectrics. The most commonly used substrate in our group is n^{++}-Si covered with 285 nm of thermally grown SiO_2 (Fig. 4.4 a,d). Considerable improvements in data quality could be achieved by using metallic bottom gates covered by exfoliated hexagonal Boron nitride (hBN) (4.4b,e). It is an ideal dielectric for nanowire devices because of its chemical stability, high breakdown voltage and atomic flatness [24] in combination with a well established dry transfer process [25]. Exfoliating hBN gives flakes with a thickness varying from 10 nm to 50 nm and flake sizes of tens of μm. For helical gap measurements it is important to have precise control of the dielectric thickness as discussed in chapter 6. With hBN this requires a time consuming search for flakes with the correct thickness. As an alternative dielectric we therefore use high quality Si_3N_4 grown by low pressure chemical vapor deposition (LPCVD) which allows scalable and controlled growth with sub-nanometer precision in the thickness. QPC measurements (Fig. 4.4c,f) show that the quality of Si_3N_4 is comparable to hBN. A 20 nm thick dielectric can withstand voltage differences of more than 15 V without breaking down. The biggest difficulty with using Si_3N_4 is poor adhesion of PMMA resist, as mentioned above. Bare Si_3N_4 normally shows good adhesion. However, oxidation of the Si_3N_4 surface, either in atmosphere or during the O_2-plasma step, induces surface charges which make the surface hydrophilic and repel PMMA. AR 300-80
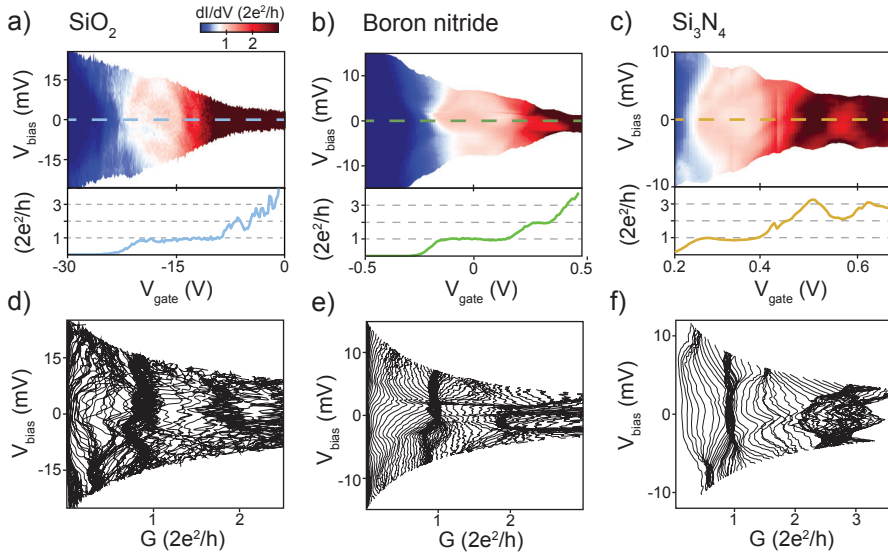
Figure 4.4: Comparison of gate dielectrics. QPCs with similar contact spacing and identical contact preparation fabricated on **a),d)** SiO$_2$, **b),e)** hexagonal Boron Nitride, and **c),f)** Si$_3$N$_4$. **a),b),c)** Colorplot of the differential conductance as function of bias voltage, V_{sd} and gate voltage, V_g. Linecuts along $V_{sd} = 0$ mV are shown in the bottom panels **d),e),f)** Linecuts of the differential conductance at fixed V_g.
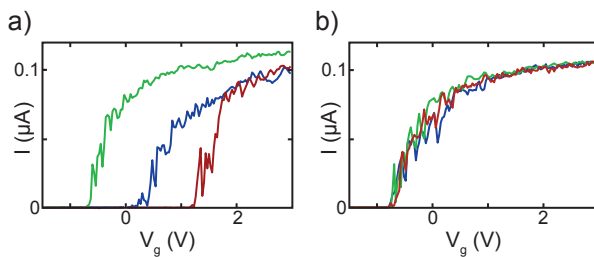
Figure 4.5: Gate hysteresis induced by the substrate surface. **a)** Three gate traces of the same device on a substrate covered with adhesion promoter AR 300-80 show strong hysteresis. The blue trace is taken immediately after cool down, the green trace after ramping the back-gate to $V_g = 14$ V and the red trace after ramping the back-gate to $V_g = -14$ V. **b)** Gate traces of the same device device on a substrate without AR 300-80 show no hysteresis. Traces taken after setting the back-gate to -14 V (red), 0 V (blue) and 14 V (green).

is an adhesion promoter which can be spin-coated on a substrate and, by reacting with SiO, forms a very stable, chemically bonded monolayer on the surface. While this successfully solved the resist delamination, conductance measurements of QPC devices on substrates treated with AR 300-80 (Fig. 4.5) show that even a single monolayer is enough to induce strong gate hysteresis.

4.4.2. Post-processing

We find that extended exposure to atmosphere after contact fabrication reduces the contact quality. Most likely these aging effects are due to reoxidation and surface adsorption. The devices are therefore mounted and bonded as fast as possible and evacuated for several hours to remove surface adsorbents [1, 26, 27]. Figure 4.6 shows the strong effect that different pumping durations can have. One batch of nanowire QPCs was first measured after 12 h, 12 + 72 h and 12 + 72 + 24 h pumping. The first cool down with short pumping (Fig. 4.6a) shows large spread between individual pinch-off traces. V_{th} varies by almost 2 V, I_s ranges from ~ 0.8 to 1.2 µV and individual traces are dominated by conductance fluctuations. After pumping all devices for additional 72 h they improve greatly (Fig. 4.6b). Now all devices perform comparable to the best device in the first cool down. Conductance fluctuations are reduced and variations in V_{th} and I_s are down to ~ 0.3 V and ~ 0.2 µA. Adding another thermal cycle with 24 h additional pumping time (without breaking the vacuum in between) doesn't improve performance further, but on average gives a small increase in conductance fluctuations and in the variations of V_{th} and I_s (Fig. 4.6c). Finally we look at a single QPC device with 240 nm contact spacing and compare measurements after each pumping step in Figure 4.6d-f). In the first measurement (Fig. 4.6d) the device conductance is dominated by fluctuations and no clear conductance plateaus are visible even at high magnetic fields. In the second cool down (Fig. 4.6e), after 12 + 72 h pumping, the conductance at low magnetic fields is dominated by Fabry-Perot resonances but now the two first conductance plateaus can be identified at 1 and 2 · G_0. These plateaus become clearer at higher magnetic fields where conductance oscillations decrease. After the third pumping step the conductance plateaus become even clearer (Fig. 4.6f). Now the first two plateaus are visible from 0 T on and remain flat and free of resonances or oscillations throughout the full magnetic field range. These observations agree with earlier studies of nanowire mobility [1, 22, 26], and demonstrate that samples fabricated with the optimized contact recipe are still limited by scattering sources along the nanowire channel which can be removed by evacuation. Water naturally adsorbs to the nanowire and substrate surface during and after fabrication. The polar molecules reorient in the electric-field of the bottom gate and additionally attract other charged particles from the environment. This can cause local doping on the nanowire surface and variations of the gate potential which decrease device performance. Similar effects can be cause by organic fabrication residues like acetone, IPA or PMMA. For some devices a strong indication for fabrication residues could be found with a scanning electron microscope (SEM). Figure 4.7 shows high resolution images of one device first immediately after liftoff and then after measurements which included several days of pumping. White dots on the nanowire, indicated by arrows, can be seen after liftoff and disappear in the second images. Such obvious contaminations only show up in some of the fabrication runs and their exact origin and composition is unknown.
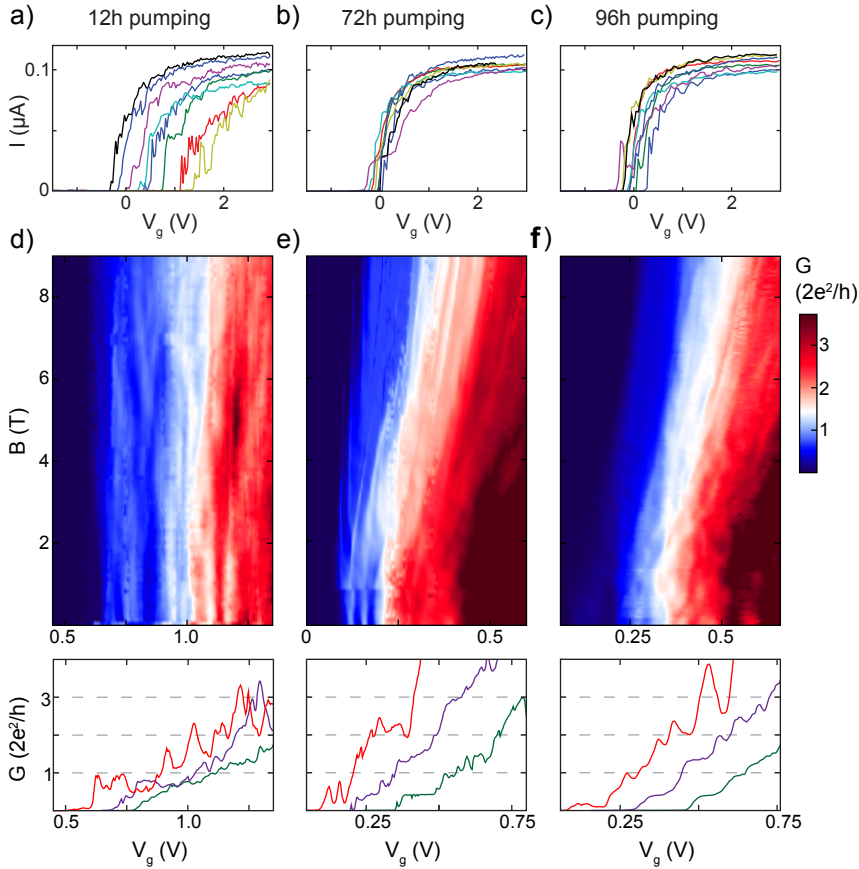
Figure 4.6: Influence of pumping duration before device cool down. One chip with 8 QPCs was repeatedly measured after pumping on the chip for **a),d)** 12 h, **b),e)** 12 + 72 h, and **c),f)** 12 + 72 + 24 h. Measurements were performed in 3 consecutive cool downs without exposing the chip to atmosphere in between. **a, b, c)** Conductance traces taken at $V_{sd} = 1$ mV. **d, e, f)** Differential conductance dI/dV measured as function of magnetic field. The bottom panels show linecuts taken at 0 T (red), 4.5 T (purple) and 9 T (green) offset in V_g by 0.2 V for clarity.
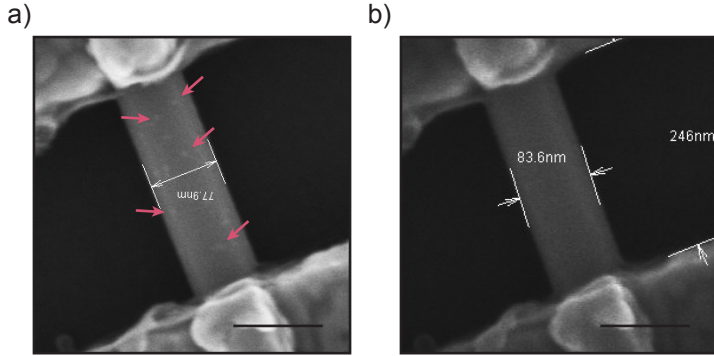
Figure 4.7: Fabrication residues. Electron microscope image of a nanowire QPC taken **a)** before and **b)** after measurements. Fabrication residues on the nanowire surface (indicated by arrows) are visible as white dots in **a)** and disappear in **b)**. Scale bar is 100 nm.

4.5. CONCLUSIONS

The improvements discussed in this chapter are essential for the results presented in chapters 5 and 6. Maintaining high device quality and fabrication yield requires reliable control of every fabrication step and it is important to recognize and keep track of any changes. The O_2-plasma in particular has been a source of sudden changes of the etch rate which delayed fabrication by several months. Large improvements were possible by changing the gate dielectric and by extending sample evacuation. This suggests that the dominating source of electron backscattering is due to defects in the dielectric and fabrication residues in nanowire environment. These improvements allowed the observation of conductance quantization in devices with up to 400 nm channel length. To further enhance the electron mean free path a better understanding of the remaining scattering sources is needed. Remaining surface residues which cannot be removed by pumping alone could be one source. Another possibility are defects in the nanowire surface oxide. These effects could be minimized by encapsulating the full nanowire either before fabrication or ideally in-situ directly after nanowire growth. For example, epitaxially grown contacts have demonstrated enormous improvements for InAs nanowires [28] and are also promising for InSb wires. Recent atom probe spectroscopy measurements of InSb nanowires found a large Arsenic content of up to 4 % [29] which could also contribute to electron scattering.

REFERENCES

[1] Ö. Gül, D. J. van Woerkom, I. van Weperen, D. Car, S. R. Plissard, E. P. A. M. Bakkers, and L. P. Kouwenhoven, "Towards high mobility insb nanowire devices," *Nanotechnology*, vol. 26, no. 21, p. 215202, 2015.

[2] S. Nadj-Perge, V. S. Pribiag, J. W. G. Van den Berg, K. Zuo, S. R. Plissard, E. P. A. M. Bakkers, S. M. Frolov, and L. P. Kouwenhoven, "Spectroscopy of spin-orbit quantum bits in indium antimonide nanowires," *Phys. Rev. Lett.*, vol. 108, no. 16, p. 166801, 2012.

[3] I. van Weperen, S. R. Plissard, E. P. A. M. Bakkers, S. M. Frolov, and L. P. Kouwenhoven, "Quantized conductance in an insb nanowire," *Nano Lett.*, vol. 13, no. 2, pp. 387–391, 2012.

[4] H. A. Nilsson, P. Caroff, C. Thelander, M. Larsson, J. B. Wagner, L.-E. Wernersson, L. Samuelson, and H. Q. Xu, "Giant, level-dependent g factors in insb nanowire quantum dots," *Nano Lett.*, vol. 9, no. 9, pp. 3151–3156, 2009. PMID: 19736971.

[5] J. W. G. Van den Berg, S. Nadj-Perge, V. S. Pribiag, S. R. Plissard, E. P. A. M. Bakkers, S. M. Frolov, and L. P. Kouwenhoven, "Fast spin-orbit qubit in an indium antimonide nanowire," *Phys. Rev. Lett.*, vol. 110, no. 6, p. 066806, 2013.

[6] R. Winkler, S. Papadakis, E. De Poortere, and M. Shayegan, *Spin-Orbit Coupling in Two-Dimensional Electron and Hole Systems*, vol. 41. Springer, 2003.

[7] X. W. Zhang and J. B. Xia, "Rashba spin-orbit coupling in insb nanowires under transverse electric field," *Phys. Rev. B*, vol. 74, p. 075304, Aug 2006.

[8] I. Van Weperen, B. Tarasinski, D. Eeltink, V. Pribiag, S. Plissard, E. Bakkers, L. Kouwenhoven, and M. Wimmer, "Spin-orbit interaction in insb nanowires," *Phys. Rev. B*, vol. 91, no. 20, p. 201413, 2015.

[9] S. Nadj-Perge, S. M. Frolov, E. P. A. M. Bakkers, and L. P. Kouwenhoven, "Spin-orbit qubit in a semiconductor nanowire," *Nature*, vol. 468, no. 7327, pp. 1084–1087, 2010.

[10] V. S. Pribiag, S. Nadj-Perge, S. M. Frolov, J. W. G. van den Berg, I. van Weperen, S. R. Plissard, E. P. A. M. Bakkers, and L. P. Kouwenhoven, "Electrical control of single hole spins in nanowire quantum dots," *Nat. Nanotechnol.*, vol. 8, no. 3, pp. 170–174, 2013.

[11] V. Mourik, K. Zuo, S. M. Frolov, S. R. Plissard, E. P. A. M. Bakkers, and L. P. Kouwenhoven, "Signatures of majorana fermions in hybrid superconductor-semiconductor nanowire devices," *Science*, vol. 336, no. 6084, pp. 1003–1007, 2012.

[12] M. T. Deng, C. L. Yu, G. Y. Huang, M. Larsson, P. Caroff, and H. Q. Xu, "Anomalous zero-bias conductance peak in a nb–insb nanowire–nb hybrid device," *Nano Lett.*, vol. 12, no. 12, pp. 6414–6419, 2012.

4

[13] M. Deng, C. Yu, G. Huang, M. Larsson, P. Caroff, and H. Xu, "Parity independence of the zero-bias conductance peak in a nanowire based topological superconductor-quantum dot hybrid device," *Sci. Rep.*, vol. 4, 2014.

[14] H. O. H. Churchill, V. Fatemi, K. Grove-Rasmussen, M. T. Deng, P. Caroff, H. Q. Xu, and C. M. Marcus, "Superconductor-nanowire devices from tunneling to the multi-channel regime: Zero-bias oscillations and magnetoconductance crossover," *Phys. Rev. B*, vol. 87, p. 241401, Jun 2013.

[15] Ö. Gül, H. Zhang, F. K. de Vries, J. van Veen, K. Zuo, V. Mourik, S. Conesa-Boj, M. Nowak, D. van Woerkom, M. Quintero-Perez, M. Cassidy, A. Geresdi, S. Koelling, D. Car, S. Plissard, E. P. Bakkers, and L. P. Kouwenhoven, "Hard superconducting gap in insb nanowires," *Nano Lett.*, vol. 17, no. 4, pp. 2690–2696, 20107.

[16] S. Chuang, Q. Gao, R. Kapadia, A. C. Ford, J. Guo, and A. Javey, "Ballistic inas nanowire transistors," *Nano Lett.*, vol. 13, no. 2, pp. 555–558, 2013.

[17] L. P. Kouwenhoven, B. J. van Wees, C. J. P. M. Harmans, J. G. Williamson, H. van Houten, C. W. J. Beenakker, C. T. Foxon, and J. J. Harris, "Nonlinear conductance of quantum point contacts," *Phys. Rev. B*, vol. 39, pp. 8040–8043, Apr 1989.

[18] P. D. C. King, T. D. Veal, M. J. Lowe, and C. F. McConville, "Surface electronic properties of clean and s-terminated insb(001) and (111)b," *J. Appl. Phys.*, vol. 104, no. 8, 2008.

[19] H. Zhang, Ö. Gül, S. Conesa-Boj, K. Zuo, V. Mourik, F. K. de Vries, J. van Veen, D. J. van Woerkom, M. P. Nowak, M. Wimmer, *et al.*, "Ballistic majorana nanowire devices," *arXiv preprint arXiv:1603.04069*, 2016.

[20] D. Wang, Y.-L. Chang, Q. Wang, J. Cao, D. B. Farmer, R. G. Gordon, and H. Dai, "Surface chemistry and electrical properties of germanium nanowires," *J. Am. Chem. Soc.*, vol. 126, no. 37, pp. 11602–11611, 2004.

[21] E. Halpern, G. Elias, A. V. Kretinin, H. Shtrikman, and Y. Rosenwaks, "Direct measurement of surface states density and energy distribution in individual inas nanowires," *Appl. Phys. Lett.*, vol. 100, no. 26, 2012.

[22] S. A. Dayeh, C. Soci, P. K. L. Yu, E. T. Yu, and D. Wang, "Transport properties of inas nanowire field effect transistors: The effects of surface states," *Journal of Vacuum Science & Technology B: Microelectronics and Nanometer Structures Processing, Measurement, and Phenomena*, vol. 25, no. 4, pp. 1432–1436, 2007.

[23] W. Kim, A. Javey, O. Vermesh, Q. Wang, Y. Li, and H. Dai, "Hysteresis caused by water molecules in carbon nanotube field-effect transistors," *Nano Lett.*, vol. 3, no. 2, pp. 193–198, 2003.

[24] C. Dean, A. Young, I. Meric, C. Lee, L. Wang, S. Sorgenfrei, K. Watanabe, T. Taniguchi, P. Kim, K. Shepard, and J. Hone, "Boron nitride substrates for high-quality graphene electronics," *Nat. Nanotechnol.*, vol. 5, no. 10, pp. 722–726, 2010.

[25] A. Castellanos-Gomez, M. Buscema, R. Molenaar, V. Singh, L. Janssen, H. S. J. van der Zant, and G. A. Steele, "Deterministic transfer of two-dimensional materials by all-dry viscoelastic stamping," *2D Mater.*, vol. 1, no. 1, p. 011002, 2014.

[26] A. V. Kretinin, R. Popovitz-Biro, D. Mahalu, and H. Shtrikman, "Multimode fabry-pérot conductance oscillations in suspended stacking-faults-free inas nanowires," *Nano Lett.*, vol. 10, no. 9, pp. 3439–3445, 2010.

[27] S. Nadj-Perge. PhD thesis, TU Delft, 12 2010.

[28] W. Chang, S. M. Albrecht, T. S. Jespersen, F. Kuemmeth, P. Krogstrup, J. Nygård, and C. M. Marcus, "Hard gap in epitaxial semiconductor–superconductor nanowires," *Nat. Nanotechnol.*, vol. 10, no. 3, pp. 232–236, 2015.

[29] S. Koelling, A. Li, A. Cavalli, S. Assali, D. Car, S. Gazibegovic, E. P. Bakkers, and P. M. Koenraad, "Atom-by-atom analysis of semiconductor nanowires with parts per million sensitivity," *Nano Lett.*, vol. 17, no. 2, pp. 599–605, 2017.

4

5

CONDUCTANCE QUANTIZATION AT ZERO MAGNETIC FIELD IN INSB NANOWIRES

J. Kammhuber, M. C. Cassidy, H. Zhang, Ö. Gül, F. Pei, M. W. A. de Moor, B. Nijholt, K. Watanabe, T. Taniguchi, D. Car, S. R. Plissard, E. P. A. M Bakkers and L. P. Kouwenhoven

Ballistic electron transport is a key requirement for the existence of a topological phase transition in proximitized InSb nanowires. However, measurements of quantized conductance as direct evidence of ballistic transport have so far been obscured due to the increased chance of backscattering in one-dimensional nanowires. We show that by improving the nanowire-metal interface as well as the dielectric environment we can consistently achieve conductance quantization at zero magnetic field. Additionally, studying the subband evolution in a rotating magnetic field reveals an orbital degeneracy between the second and third subbands for perpendicular fields above 1 T.

5.1. Introduction

Semiconducting nanowires made from InAs and InSb are prime candidates for the investigation of novel phenomena in electronic devices. The intrinsic strong spin-orbit interaction (SOI) and large g-factor combined with flexible fabrication has resulted in these materials being investigated for applications in quantum computing [1–3], spintronics [4–6], and Cooper pair splitters [7, 8]. More recently, these nanowires have been investigated as solid-state hosts for Majorana zero modes (MZMs) [9–12]. By bringing a one-dimensional (1D) nanowire with strong SOI into close contact with a superconductor under an external magnetic field, a region with inverted band structure emerges, creating MZMs at its ends. Together with strong SOI and induced superconductivity, a key requirement for MZMs is quasi-ballistic electron transport along the length of the proximitized region in the nanowire, with a controlled odd number of occupied modes [13]. In the absence of scattering, the motion of 1D confined electrons will be restricted to discrete energy bands resulting in quantized conductance plateaus [14, 15]. Measurements of quantized conductance in the nanowires therefore provide direct evidence for controlled mode occupation, as well as ballistic transport in these nanowires.

Although now routine in gate defined quantum point contacts (QPC) in two dimensional electron gases (2DEG) [14–18] quantized conductance in one dimensional semiconductor nanowires is more difficult to achieve. In a 1D nanowire, scattering events along the electrons path to and through the constriction between the source and drain contacts have an increased probability of reflection, obscuring the observation of quantized conductance [19]. These scattering events may be due to impurities and imperfections in the crystal lattice, or due to surface states that create inhomogeneities in the local electrostatic environment [20]. A Schottky barrier between the nanowire and metallic contacts will result in additional backscattering events, further smearing out the quantized conductance plateaus. To date, quantized conductance in InSb nanowires has only been observed at high magnetic fields (> 4 T), where electron backscattering is strongly suppressed [19]. No quantization has been observed in InSb for magnetic fields below 1 T, where the topological transition is expected to take place [9]. Here we demonstrate conductance quantization in InSb nanowires at zero magnetic field. We have developed a robust fabrication recipe for observing quantized conductance by optimizing both the metal-nanowire contact interface and dielectric environment through the use of hexagonal boron nitride (hBN) as a gate dielectric. We study the evolution of the quantized conductance plateaus with both source-drain bias as well as magnetic field, and extract values for the Landé g-factor of the first three subbands in the nanowire. Additionally, we observe an orbital energy degeneracy of the second and third subbands at finite magnetic fields applied perpendicular to the nanowire.

5.2. Device Layout and Characterization

Figure 5.1 a) shows a cross-sectional view of our devices. They consist of an intrinsic Si-substrate with local metallic gates made of Ti/Au (5/10 nm), on top of which a sheet of hexagonal boron nitride (hBN) is mechanically transferred as the dielectric. The chemical stability, atomic flatness, and high breakdown voltage [21], together with the well established dry transfer mechanism [22] make hBN an ideal dielectric for our
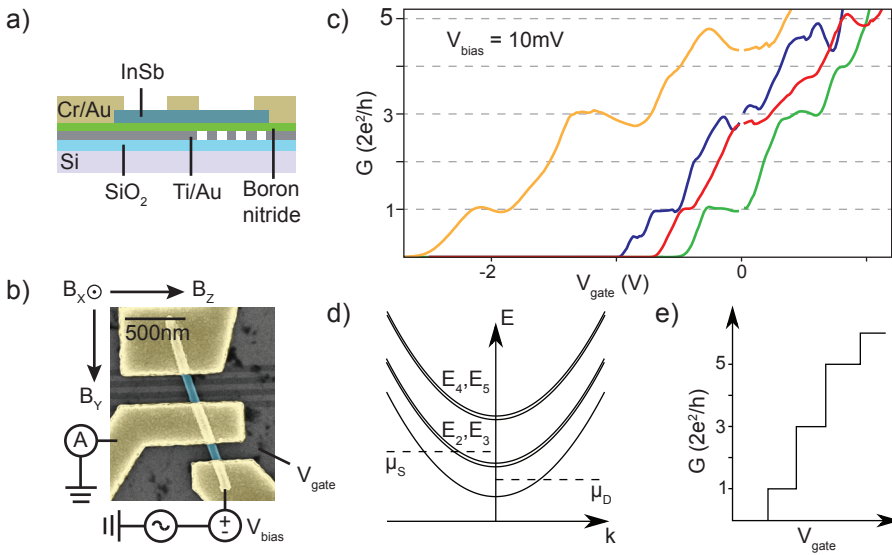
Figure 5.1: **a)** Cross-sectional schematic and **b)** false color SEM image of a typical device. An InSb nanowire (blue) contacted by Cr/Au (yellow) is deposited on Ti/Au metal gates (grey) covered with hexagonal boron nitride (green) as insulating dielectric. **c)** Pinch-off traces of four different devices each showing quantized conductance plateaus at high bias voltage ($V_{bias} = 10\,mV$). **d)** Schematic diagram of the first five subbands in a nanowire. At zero magnetic field, each spin-degenerate subband below the Fermi level contributes a conductance of $G_0 = 2e^2/h$. Due to the rotational symmetry of the nanowires E_2, E_3 and E_4, E_5 are almost degenerate. **e)** Sketch of the expected conductance steps as function of V_{gate} at high bias voltage showing suppression of the second and fourth plateaus due to orbital subband degeneracy.

nanowire devices. InSb nanowires grown by metal-organic vapor phase epitaxy [23, 24] (1–2 μm long and 70–90 nm diameter) are transferred deterministically with a micro-manipulator [25] onto the hBN dielectric. Electrical contacts to the nanowire (evaporated Cr/Au (10/100 nm, 150–400 nm spacing) are defined by electron beam lithography. Before contact deposition, the surface oxide of the nanowires is removed using sulfur passivation [26] followed by a short in situ He-ion mill. Residual sulfur from the passivation step also induces surface doping, which aids contact transparency. Further details of the fabrication are included in the supporting information. A top view scanning electron microscope image of a finished device is shown in Fig. 5.1b). The samples are mounted in a dilution refrigerator with a base temperature of 15 mK and measured using standard lock-in techniques at 73 Hz with an excitation $V_{RMS} = 70 \mu V$. Voltage is applied to the outer contact and current measured through the grounded central contact, while the third, unused contact is left floating. We first characterize each device by sweeping the voltage on the underlying gate V_{gate} at fixed bias voltage $V_{bias} = 10$ mV across the sample. Conductance is obtained directly from the measured current $G = I/V_{bias}$ and an appropriate series resistance is subtracted in each case (see supporting information). Figure 5.1c) plots the conductance of the nanowire as function of gate voltage for four different devices fabricated on the same chip. Devices with both fine gates as well as wide back gates have been measured. We find that while fine gates allow more flexible gating, devices with wide back gates showed more pronounced conductance plateaus even after extensive tuning of the fine gates. Data from additional devices all fabricated on the same chip is included in the supporting information. As seen in Fig. 5.1c) all devices show well defined plateaus at G_0 and $3 G_0$ but the plateaus at $2 G_0$ and $4 G_0$ appear smaller or even completely absent. Unlike QPC's formed in 2DEGs, nanowires possess rotational symmetry. This symmetry can give rise to additional orbital degeneracies in the energies for the 2nd and 3rd as well as the 4th and 5th subband (Fig. 5.1d) [27, 28]. In conductance measurements at finite bias, subbands that are close in energy or degenerate will be populated at similar values in gate voltage giving a double step of $4 \frac{e^2}{h}$ instead of $2 \frac{e^2}{h}$, which explains the suppressed plateaus at 2 and $4 G_0$ (Fig. 5.1e) [29]. To investigate this phenomenon in more detail, we measure the differential conductance $G = dI/dV_{bias}$ as function of gate voltage and bias voltage for one of these devices (corresponding to the green trace in Fig. 5.1c). This data is shown in Fig. 5.2a) as a color plot, with a line cut along zero bias voltage added in the bottom panel. At zero bias voltage an extended plateau is visible at $1 G_0$, together with an additional small plateau at $2 G_0$ which was not visible in the linear conductance data of Figure 5.1c). The existence of this small $2 G_0$ plateau indicates that the device has a small, but finite energy splitting between the second and third subband which was not resolved at high bias. At finite bias voltage the conductance will only be quantized in integer values of G_0 if both μ_{source} and μ_{drain} occupy the same subband. This creates diamond shaped regions of constant conductance indicated by black dotted lines in Fig. 5.2a). At the tip of the diamond the two dotted lines cross when V_{bias} is equal to the subband energy spacing $\Delta E_{subband}$. From this we extract $\Delta E_{subband}$ and the lever-arm η of the bottom gate via $\eta V_{gate} = \Delta E_{subband}$ [30]. A finite magnetic field breaks time reversal symmetry, lifting spin degeneracy and splitting the individual spin subbands $E_{n,\uparrow/\downarrow}$ by the Zeeman energy $E_{Zeeman} = g\mu_B B$. Here μ_B denotes the Bohr magneton and g the Landé g-factor. Ex-
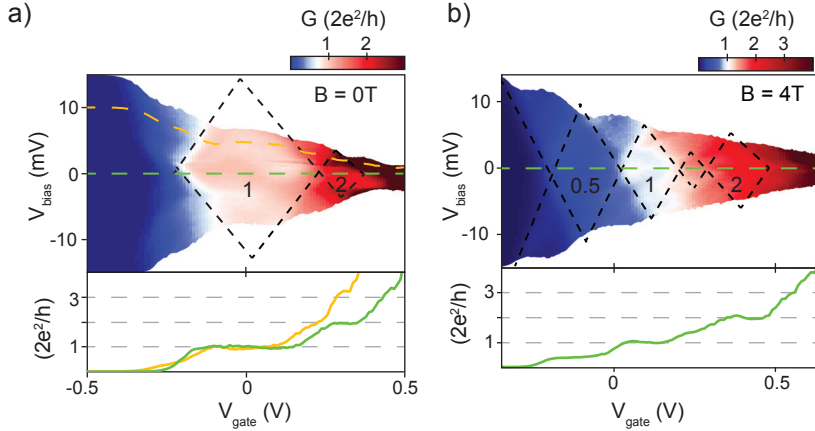
Figure 5.2: Color-plot of the differential conductance $G = dI/dV_{bias}$ as function of V_{bias} and V_{gate} at **a)** $B = 0\,T$ and **b)** $B_Z = 4\,T$. A line cut along zero bias voltage is shown in the bottom panel. Plateaus appear as diamonds and are indicated by black dotted lines.

5

perimentally this splitting manifests as the appearance of additional half integer steps $\frac{N}{2} \cdot 2e^2/h$. At $B = 4\,T$ we clearly observe this for the first subband as shown in Fig. 5.2b) where an additional plateau emerges at $0.5\,G_0$. Similarly, the second subband should also split into two plateaus at 1.5 and $2\,G_0$. However only the $2\,G_0$ plateau is visible, suggesting that an orbital degeneracy between $E_{2,\uparrow}$ and $E_{3,\uparrow}$ remains at finite magnetic field.

5.3. MAGNETIC FIELD EVOLUTION

The full evolution in magnetic field of the conductance and transconductance is shown in Fig. 5.3a,b) and individual line traces of the conductance taken in steps of 1 T are presented in Fig. 5.3c). While the plateau at $1\,G_0$ remains very flat up to high magnetic fields, the second plateau at $2\,G_0$ increases in height for magnetic fields larger than $400\,mT$. Around 1 T two new plateaus emerge with similar slope at 0.5 and $2\,G_0$. These correspond to the lower energy spin subbands $E_{1\uparrow}$ and $E_{2,3\uparrow}$. Here we can clearly see experimentally that the non-degenerate orbital state at zero field transforms into a degenerate orbital state at finite field and that $E_{2,3\uparrow}$ remain degenerate over a magnetic field range of several Tesla. From the individual gate traces we convert the plateau width to energy by using the lever arm η extracted from Figure 5.2. This way we can directly extract the subband spacing $E_{2\uparrow} - E_{1\uparrow}$ and the individual g-factors g_1, $g_{2,3}$ through a linear fit fixed at the origin to $E_{1\downarrow} - E_{1\uparrow}$ and $E_{2,3\downarrow} - E_{2,3\uparrow}$. We find $g_1 = 39 \pm 1$ $g_{2,3} = 40 \pm 1$ and a constant subband spacing $E_{2\uparrow} - E_{1\uparrow} \approx 16\,meV$.

Orbital degeneracy of subbands has previously been observed in metallic point contacts [29] and recently also in passivated narrow InAs nanowires with highly symmetric conducting channels [27]. However, the magnetoconductance of InSb nanowires may deviate significantly from the results found in InAs nanowires. In InAs, Fermi level pinning leads to conduction close to the nanowire surface [31, 32] which strongly influences the subband dispersion in magnetic field [33, 34]. InSb has no surface accumulation

5
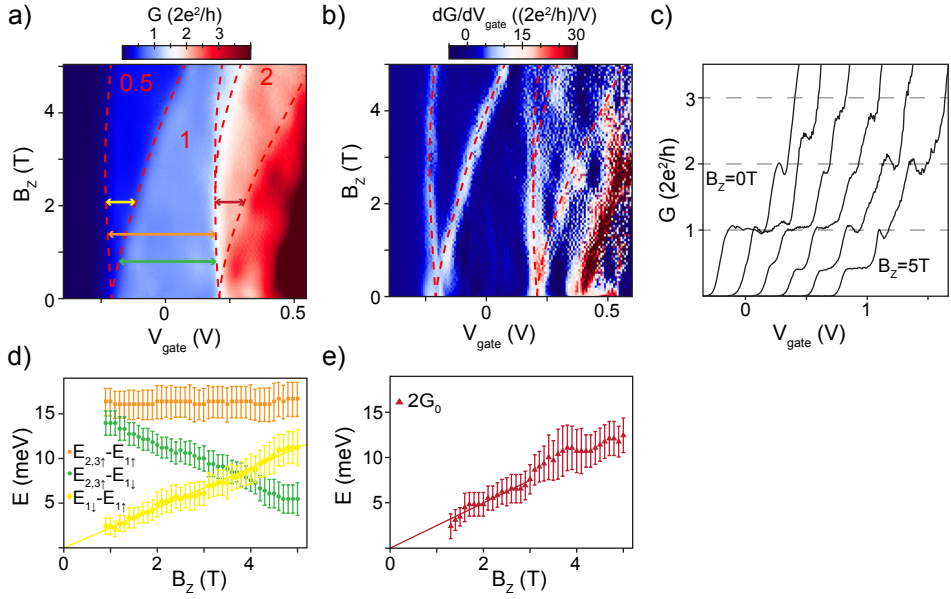
Figure 5.3: a) Differential conductance $G = dI/dV_{bias}$ and **b)** transconductance dG/dV_{gate} as function of magnetic field along B_Z and V_{gate} taken at $V_{bias} = 0\,mV$. The level spacings plotted in d,e) are marked by arrows of corresponding color. Red dashed lines indicating the subband spacing in a,b) are drawn as guide to the eye. **c)** Linecuts of a) in steps of 1 T and offset by 200 mV for clarity. **d)** Energy level spacings of $E_{1\downarrow} - E_{1\uparrow}$ (yellow), $E_{2,3\uparrow} - E_{1\downarrow}$ (green) and $E_{2,3\uparrow} - E_{1\uparrow}$ (orange) extracted from the 0.5 and $1G_0$ plateau in a). A linear fit to $E_{1\downarrow} - E_{1\uparrow}$ fixed at the origin gives the g-factor of the first subband $g_1 = 39 \pm 1$. **e)** Energy spacing of $E_{2,3\downarrow} - E_{2,3\uparrow}$ extracted from the $2G_0$ plateau with $g_{2,3} = 40 \pm 1$.
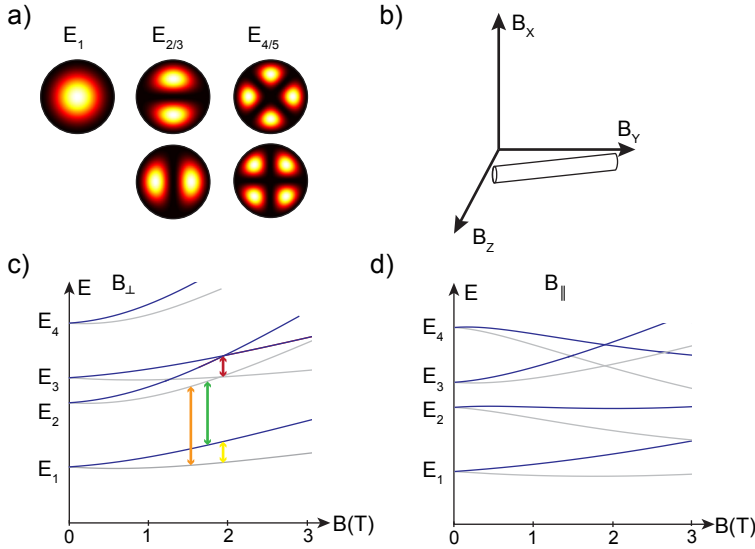
Figure 5.4: **a)** Probability density of the first 5 subbands of a cylindrical nanowire. **b)** Orientation of the nanowire with respect to the magnetic field axes. **c),d)** Numerical simulations of the subband dispersion of a InSb nanowire in c) perpendicular and d) parallel magnetic field.

[35] and the electron wave-function will be more strongly confined in the center of the nanowire. For cylindrical nanowires individual subband wave functions are given by Bessel functions with different orbital angular momentum along the wire (Fig. 5.4a), and numerical simulations of wires with a hexagonal cross-section show qualitatively similar results [28, 36]. An additional magnetic field will add Zeeman splitting, but also causes orbital effects which can substantially change the subband dispersion depending on the orientation of the field with respect to the nanowires axis [37]. Numerical simulations of nanowires in a magnetic field show that orbital effects strongly depend on the magnetic field orientation and can dominate the subband dispersion, leading to a decrease of the energy splitting between E_2 and E_3 [37]. Furthermore these simulations also show that the orbital effects can strongly influence the phase diagram of MZMs [37]. Using the model of ref. 37 with the parameters of our device (wire radius: 35 nm; g-factor: 40) we simulate this change in the subband dispersion for a magnetic field perpendicular (Fig. 5.4c) and parallel (Fig. 5.4d) to the nanowire. A perpendicular magnetic field causes $E_{2,\uparrow}$ and $E_{3,\uparrow}$ to shift higher and closer in energy, while a parallel magnetic field increases the energy splitting of the higher subbands E_2 and E_3, due to their different orbital angular momentum. Experimentally we test this by rotating the direction of the magnetic field, as shown in Fig. 5.5. When aligning the magnetic field along B_Z (almost perpendicular to the nanowire, Fig. 5.5a,b), a small splitting appears at the beginning of the first plateau for fields above $B_Z = 0.6$ T, marking the onset of the 0.5-plateau. In contrast, in the second plateau the splitting only starts above 1 T and the line-cuts (Fig. 5.5b) show that the new plateau emerges at $2 G_0$. Similarly, for a magnetic field along B_X (Fig. 5.5c,d), a new plateau emerges around $B_X = 0.6$ T in the first step but not in the second. However,

5

5
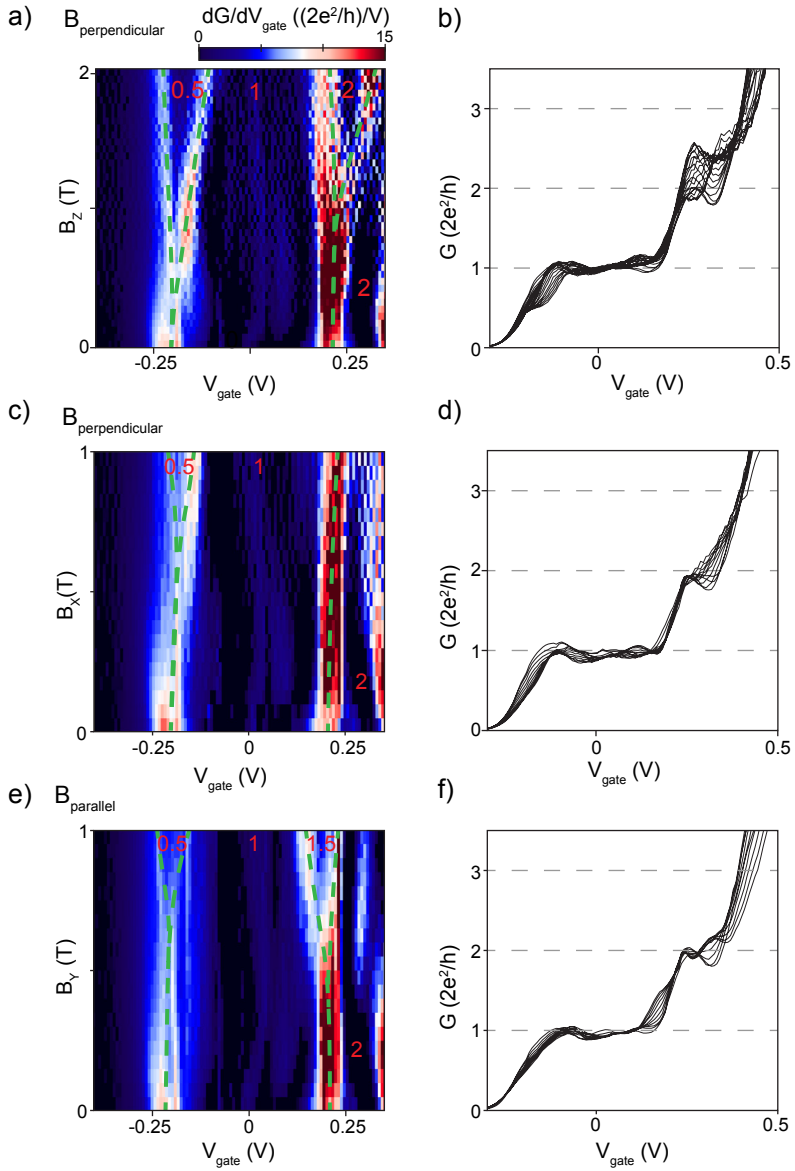
Figure 5.5: Transconductance dG/dV$_{gate}$ and differential conductance G for three different directions of the magnetic field all taken at V$_{bias}$ = 0 mV. Green dashed lines indicating the subband spacing in a,c,e) are drawn as guide to the eye and red numbers label the height of the conductance plateaus. B$_Z$ is increased from 0–2 T and B$_{X,Y}$ from 0–1 T. **a),b)** Magnetic field aligned along B$_Z$. **c),d)** Magnetic field aligned along B$_X$. **e),f)** Magnetic field aligned along B$_Y$.

for the magnetic field aligned along B_Y (mostly parallel to the nanowire) shown in Fig. 5.5e,f) we do see a clear difference. Now two new plateaus emerge almost simultaneously around $B_Y \approx 0.75\,T$, with the second plateau at 1.5 and not at $2\,G_0$, in agreement with the expected behavior due to orbital effects.

5.4. Conclusions and Outlook

In conclusion we achieved substantial improvements in electrical transport measurements of InSb nanowires by using a high quality hBN dielectric and clearly demonstrated conductance quantization at zero magnetic field, as well as degenerate subbands at magnetic field above 1 T. In the future these, improvements will allow the more detailed investigation of features in the 1st plateau, such as signatures of a helical gap [38, 39], or the presence of a 0.7 anomaly [40–42]. The large SOI in our InSb nanowire strongly influences the electron dispersion relation and the tunability with magnetic field could add new insight into the underlying physics [43]. We did not see any clear features related to the 0.7-anomaly in our devices. However, the 0.7 state becomes more pronounced at higher temperatures [40]. A more detailed study of the temperature dependence of conductance quantization may reveal more information about the existence of this intriguing state in nanowire QPCs.

5.5. Supplementary Information

5.5.1. Fabrication Recipe

Substrate preparation : A substrate made of intrinsic Si with 285 nm thermal SiO_2 and alignment markers made of 10 nm Ti + 80 nm Au was used.

Fine gate deposition :

- Resist spinning: PMMA 950 K A2 at 5000 rpm; bake for 60 min at 175 °C
- Writing of gate patterns using ebeam lithography.
- Developing: 60 s MIBK:IPA (1:3); 60 s IPA.
- Deposition: Evaporation of 5 nm Ti and 10 nm Au.
- Lift-off in hot (50 °C) Acetone for 2 hours.

Dielectric deposition : Hexagonal boron nitride (hBN) was transferred on top of the fine gates in a setup similar to ref 22 which also contains a more detailed description of the process.

- Exfoliated hBN flakes are transferred on a glass substrates covered with a PDMS film.
- Identification of fitting hBN flakes (20–25 nm typical thickness), alignment to the fine gates and transfer onto the chip are all done with an optical microscope.
- Cleaning of PDMS residues with oxygen plasma (60 s, 1 mBar, 600 W).
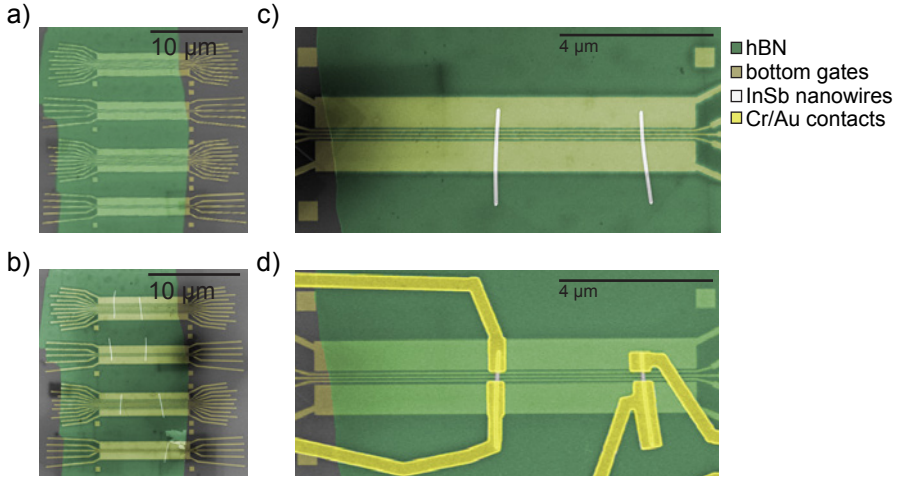
Figure 5.6: False color SEM images illustrating the fabrication process. **a)** Ti/Au bottom gates (dark yellow) with a hBN flake (green) on top. **b),c)** InSb nanowires (white) deposited on hBN and aligned perpendicular to the fine gates. **d)** Two finished devices after evaporation of Cr/Au contacts (light yellow).

Wire deposition : InSb nanowires are transferred onto the chip with fine gates covered by hBN under an optical microscope equipped with a fine needle (250 nm diameter) attached to a micro-manipulator similar to the setup described in ref 25.

Contact deposition :

- SEM imaging of nanowires for contact design.
- Resist spinning: PMMA 950 K A4 at 4000 rpm; bake for 15 min at 175 °C.
- Writing of contact patterns using ebeam lithography.
- Developing: 60 s MIBK:IPA (1:3); 60 s IPA.
- Sulfur passivation as described in ref. 26: Diluted ammonium polysulfide $(NH_4)_2 S_x$ solution (3.5 ml $(NH_4)_2 S$ mixed with 290 mg sulfur then diluted with DI-water at a ratio of $1 : 200$) for 30 min at 60 °C. Rinse in DI water and transfer chip to the evaporator in a non-transparent beaker filled with IPA.
- 30 s He-etch with a Kauffman ion source.
- Deposition: Evaporation of 10 nm Cr and 90 nm Au.
- Lift-off in hot (50 °C) Acetone for 2 h.

5.5.2. CONTACT RESISTANCE

After subtracting a series resistance of 5.6 kΩ for filters and 3 kΩ for the measurement setup all data was corrected for an additional device dependent contact resistance R_{device}. This accounts for the resistance of the metallic contacts as well as the resistance of the metal-nanowire interface. R_{device} was chosen to fit the height of the $1\,G_0$-plateau to

$2e^2/h$ at high magnetic fields B = 5 T and then used for all other scans of the same device. Typical values of R_{device} are 3–6 kΩ and for the device presented in Fig. 5.2 – 5.5 we subtracted $R_{device} = 6.5$ kΩ.

5.5.3. NUMERICAL SIMULATIONS

Numerical Simulations of the subband dispersion have been performed using the Kwant code [44] with the model described in ref 37. The model consisted of a hexagonal nanowire with radius r = 35 nm and g-factor g = 40 and includes spin-orbit interaction as well as orbital effects. The source code can be found in the supplementary materials of ref 37.

5.5.4. ADDITIONAL DATA OF THE MAIN DEVICE AND LEVER ARM EXTRACTION

In addition to the data shown in the main text we also took measurements at intermediate values of magnetic field. Conductance, transconductance and gate traces as function of bias voltage and gate voltage are shown in Figures 5.7 and 5.8. From this we extracted the gate lever arm η via $V_{gate}\eta = \Delta E_{subband}$ and find $\eta = 40 \pm 3$ meV/V. The data also shows that higher conductance plateaus are not always clearly resolved in the low bias lock-in measurements. We also observe this in other devices and it is probably due to remaining imperfections in the device which show up stronger in the less-averaging low bias measurements.

5.5.5. DATA OF ADDITIONAL DEVICES

All together we fabricated eight working devices on the same chip and data for four of those is shown in Figure 1 of the main text. For completeness the I-V traces of all eight devices is shown in Figure 5.9. As mentioned in the main text, devices with both fine and wide bottom gates were fabricated. Fine gates had a width of 50 nm and pitch of 100 nm, wide gates had a width of 800 nm effectively extending through the full QPC channel and under the metallic contacts. Fine gates allow more flexibility in gating, but the gate potential will be less homogeneous (when using multiple fine gates) with a sharper onset. This can increase the chance of back reflection and give more pronounced Fabry-Perot oscillations. Wide bottom gates on the other hand have a smoother onset of the potential profile which increases the QPC transmission and visibility. Data of an additional device with fine gates is shown in Figure 5.10.

5.5.6. DEVICES ON SiO_2 DIELECTRIC

To compare the influence of the gate dielectric we also fabricated identical devices with 285 nm SiO_2 as dielectric. These devices also showed clear signs of conductance quantization as demonstrated in Figure 5.11. Data of two QPCs with identical contact spacing but different dielectric is shown in Figure 5.12 and verifies the improvements due to the hBN dielectric.

5
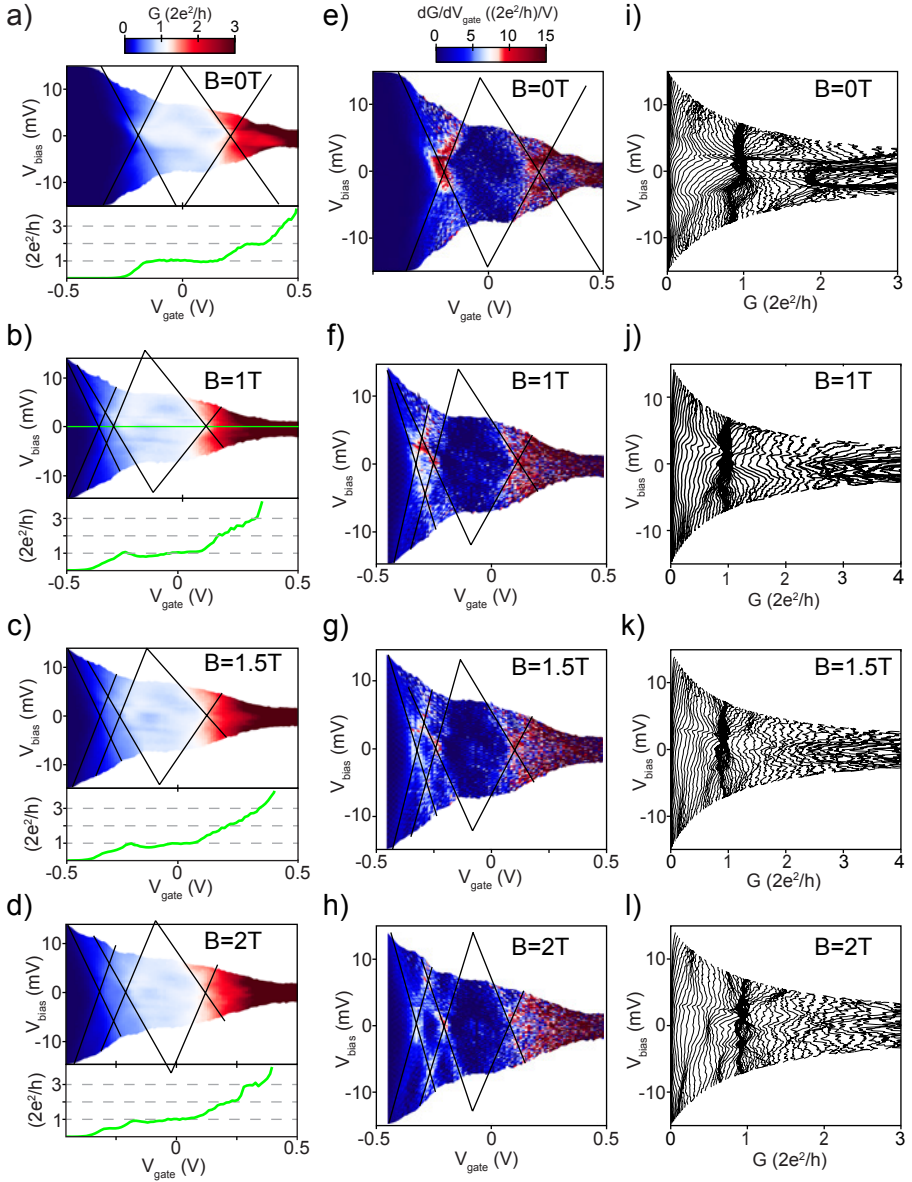
Figure 5.7: **a) – d)** Differential conductance G as function of V_{bias} and V_{gate} at increasing magnetic fields. **e) – h)** transconductance dG/dV_{gate} at increasing magnetic fields. **i) – l)** Line cuts from a)-d) at fixed V_{gate} drawn without offset between individual traces.
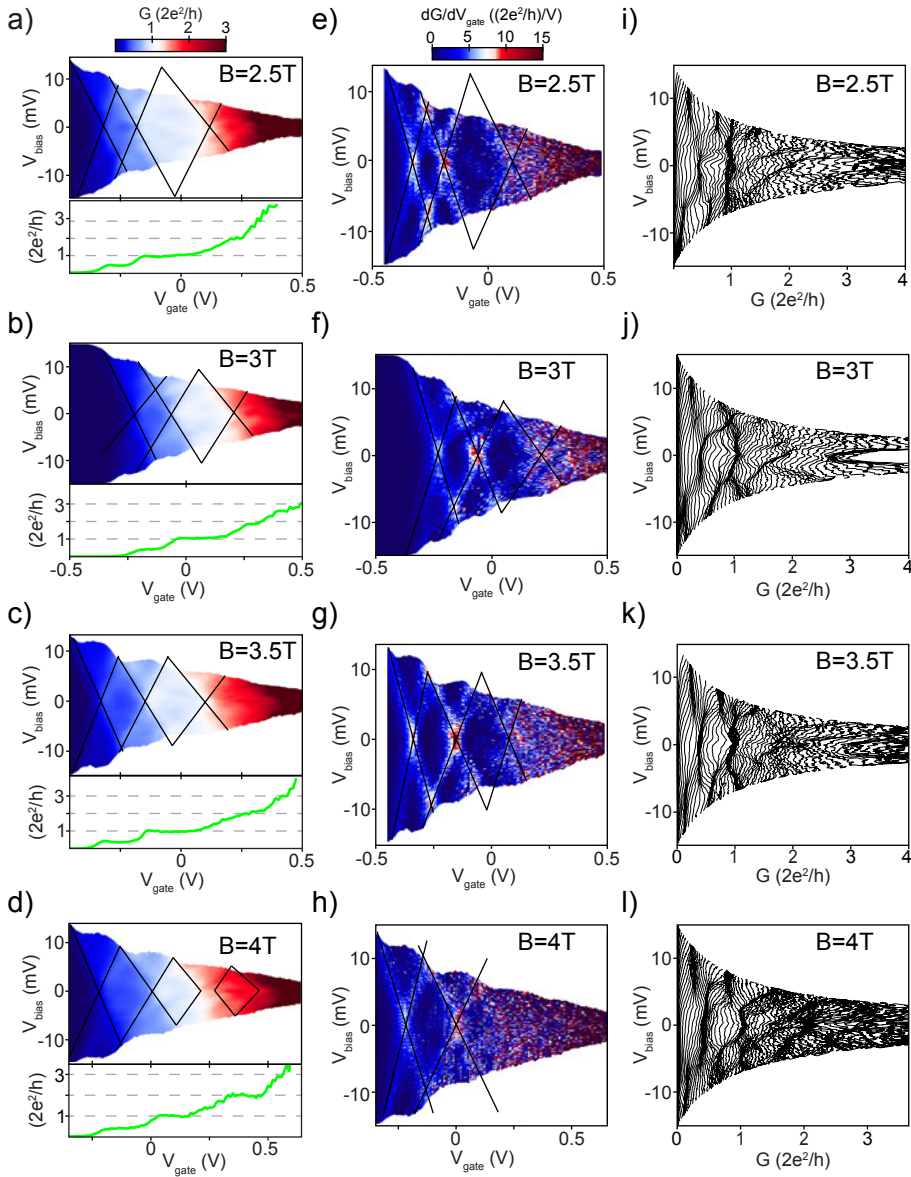
Figure 5.8: **a) – d)** Differential conductance G as function of V_{bias} and V_{gate} at increasing magnetic fields. **e) – h)** transconductance dG/dV_{gate} at increasing magnetic fields. **i) – l)** Line cuts from a)-d) at fixed V_{gate} drawn without offset between individual traces.
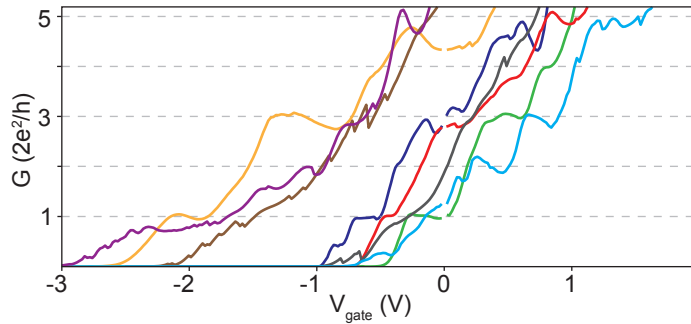
Figure 5.9: I-V traces of all eight devices fabricated with hBN dielectric.

5
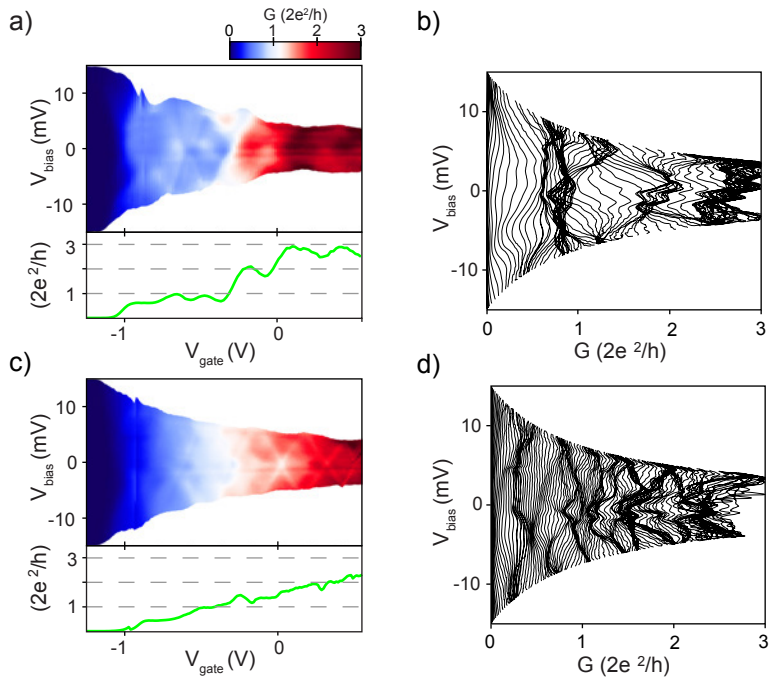
Figure 5.10: **a),b)** Differential conductance G of a second device on hBN and with fine gates at B = 0 T (a) and B = 4 T (b) **c),d)** Line-cuts from a),b) at fixed V_{gate} drawn without offset.
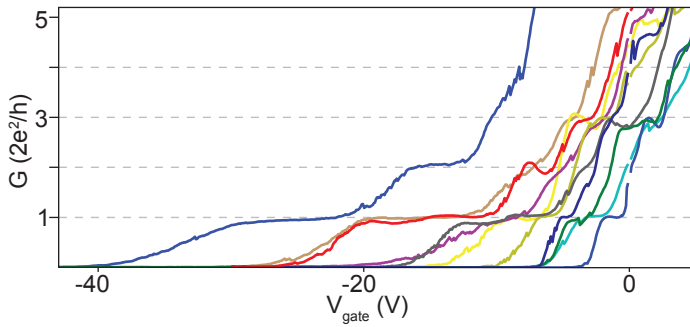
Figure 5.11: I-V traces of 11 different devices with wires on a SiO_2 dielectric taken at $V_{bias} = 10\,mV$
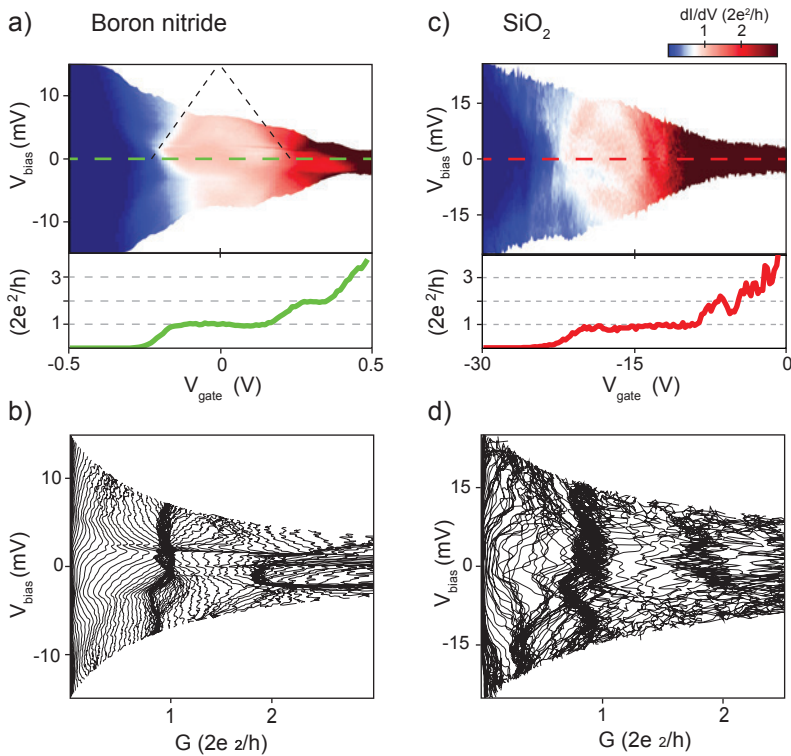
Figure 5.12: **a)** Color plot of the differential conductance G as function of V_{bias} and V_{gate} for a device with hBN dielectric at B = 0T. A line cut along $V_{bias} = 0\,mV$ is shown in the bottom panel. **b)** Line traces from a) at fixed V_{gate} drawn without offset between individual traces. **c)** Color plot of the differential conductance G as function of V_{bias} and V_{gate} of a device with a SiO_2 dielectric. **d)** Line traces of c) at fixed V_{gate}.

REFERENCES

[1] S. Nadj-Perge, S. M. Frolov, E. P. A. M. Bakkers, and L. P. Kouwenhoven, "Spin-orbit qubit in a semiconductor nanowire," *Nature*, vol. 468, no. 7327, pp. 1084–1087, 2010.

[2] J. W. G. Van den Berg, S. Nadj-Perge, V. S. Pribiag, S. R. Plissard, E. P. A. M. Bakkers, S. M. Frolov, and L. P. Kouwenhoven, "Fast spin-orbit qubit in an indium antimonide nanowire," *Phys. Rev. Lett.*, vol. 110, no. 6, p. 066806, 2013.

[3] K. D. Petersson, L. W. McFaul, M. D. Schroer, M. Jung, J. M. Taylor, A. A. Houck, and J. R. Petta, "Circuit quantum electrodynamics with a spin qubit," *Nature*, vol. 490, no. 7420, pp. 380–383, 2012.

[4] D. Liang and X. P. Gao, "Strong tuning of rashba spin–orbit interaction in single inas nanowires," *Nano Lett.*, vol. 12, no. 6, pp. 3263–3267, 2012.

[5] F. Rossella, A. Bertoni, D. Ercolani, M. Rontani, L. Sorba, F. Beltram, and S. Roddaro, "Nanoscale spin rectifiers controlled by the stark effect," *Nat. Nanotechnol.*, vol. 9, no. 12, pp. 997–1001, 2014.

[6] I. Žutić, J. Fabian, and S. Das Sarma, "Spintronics: Fundamentals and applications," *Rev. Mod. Phys.*, vol. 76, pp. 323–410, Apr 2004.

[7] L. Hofstetter, S. Csonka, J. Nygård, and C. Schönenberger, "Cooper pair splitter realized in a two-quantum-dot y-junction," *Nature*, vol. 461, no. 7266, pp. 960–963, 2009.

[8] A. Das, Y. Ronen, M. Heiblum, D. Mahalu, A. V. Kretinin, and H. Shtrikman, "High-efficiency cooper pair splitting demonstrated by two-particle conductance resonance and positive noise cross-correlation," *Nat. Commun.*, vol. 3, p. 1165, 2012.

[9] V. Mourik, K. Zuo, S. M. Frolov, S. R. Plissard, E. P. A. M. Bakkers, and L. P. Kouwenhoven, "Signatures of majorana fermions in hybrid superconductor-semiconductor nanowire devices," *Science*, vol. 336, no. 6084, pp. 1003–1007, 2012.

[10] M. T. Deng, C. L. Yu, G. Y. Huang, M. Larsson, P. Caroff, and H. Q. Xu, "Anomalous zero-bias conductance peak in a nb–insb nanowire–nb hybrid device," *Nano Lett.*, vol. 12, no. 12, pp. 6414–6419, 2012.

[11] H. O. H. Churchill, V. Fatemi, K. Grove-Rasmussen, M. T. Deng, P. Caroff, H. Q. Xu, and C. M. Marcus, "Superconductor-nanowire devices from tunneling to the multichannel regime: Zero-bias oscillations and magnetoconductance crossover," *Phys. Rev. B*, vol. 87, p. 241401, Jun 2013.

[12] M. Deng, C. Yu, G. Huang, M. Larsson, P. Caroff, and H. Xu, "Parity independence of the zero-bias conductance peak in a nanowire based topological superconductor-quantum dot hybrid device," *Sci. Rep.*, vol. 4, 2014.

5

[13] R. M. Lutchyn, T. D. Stanescu, and S. Das Sarma, "Search for majorana fermions in multiband semiconducting nanowires," *Phys. Rev. Lett.*, vol. 106, p. 127001, Mar 2011.

[14] B. J. van Wees, H. van Houten, C. W. J. Beenakker, J. G. Williamson, L. P. Kouwenhoven, D. van der Marel, and C. T. Foxon, "Quantized conductance of point contacts in a two-dimensional electron gas," *Phys. Rev. Lett.*, vol. 60, pp. 848–850, Feb 1988.

[15] D. A. Wharam, T. J. Thornton, R. Newbury, M. Pepper, H. Ahmed, J. E. F. Frost, D. G. Hasko, D. C. Peacock, D. A. Ritchie, and G. A. C. Jones, "One-dimensional transport and the quantisation of the ballistic resistance," *J. Phys. C,* vol. 21, no. 8, p. L209, 1988.

[16] H. T. Chou, S. Lüscher, D. Goldhaber-Gordon, M. J. Manfra, A. M. Sergent, K. W. West, and R. J. Molnar, "High-quality quantum point contacts in gan/algan heterostructures," *Appl. Phys. Lett.*, vol. 86, no. 7, 2005.

[17] D. Többen, D. A. Wharam, G. Abstreiter, J. P. Kotthaus, and F. Schaffler, "Ballistic electron transport through a quantum point contact defined in a si/si 0.7 ge 0.3 heterostructure," *Semicond. Sci. Technol.*, vol. 10, no. 5, p. 711, 1995.

[18] S. J. Koester, B. Brar, C. R. Bolognesi, E. J. Caine, A. Patlach, E. L. Hu, H. Kroemer, and M. J. Rooks, "Length dependence of quantized conductance in ballistic constrictions fabricated on inas/alsb quantum wells," *Phys. Rev. B*, vol. 53, pp. 13063–13073, May 1996.

[19] I. van Weperen, S. R. Plissard, E. P. A. M. Bakkers, S. M. Frolov, and L. P. Kouwenhoven, "Quantized conductance in an insb nanowire," *Nano Lett.*, vol. 13, no. 2, pp. 387–391, 2012.

[20] Ö. Gül, D. J. van Woerkom, I. van Weperen, D. Car, S. R. Plissard, E. P. A. M. Bakkers, and L. P. Kouwenhoven, "Towards high mobility insb nanowire devices," *Nanotechnology*, vol. 26, no. 21, p. 215202, 2015.

[21] C. Dean, A. Young, I. Meric, C. Lee, L. Wang, S. Sorgenfrei, K. Watanabe, T. Taniguchi, P. Kim, K. Shepard, and J. Hone, "Boron nitride substrates for high-quality graphene electronics," *Nat. Nanotechnol.*, vol. 5, no. 10, pp. 722–726, 2010.

[22] A. Castellanos-Gomez, M. Buscema, R. Molenaar, V. Singh, L. Janssen, H. S. J. van der Zant, and G. A. Steele, "Deterministic transfer of two-dimensional materials by all-dry viscoelastic stamping," *2D Mater.*, vol. 1, no. 1, p. 011002, 2014.

[23] S. R. Plissard, D. R. Slapak, M. A. Verheijen, M. Hocevar, G. W. G. Immink, I. van Weperen, S. Nadj-Perge, S. M. Frolov, L. P. Kouwenhoven, and E. P. A. M. Bakkers, "From insb nanowires to nanocubes: Looking for the sweet spot," *Nano Lett.*, vol. 12, no. 4, pp. 1794–1798, 2012.

[24] D. Car, J. Wang, M. A. Verheijen, E. P. A. M. Bakkers, and S. R. Plissard, "Rationally designed single-crystalline nanowire networks," *Adv. Mater.*, vol. 26, no. 28, pp. 4875–4879, 2014.

5

[25] K. Flöhr, M. Liebmann, K. Sladek, H. Y. Günel, R. Frielinghaus, F. Haas, C. Meyer, H. Hardtdegen, T. Schäpers, D. Grützmacher, and M. Morgenstern, "Manipulating inas nanowires with submicrometer precision," *Rev. Sci. Instrum.*, vol. 82, no. 11, p. 113705, 2011.

[26] D. B. Suyatin, C. Thelander, M. T. Björk, I. Maximov, and L. Samuelson, "Sulfur passivation for ohmic contact formation to inas nanowires," *Nanotechnology*, vol. 18, no. 10, p. 105307, 2007.

[27] A. Ford, S. B. Kumar, R. Kapadia, J. Guo, and A. Javey, "Observation of degenerate one-dimensional sub-bands in cylindrical inas nanowires," *Nano Lett.*, 2012.

[28] I. van Weperen. PhD thesis, TU Delft, 10 2014.

[29] J. M. Krans, J. M. Van Ruitenbeek, V. V. Fisun, I. K. Yanson, and L. J. De Jongh, "The signature of conductance quantization in metallic point contacts," *Nature*, vol. 375, no. 6534, pp. 767–769, 1995.

[30] L. P. Kouwenhoven, B. J. van Wees, C. J. P. M. Harmans, J. G. Williamson, H. van Houten, C. W. J. Beenakker, C. T. Foxon, and J. J. Harris, "Nonlinear conductance of quantum point contacts," *Phys. Rev. B*, vol. 39, pp. 8040–8043, Apr 1989.

[31] M. Scheffler, S. Nadj-Perge, L. P. Kouwenhoven, M. T. Borgström, and E. P. A. M. Bakkers, "Diameter-dependent conductance of inas nanowires," *J. Appl. Phys.*, vol. 106, no. 12, 2009.

[32] E. Halpern, G. Elias, A. V. Kretinin, H. Shtrikman, and Y. Rosenwaks, "Direct measurement of surface states density and energy distribution in individual inas nanowires," *Appl. Phys. Lett.*, vol. 100, no. 26, 2012.

[33] G. W. Holloway, D. Shiri, C. M. Haapamaki, K. Willick, G. Watson, R. R. LaPierre, and J. Baugh, "Magnetoconductance signatures of subband structure in semiconductor nanowires," *Phys. Rev. B*, vol. 91, p. 045422, Jan 2015.

[34] Y. Tserkovnyak and B. I. Halperin, "Magnetoconductance oscillations in quasiballistic multimode nanowires," *Phys. Rev. B*, vol. 74, p. 245327, Dec 2006.

[35] P. D. C. King, T. D. Veal, M. J. Lowe, and C. F. McConville, "Surface electronic properties of clean and s-terminated insb(001) and (111)b," *J. Appl. Phys.*, vol. 104, no. 8, 2008.

[36] A. Vuik, D. Eeltink, A. Akhmerov, and M. Wimmer, "Effects of the electrostatic environment on the majorana nanowire devices," *New Journal of Physics*, vol. 18, no. 3, p. 033013, 2016.

[37] B. Nijholt and A. R. Akhmerov, "Orbital effect of magnetic field on the majorana phase diagram," *arXiv:1509.02675*, 2015.

[38] P. Středa and P. Šeba, "Antisymmetric spin filtering in one-dimensional electron systems with uniform spin-orbit coupling," *Phys. Rev. Lett.*, vol. 90, p. 256601, Jun 2003.

[39] Y. V. Pershin, J. A. Nesteroff, and V. Privman, "Effect of spin-orbit interaction and in-plane magnetic field on the conductance of a quasi-one-dimensional system," *Phys. Rev. B*, vol. 69, p. 121306, Mar 2004.

[40] K. J. Thomas, J. T. Nicholls, M. Y. Simmons, M. Pepper, D. R. Mace, and D. A. Ritchie, "Possible spin polarization in a one-dimensional electron gas," *Phys. Rev. Lett.*, vol. 77, pp. 135–138, Jul 1996.

[41] F. Bauer, J. Heyder, E. Schubert, D. Borowsky, D. Taubert, B. Bruognolo, D. Schuh, W. Wegscheider, J. von Delft, and S. Ludwig, "Microscopic origin of the 0.7-anomaly in quantum point contacts," *Nature*, vol. 501, no. 7465, pp. 73–78, 2013.

[42] M. J. Iqbal, R. Levy, E. J. Koop, J. B. Dekker, J. P. De Jong, J. H. M. van der Velde, D. Reuter, A. D. Wieck, R. Aguado, Y. Meir, and C. H. van der Wal, "Odd and even kondo effects from emergent localization in quantum point contacts," *Nature*, vol. 501, no. 7465, pp. 79–83, 2013.

[43] O. Goulko, F. Bauer, J. Heyder, and J. von Delft, "Effect of spin-orbit interactions on the 0.7 anomaly in quantum point contacts," *Phys. Rev. Lett.*, vol. 113, p. 266402, Dec 2014.

[44] C. W. Groth, M. Wimmer, A. R. Akhmerov, and X. Waintal, "Kwant: a software package for quantum transport," *New J. Phys.*, vol. 16, no. 6, p. 063065, 2014.

5

6

CONDUCTANCE THROUGH A HELICAL GAP IN AN INSB NANOWIRE

J. Kammhuber, M. C. Cassidy, F. Pei, M. P. Nowak, A. Vuik, Ö. Gül, D. Car, S. R. Plissard, E. P. A. M Bakkers, M. Wimmer, and L. P. Kouwenhoven

The motion of an electron and its spin are generally not coupled. However in a one dimensional (1D) material with strong spin-orbit interaction (SOI) a helical state may emerge at finite magnetic fields [1, 2], where electrons of opposite spin will have opposite momentum. The existence of this helical state has applications for spin filtering and Cooper pair splitter devices [3, 4] and is an essential ingredient for realizing topologically protected quantum computing using Majorana zero modes [5–7]. Here we report electrical conductance measurements of a quantum point contact (QPC) formed in an indium antimonide (InSb) nanowire as a function of magnetic field. At magnetic fields exceeding $3\,\mathrm{T}$, the $2e^2/h$ plateau shows a reentrant conductance feature towards $1e^2/h$ which increases linearly in width with magnetic field before enveloping the $1e^2/h$ plateau. Rotating the external magnetic field either parallel or perpendicular to the spin-orbit field allows us to clearly attribute this experimental signature to SOI. We compare our observations with a model of a QPC incorporating SOI and extract a spin-orbit energy of ~ $6.5\,\mathrm{meV}$, which is significantly stronger than the SO energy obtained by other methods.

6.1. INTRODUCTION

Spin-orbit interaction is a relativistic effect where a charged particle moving in an electric field E with momentum k and velocity $v = k/m_0$, experiences an effective magnetic field $B_{SO} = (-1/m_0 c)k \times E$ in its rest frame. The magnetic moment of the electron spin, $\mu = eS/m_0$, interacts with this effective magnetic field, resulting in a spin-orbit Hamiltonian $H_{SO} = -\mu.B_{SO}$ that couples the spin to the orbital motion and electric field. In crystalline materials, the electric field arises from a symmetry breaking that is either intrinsic to the underlying crystal lattice in which the carriers move, known as the Dresselhaus SOI [8], or an artificially induced asymmetry in the confinement potential due to an applied electric field, or Rashba SOI [9]. Wurtzite and certain zincblende nanowires possess a finite Dresselhaus SOI, and so the SOI is a combination of both the Rashba and Dresselhaus components. For zincblende nanowires grown along the [111] growth direction the crystal lattice is inversion symmetric, and so only a Rashba component to the spin-orbit interaction is thought to remain [10].

Helical states have been shown to emerge in the edge mode of 2D quantum spin hall topological insulators [11, 12], and in quantum wires created in GaAs cleaved edge overgrowth samples [13]. They have also been predicted to exist in carbon nanotubes under a strong applied electric field [14], RKKY systems [15], and in InAs and InSb semiconducting nanowires where they are essential for the formation of Majorana zero modes. Although the signatures of Majoranas have been observed in nanowire-superconductor hybrid devices [16, 17], explicit demonstration of the helical state in these nanowires has remained elusive. The measurement is expected to show a distinct experimental signature of the helical state - a return to $1e^2/h$ conductance at the $2e^2/h$ plateau in increasing magnetic field as different portions of the band dispersion are probed [1, 2, 18]. While ballistic transport through nanowire QPCs is now standard [19, 20], numerical simulations have shown that the visibility of this experimental signature critically depends on the exact combination of geometrical and physical device parameters [18].

Here we observe a clear signature of transport through a helical state in a QPC formed in an InSb nanowire when the magnetic field has a component perpendicular to the spin-orbit field. We show that the state evolves under rotation of the external magnetic field, disappearing when the magnetic field is aligned with B_{SO}. By comparing our data to a theoretical model, we extract a spin-orbit energy $E_{SO} = 6.5$ meV, significantly stronger than that measured in InSb nanowires by other techniques.

6.2. DEVICE LAYOUT

Figure 6.1a) shows a schematic image of a typical QPC device. An InSb nanowire is deposited on a degenerately doped silicon wafer covered with a thin (20 nm) SiN dielectric. The QPC is formed in the nanowire channel in a region defined by the source and drain contacts spaced ~ 325 nm apart. The chemical potential μ in the QPC channel, which sets the subband occupation, is controlled by applying a voltage to the gate V_g. The electric field in the nanowire, E, generated by the backgate and the substrate that the nanowire lies on, both induce a structural inversion asymmetry that results in a finite Rashba spin-orbit field. As the wire is translationally invariant along its length, the spin-orbit field, B_{SO}, is perpendicular to both the electric field and the wire axis. The effective
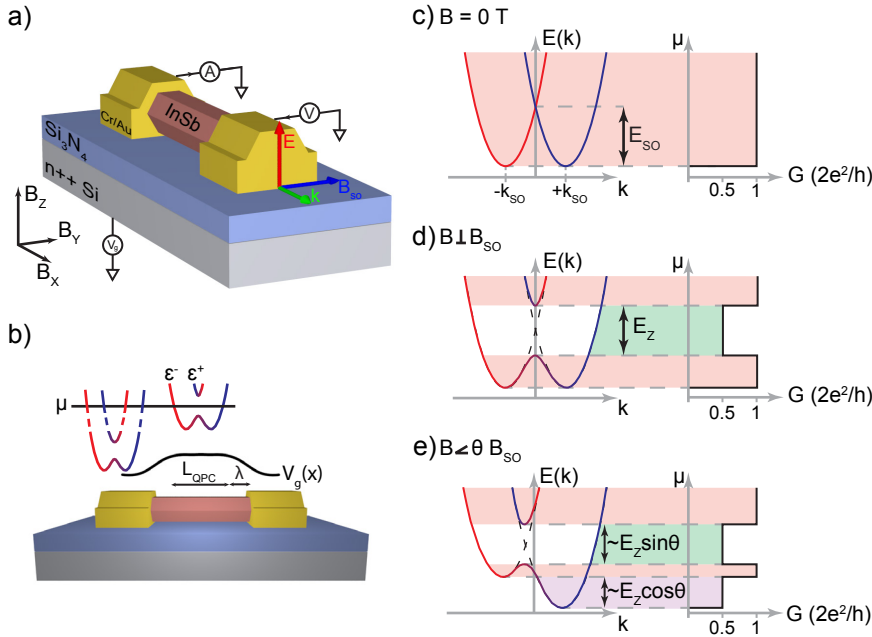
Figure 6.1: The helical gap in a 1D nanowire device. **a)** An InSb nanowire device with a Rashba spin-orbit field B_{SO} perpendicular to the wave vector **k** and the electric field **E**. A voltage is sourced to one contact, and the resulting conductance measured from the second contact. The chemical potential in the wire, μ, is tuned with a global backgate V_g. **b)** The QPC channel of length L is defined by the two contacts. Underneath the nanowire contacts, many subbands are occupied as the contacts screen the gate electric field. In the nanowire channel away from the contacts, the chemical potential in the wire, μ, is tuned with V_g. The onset shape of V_g with a lengthscale λ is set by the dielectric and screening of the electric field from the metallic contacts resulting in an effective QPC length $L_{QPC} = L - 2\lambda$. **c)** The energy dispersion of the first two subbands for a system with SOI at external magnetic field $B = 0$. The SOI causes subbands to shift by k_{SO} in momentum space, as electrons with opposite spins carry opposite momentum. When the electrochemical potential μ in the wire is tuned conductance plateaus will occur at integer values of G_0. **d)** At finite magnetic field B perpendicular to B_{SO}, the spin polarized bands hybridize opening a helical gap of size E_Z (green). In this region the conductance reduces from $1 \cdot G_0$ to $0.5 \cdot G_0$ when μ is positioned inside the gap. **e)** When the magnetic field is orientated at an angle θ to B_{SO}, the size of the helical gap decreases to only include the component of the magnetic field perpendicular to B_{SO}. For all angles the reentrant conductance feature at $0.5 \cdot G_0$ in the $1 \cdot G_0$ plateau will scale linearly with Zeeman energy.

6
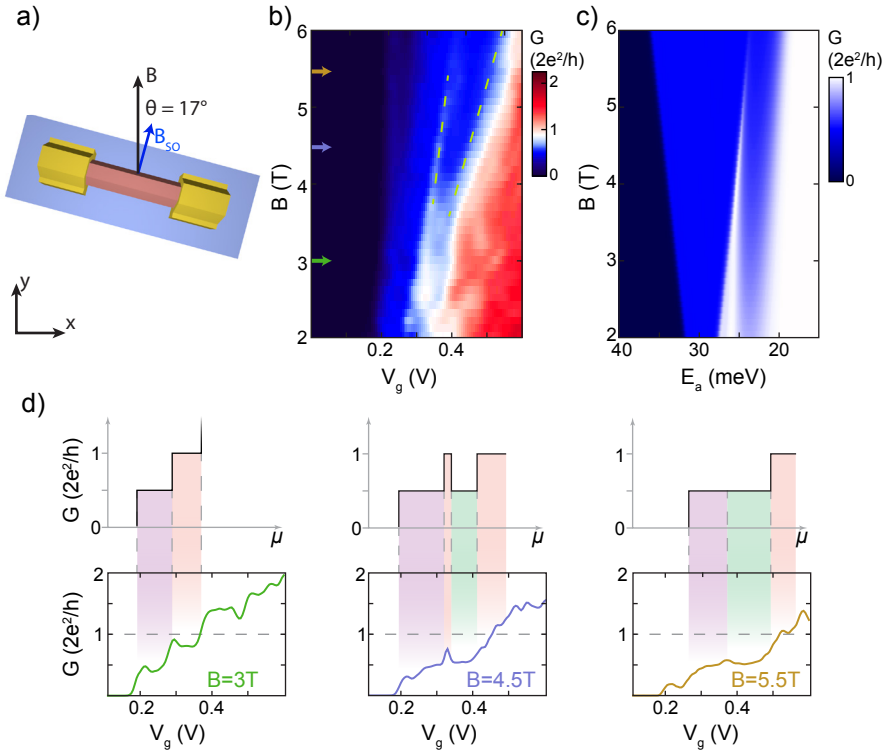
Figure 6.2: Magnetic field dependence of the helical gap. **a)** The nanowire lies in the x-y plane at an angle $\theta = 17°$ relative to the external magnetic field. **b)** Differential conductance dI/dV at zero source-drain bias as a function of back gate voltage and external magnetic field. At low magnetic fields conductance plateaus at multiples of $0.5 \cdot G_0$ are visible. Above $B = 3\,T$, a reentrant conductance feature at $0.5 \cdot G_0$ appears in the $1 \cdot G_0$ plateau. The feature evolves linearly with Zeeman energy indicated by dashed green lines. **c)** Numerical simulations of the differential conductance as a function of the potential E_a and external magnetic field for $L = 325\,nm$, $\theta = 17°$ and $l_{SO} = 20\,nm$ (See Supplementary Information for a more detailed description of the model). In the numerical simulations, the conductance plateaus have a different slope compared to the experimental data as the calculations neglect screening by charges in the wire. **d)** Line traces of the conductance map in b). As the helical gap is independent of disorder or interference effects, these and other anomalous conductance features average out in a 2D colorplot improving the visibility of the helical gap in b) compared to the individual traces in d).
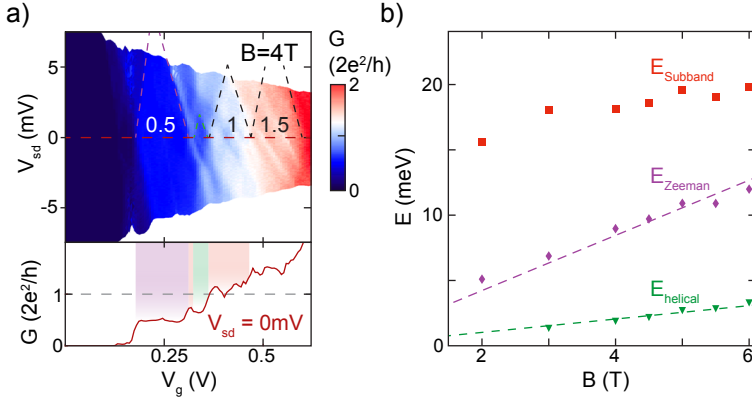
Figure 6.3: Voltage bias spectroscopy of the helical gap. **a)** Conductance measurement as a function of QPC gate and source-drain bias voltage at $B = 4\,\text{T}$. The observed helical gap (green) is a stable feature in voltage bias. Dotted lines are drawn as guide to the eye indicating the plateau edges. **b)** Evolution of the energy levels extracted from scans similar to a) at increasing magnetic field. Fits with intercept fixed at zero (dotted lines) give the g-factor of the first subband and the offset angle via $g = 1/(\mu_B \cos\theta) \cdot dE/dB$ and $E_{helical}/E_{Zeeman} \approx \tan\theta$. We find $g = 38 \pm 1$ and $\theta = 13° \pm 2°$. Individual scans are included in the Supplementary Information.

channel length, $L_{QPC} \sim 245\,\text{nm}$, as well as the shape of the onset potential $\lambda \sim 80\,\text{nm}$ are set by electrostatics which are influenced by both the thickness of the dielectric and the amount of electric field screening provided by the metallic contacts to the nanowire (Fig. 6.1b). Here we report measurements from one device. Data from an additional device that shows the same effect, as well as control devices of different channel lengths and onset potentials, is provided in the Supplementary Information.

The energy-momentum diagrams in Fig. 6.1c)–e) show the dispersion from the 1D nanowire model of Refs. 1 and 2 including both SOI with strength α and Zeeman splitting $E_Z = g\mu_B B$, where g is the g-factor, μ_B the Bohr magneton and B the magnetic field strength. These dispersion relations explain how the helical gap can be detected: Without magnetic field, the SOI causes the first two spin degenerate subbands to be shifted laterally in momentum space by $\pm k_{SO} = m^* \alpha/\hbar^2$ with m^* the effective electron mass, as electrons with opposite spins carry opposite momentum, as shown in Fig. 6.1c). The corresponding spin-orbit energy is given by $E_{SO} = \hbar^2 k_{SO}^2/2m^*$. However, here Kramers degeneracy is preserved and hence the plateaus in conductance occur at integer values of $G_0 = 2e^2/h$, as for a system without SOI. Applying a magnetic field perpendicular to B_{SO} the spin bands hybridize and a helical gap, of size E_Z opens, as shown in Fig. 6.1d). When the chemical potential µ is tuned by the external gate voltage, it first aligns with the bottom of both bands resulting in conductance at $1 \cdot G_0$ before reducing from $1 \cdot G_0$ to $0.5 \cdot G_0$ when µ is positioned inside the gap. This conductance reduction with a width scaling linearly with increasing Zeeman energy, is a hallmark of transport through a helical state. When the magnetic field is oriented at an angle θ to B_{SO}, the size of the helical gap decreases as it is governed by the component of the magnetic field perpendicular to B_{SO}, as shown in Fig. 6.1e). Additionally, the two subband bottoms also experience a spin splitting giving rise to an additional Zeeman gap. For a general angle

θ, the QPC conductance first rises from 0 to $0.5 \cdot G_0$, then to $1 \cdot G_0$, before dropping to $0.5 \cdot G_0$ again. The helical gap thus takes the form of a re-entrant $0.5 \cdot G_0$ conductance feature. By comparing to a 1D nanowire model, we can extract both the size of the helical gap $E_{helical} \approx E_Z \sin\theta$ and the Zeeman shift $E_{Zeeman} \approx E_Z \cos\theta$ (see Supplementary Information). This angle dependency is a unique feature of SOI and can be used as a decisive test for its presence in the experimental data.

6.3. LINEAR MAGNETIC FIELD

Figure 6.2 shows the differential conductance dI/dV of our device at zero source-drain bias as a function of gate and magnetic field. Here the magnetic field B is offset at a small angle $\theta = 17°$ from B_{SO} in the x-y plane (see Fig. 6.2a). We determine that our device has this orientation from the angle-dependence of the magnetic field, by clearly resolving the $1 \cdot G_0$ plateau before the re-entrant conductance feature, which is reduced at larger angles (see Supplementary Information). For low magnetic fields, we observe conductance plateaus quantized in steps of $0.5 \cdot G_0$, as typical for a QPC in a spin polarizing B-field with or without SOI. Above $B = 3\,\text{T}$, the $1 \cdot G_0$ plateau shows a conductance dip to $0.5 \cdot G_0$. This reentrant conductance feature evolves continuously as a function of magnetic field, before fully enveloping the $1 \cdot G_0$ plateau for magnetic fields larger than around 5.5 T. Line traces corresponding to the colored arrows in Fig. 6.2b) are shown in Fig. 6.2d). The feature is robust at higher temperatures up to 1K, as well across multiple thermal cycles (see Supplementary Information). Using the 1D nanowire model with $\theta = 17°$ we find that the helical gap feature vanishes into a continuous $0.5 \cdot G_0$ plateau when $E_Z > 2.4 E_{SO}$. Using the extracted g-factor $g = 38$ of our device (see Fig. 6.3 and Supplementary Information) we find a lower bound for the spin-orbit energy $E_{SO} = 5.5\,\text{meV}$, corresponding to a spin-orbit length $l_{SO} = 1/k_{SO} \approx 22\,\text{nm}$. For a second device, we extract a similar value $E_{SO} = 5.2\,\text{meV}$. Recently it has been highlighted that the visibility of the helical gap feature depends crucially on the shape of the QPC potential [18]. To verify that our observation is compatible with SOI in this respect, we perform self-consistent simulations of the Poisson equation in Thomas-Fermi approximation for our device geometry. The resulting electrostatic potential is then mapped to an effective 1D QPC potential for a quantum transport simulation using parameters for InSb (for details, see Supplementary Information). These numerical simulations, shown in Fig. 6.2c), fit best for $l_{SO} = 20\,\text{nm}$ ($E_{SO} = 6.5\,\text{meV}$) and agree well with the experimental observation, corroborating our interpretation of the re-entrant conductance feature as the helical gap.

Voltage bias spectroscopy, as shown in Fig. 6.3a) confirms that this state evolves as a constant energy feature. By analyzing the voltage bias spectroscopy data at a range of magnetic fields, we directly convert the development of the initial $0.5 \cdot G_0$ plateau, as well as the reentrant conductance feature to energy (Fig. 6.3b). From the evolution of the width of the first $0.5 \cdot G_0$ plateau, we can calculate the g-factor of the first subband $g = 38 \pm 1$. This number is consistent with the recent experiments, which reported g factors of $35 - 50$ [21, 22]. Comparing the slopes of the Zeeman gap and the helical gap $E_h/E_Z \approx \tan\theta$ provides an alternative way to determine the offset angle θ. We find $\theta = 13° \pm 2°$ which is in reasonable agreement with the angle determined by magnetic field rotation.
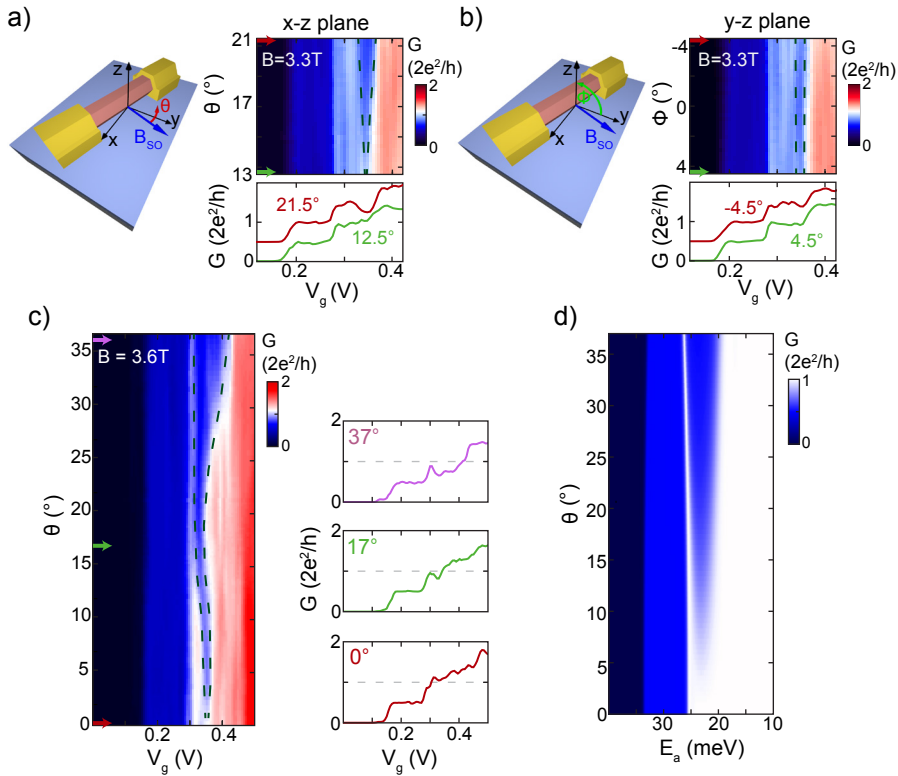
Figure 6.4: Angle dependence of the helical gap. **a)** Rotation of the magnetic field at $B = 3.3\,\text{T}$ in the x-y plane parallel to the substrate shows strong angle dependence of the helical gap. The conductance dip closes when B is rotated towards B_{SO} and opens when B is rotated away from B_{SO}. **b)** Rotation of the magnetic field at $B = 3.3\,\text{T}$ in the y-z plane, mostly perpendicular to B_{SO}. While the angle range is identical to a) there is little change in the conductance dip. **c)** Rotation of the magnetic field at $B = 3.6\,\text{T}$ in the x-y plane over a large angle range. The conductance dip disappears when B is parallel to B_{SO} which gives the exact offset angle between B_{SO} and B_Z, $\theta = 17°$. **d)** Numerical simulations of the differential conductance in a magnetic field rotated along θ in the x-y plane with $L = 325\,\text{nm}$ and $l_{SO} = 20\,\text{nm}$.

6.4. Rotating Magnetic Field

To confirm that the reentrant conductance feature agrees with spin-orbit theory, we rotate the magnetic field in the plane of the substrate at a constant magnitude $B = 3.3$ T, as shown in Fig. 6.4a). When the field is rotated towards being parallel to B_{SO}, the conductance dip closes, while when it is rotated away from B_{SO}, the dip increases in width and depth. In contrast, when the magnetic field is rotated the same amount around the y-z plane, which is largely perpendicular to B_{SO}, there is little change in the reentrant conductance feature, as shown in Fig. 6.4b). Figure 6.4c) shows the result of rotating through a larger angle in the x-y plane shows this feature clearly evolves with what is expected for spin-orbit. Our numerical simulations in Figure 6.4d) agree well with the observed experimental data. The small difference in the angle evolution between the numerical simulations and experimental data can be attributed to imperfect alignment of the substrate with the x-y plane.

6.5. Conclusions

The extracted SO energy of 6.5 meV is significantly larger than that obtained via other techniques, such as weak anti localization (WAL) measurements [23], and quantum dot spectroscopy [22]. This is not entirely unexpected, due to the differing geometry for this device and different conductance regime it is operated in. Quantum dot measurements require strong confinement, and so the Rashba SOI is modified by the local electrostatic gates used to define the quantum dot. Weak anti-localization measurements are performed in an open conductance regime, however they assume transport through a diffusive, rather than a ballistic channel. Neither of these measurements explicitly probe the spin-orbit interaction where exactly one mode is transmitting in the nanowire, the ideal regime for Majoranas, and so the spin-orbit parameters extracted from QPC measurements offer a more accurate measurement of the SOI experienced by the Majorana zero mode. Also, the SOI in a nanowire can be different for every subband, and it is expected that the lowest mode has the strongest spin-orbit due to a smaller confinement energy [10]. Additionally, the finite diameter of the nanowire, together with impurities within the InSb crystal lattice [24] both break the internal symmetry of the crystal lattice and may contribute a non-zero Dresselhaus component to the spin-orbit energy that has not been previously considered. While high quality quantized conductance measurements have been previously achieved in short channel devices [19] ($L \sim 150$ nm), the channel lengths required for observing the helical gap are at the experimental limit of observable conductance quantization. As shown in the Supplementary Information, small changes in the QPC channel length, spin-orbit strength or the QPC potential profile are enough to obscure the helical gap, particularly for wires with weaker SOI. We have fabricated and measured a range of QPCs with different length and potential profiles, and only two devices of $L \sim 300$ nm showed unambiguous signatures of a helical gap. Possibly some of the other devices did not show clear signatures because they had weaker SOI.

Several phenomena have been reported to result in anomalous conductance features in a device such as this. Oscillations in conductance due to Fabry-Perot resonances are a common feature in clean QPCs. Typically the first oscillation at the front of each plateau is the strongest and the oscillations monotonically decrease in strength further along

each plateau [18, 25]. In our second device, we clearly observe Fabry-Perot conductance oscillations at the beginning of each plateau, however these oscillations are significantly weaker than the subsequent conductance dip. Furthermore we observe Fabry-Perot oscillations at each conductance plateau, while the reentrant conductance feature is only present at the $1 \cdot G_0$ plateau. Additionally, the width of the Fabry-Perot oscillations does not change with increasing magnetic field, unlike the observed re-entrant conductance feature. A local quantum dot in the Coulomb or Kondo regimes can lead to conductance suppression, which increases in magnetic field [26]. However both effects should be stronger in the lower conductance region, and exists at zero magnetic field, unlike the feature in our data. Additionally, a Kondo resonance should scale with $V_{sd} = \pm g\mu_B B/e$ as a function of external magnetic field, decreasing instead of increasing the width of the region of suppressed conductance. Given the g factor measured in InSb quantum dots, and its variation with the angle of applied magnetic field $g = 35 - 50$ [22], we can exclude both these effects. Similarly the Fano effect and disorder can also induce a conductance dip, but these effects should not increase linearly with magnetic field. The 0.7 anomaly occurs at the beginning of the plateau, and numerical studies have shown it does not drastically affect the observation of the helical gap [27]. In conclusion, we have observed a return to $1e^2/h$ conductance at the $2e^2/h$ plateau in a QPC in an InSb nanowire. The continuous evolution in increasing magnetic field and the strong angle dependence in magnetic field rotations agree with a SOI related origin of this feature and distinguish it from Fabry-Perot oscillations and other g-factor related phenomena. Additional confirmation is given by numerical simulations of an emerging helical gap in InSb nanowires. The extracted spin-orbit energy of 6.5 meV is significantly larger than what has been found by other techniques, and more accurately represents the true spin-orbit energy in the first conduction mode. Such a large spin-orbit energy reduces the requirements on nanowire disorder for reaching the topological regime [28], and offers promise for using InSb nanowires for the creation of topologically protected quantum computing devices.

6.6. METHODS

DEVICE FABRICATION

The InSb nanowires were grown using the metalorganic vapor phase epitaxy (MOVPE) process and are grown along the [111] growth direction in a zinc-blende crystal structure [29]. The InSb nanowires were deposited using a deterministic deposition method on a degenerately doped silicon wafer. The wafer covered with 20 nm of low stress LPCVD SiN which is used as a high quality dielectric. Electrical contacts (Cr/Au, 10 nm/110 nm) defined using ebeam lithography were then evaporated at the ends of the wire. Before evaporation the wire was exposed to an ammonium polysulfide surface treatment and short helium ion etch to remove the surface oxide and to dope the nanowire underneath the contacts [19].

MEASUREMENTS

Measurements are performed in a dilution refrigerator with base temperature $\sim 20\,\text{mK}$ fitted with a 3-axis vector magnet, which allowed for the external magnetic field to be

rotated in-situ. The sample is mounted with the substrate in the x-y plane with the wire orientated at a small offset angle $\theta = 17°$ from the x-axis. We measure the differential conductance $G = dI/dV$ using standard lock-in techniques with an excitation voltage of $60\,\mu V$ and frequency $f = 83\,Hz$. Additional resistances due to filtering are subtracted to give the true conductance through the device. The helical gap, Zeeman gap, and subband spacing reported in Fig. 6.3b) were extracted from analysis of the full voltage bias conductance diamonds shown in Fig. 6.3a) and Fig. 6.10. The subband spacing was extracted by summing the widths of the 0.5 and 1 plateaus, the helical gap and Zeeman gap from their respective conductance diamonds.

NUMERICAL TRANSPORT SIMULATIONS

We use the method of finite differences to discretize the one-dimensional nanowire model of Ref 2. In order to obtain a one-dimensional QPC potential, we solve the Poisson equation self-consistently for the full three-dimensional device structure treating the charge density in the nanowire in Thomas-Fermi approximation. To this end, we use a finite element method, using the software FEniCS [30]. The resulting three-dimensional potential is then projected onto the lowest nanowire subband and interpolated using the QPC potential model of Ref [18]. Transport in the resulting tight-binding model is calculated using the software Kwant [31].

6.7. SUPPLEMENTARY MATERIALS

6.7.1. NUMERICAL SIMULATIONS OF THE CONDUCTANCE THROUGH A HELICAL STATE

POISSON CALCULATIONS IN A 3D NANOWIRE DEVICE

Observing the helical gap in a semiconducting nanowire crucially depends on the smoothness of the electrostatic potential profile between the two contacts [18]. When the potential profile changes too abruptly, it forms a tunnel barrier which suppresses conductance well below quantized values, thereby masking features of the helical gap. On the other hand, if the potential varies on a length scale much larger than the characteristic spin-orbit coupling length l_{SO}, transmission through the 'internal state' (the smaller-momentum state of the two right-moving states in the bottom of the lower band) is suppressed. This reduces the first $2e^2/h$ plateau in the conductance to a $1e^2/h$ plateau, thereby concealing again the helical gap.

Because of the crucial role of the electrostatic potential, we perform realistic Poisson calculations to compute the potential $\phi(\vec{r})$ in the nanowire (with $\vec{r} = (x, y, z)$), solving the Poisson equation of the general form

$$\nabla^2 \phi(\vec{r}) = -\frac{\rho(\vec{r})}{\epsilon}, \tag{6.1}$$

with ϵ the dielectric permittivity and ρ the charge density. For the charge density ρ, we apply the Thomas-Fermi approximation [32]

$$\rho(\vec{r}) = \frac{e}{3\pi^2 \epsilon} \left(\frac{2m^* e\phi(\vec{r})}{\hbar^2} \right)^{3/2}, \tag{6.2}$$

where m^* is the effective mass of InSb.

For a given charge density ρ, we solve Eq. 6.1 numerically for the potential using the finite element package FEniCS [30]. We model the two normal contacts as metals with a fixed potential $V_N = 0.22$ V, assuming a small work function difference between the nanowire and the normal contacts. The back gate is modeled as a fixed potential V_G along the bottom surface of the dielectric layer. We use the dielectric permittivities for InSb and SiN in the wire and the dielectric layer respectively. The FEM mesh, with its dimensions and boundary conditions, is depicted in Fig. 6.5a).

We apply the Anderson mixing scheme [33] to solve the nonlinear equation formed by Eqs. 6.1 and 6.2 self-consistently. An example of a self-consistent Poisson potential with Thomas-Fermi density is plotted in Fig. 6.5b).

CONDUCTANCE CALCULATIONS IN A 1D MODEL WITH A PROJECTED POTENTIAL BARRIER

To apply the 3D Poisson potential in a simple 1D nanowire model, we convert the three-dimensional potential $\phi(x, y, z)$ to a one-dimensional effective potential barrier $\hat{\phi}(x)$ by projecting ϕ on the transverse wave functions $\psi(y, z)$ in the nanowire:

$$\hat{\phi}(x) = \langle \psi(y, z) | \phi(x, y, z) | \psi(y, z) \rangle. \tag{6.3}$$

To do this, we compute the eigenenergies of the Hamiltonian of a two-dimensional cross section at a point x_0 along the wire, with a corresponding potential $\phi(x_0, y, z)$. The effective potential barrier is then given by the ground state of the Hamiltonian. The longitudinal variation of the potential barrier is obtained by computing the ground state of the transverse Hamiltonian at many points along the wire. An example of the projected potential is given in Fig. 6.5c) with the solid-black curve.

Due to rough boundary conditions in the FEM mesh (see the edges of the dielectric layer and the normal contacts in the potential of Fig. 6.5b), the projected potential $\hat{\phi}(x)$ shows some roughness that may cause unwanted scattering events (see black curve in Fig. 6.5c). To avoid this, we fit $\hat{\phi}(x)$ to a linear combination of hyperbolic tangents, given by

$$V(x) = \frac{E_a}{2} \left[\tanh\left(\frac{x - x_s + W/2}{\lambda/2} \right) - \tanh\left(\frac{x - x_s - W/2}{\lambda/2} \right) \right] + E_s. \tag{6.4}$$

Here, E_a is the amplitude, W the width and E_s the downshift in energy of the potential barrier, which varies along x on a typical length scale λ, as indicated in Fig. 6.5c). The horizontal shift of the barrier to the middle of the nanowire is denoted by $x_s = 500$ nm.

The parameter λ expresses the smoothness of the barrier. We find that λ is close to zero when no charge is present in the wire and the boundary conditions result in an abrupt step in the potential between the contacts and the uncovered part of the wire. When charge enters the wire, it screens the electric field, thereby smoothening the potential. For a QPC length of 325 nm we find in this regime $\lambda \approx 80$ nm. The value of λ is reduced for smaller QPC lengths, but saturates to $\lambda \approx 80$ nm for longer QPC lengths. Moreover we find that λ has only a little dependency on the back gate voltage V_G or the applied magnetic field B (Fig. 6.5d). Taking advantage of the latter and the fact that we are interested in the conductance of the wire in the vicinity of the helical-gap feature – where the screening *is* present – we assume λ constant in V_G and B space for the conductance calculation.

For the conductance calculations we consider transport through a two-mode nanowire described by the Hamiltonian

$$\mathcal{H} = \left[\frac{\hbar^2 k_x^2}{2m^*} + V(x) \right] \sigma_0 + \alpha \sigma_y k_x + \frac{1}{2} g \mu_B B (\sigma_x \sin\theta + \sigma_y \cos\theta), \quad (6.5)$$

where σ denote the Pauli matrices (with σ_0 the identity matrix) and $V(x)$ is fit to the projected potential barrier, as expressed in Eqs. 6.3 and 6.4. Spin-orbit coupling strength is given by $\alpha = \hbar^2 / m^* l_{SO}$ where l_{SO} we use as a free parameter. We take the effective mass $m^* = 0.014 m_0$ of InSb and $g = 38$ (unless stated otherwise) as estimated in the main text. Note that for the coordinate system used here, where the wire lies along the x direction and θ is the angle between B_{SO} and the external magnetic field. The Hamiltonian Eq. 6.5 is discretized on a mesh with lattice spacing $\Delta x = 4$ nm. Assuming translational invariance of the boundary conditions at the ends of the wire one arrives at the scattering problem that is solved using the Kwant package [31] to obtain the linear-response conductance within the Landauer-Büttiker formalism.

6.7.2. Angle Dependence of the Conductance in Rashba Nanowires
Theoretical Model
We consider a one-dimensional nanowire with Rashba spin-orbit interaction (SOI) in an external magnetic field **B**. The field **B** is oriented at an angle θ with respect to the effective magnetic field $\mathbf{B}_{so}$ due to Rashba SOI, as shown in Fig. 6.5e). This setup is described by the Hamiltonian:[2]

$$H = \frac{p^2}{2m^*} + \frac{\alpha}{\hbar} p \sigma_y + \frac{1}{2} E_Z \left(\sin(\theta) \sigma_x + \cos(\theta) \sigma_y \right). \quad (6.6)$$

In this expression, p is the momentum operator, m^* is the effective mass, α the Rashba SOI-strength, and $\sigma_{x,y}$ the Pauli matrices. The Zeeman energy $E_Z = g \mu_B B$, where g is the g-factor, and μ_B the Bohr magneton. In Eq. (6.6) we assumed without loss of generality a magnetic field in the x-y-plane; the band structure however only depends on the relative angle θ of **B** with $\mathbf{B}_{so}$.

The Rashba SO-strength α can be related to an effective length scale, the spin-orbit length

$$l_{so} = \frac{\hbar^2}{m\alpha} \quad (6.7)$$

and to an energy scale, the spin-orbit energy

$$E_{so} = \frac{m\alpha^2}{2\hbar^2}. \quad (6.8)$$

Defining length in units of l_{so} and energy in units of E_{so} it is possible to write the Hamiltonian in a convenient dimensionless form:

$$H = \frac{d^2}{dx^2} + 2\frac{d}{dx}\sigma_y + \frac{1}{2}\frac{E_Z}{E_{so}}(\sin(\theta)\sigma_x + \cos(\theta)\sigma_y). \quad (6.9)$$

Proper units will be restored in the final result.

In an translationally invariant nanowire, the wave vector k is a good quantum number and the Rashba Hamiltonian is readily diagonalized as [2]

$$E_\pm(k) = k^2 \pm \frac{1}{2}\sqrt{\left(\frac{E_Z}{E_{so}}\right)^2 + 16k^2 + 8\frac{E_Z}{E_{so}}k\cos(\theta)}. \tag{6.10}$$

The resulting band structure for a general angle θ is shown schematically in the left panel of Fig. 6.5f). The band structure can be related to an idealized quantum point contact (QPC) conductance by counting the number of propagating modes at a given energy E (see right panel of Fig. 6.5f).

In the following we will derive from the band structure: (i) the size of the $1e^2/h$ plateaus in energy (denoted by $\Delta E_{Z,1}$ and $\Delta E_{Z,2}$). This is directly measurable using the finite bias dependence of the QPC conductance (measuring so-called QPC diamonds). (ii) The critical field for which the spin-orbit induced $2e^2/h$ conductance (the size of this plateau is denoted as ΔE_{so}) vanishes. This allows for an estimate of the spin-orbit strength from the magnetic field dependence in experiment.

SIZE OF ZEEMAN-INDUCED GAPS

In order to compute the size of the different QPC plateaus in energies, we need to compute the value of the minima and maxima of the bands $E_\pm(k)$. This can be done exactly using a computer algebra program (we used Mathematica), as it only involves solving for the roots of polynomials up to fourth order. The resulting expressions are however quite cumbersome, and it is more useful to find an approximate expression doing a Taylor approximation. Up to second order in E_z/E_{so} we then find the simple expressions

$$\Delta E_{Z,1} \approx E_Z \sin\theta, \tag{6.11}$$

$$\Delta E_{Z,2} \approx E_Z \cos\theta. \tag{6.12}$$

CRITICAL MAGNETIC FIELD FOR THE SPIN-ORBIT INDUCED $2e^2/h$-PLATEAU

The spin-orbit induced $2e^2/h$ region persists only up to a critical Zeeman splitting $E_{Z,crit}$, after which the two $1e^2/h$-plateaus merge into one. In the band structure, this corresponds to a transition from three extrema in $E_-(k)$ (two minima, one maximum) to only one minimum. The critical Zeeman splitting where this happens can be solved for exactly using Mathematica:

$$\frac{E_{Z,crit}}{E_{so}} = \sqrt{\frac{54\cos(8\theta) + 3M_1^{\frac{2}{3}} + 6\left(3M_1^{\frac{1}{3}} - 4\right)\cos(4\theta) - 2M_1^{\frac{1}{3}} - 30}{M_2^{\frac{1}{3}}}} \tag{6.13}$$

where

$$M_1 = 68 - 86\cos(4\theta) - 36\cos(8\theta) + 54\cos(12\theta) + 512\sqrt{\sin^4(2\theta)\cos^2(2\theta)} \tag{6.14}$$

$$M_2 = 68 - 86\cos(4\theta) - 36\cos(8\theta) + 54\cos(12\theta) + 256\sqrt{\sin^2(2\theta)\sin^2(4\theta)} \tag{6.15}$$

For $\theta = 17°$ this gives $E_{Z,\text{crit}} = 2.386 E_{\text{so}}$ and for $\theta = 10°$ $E_{Z,\text{crit}} = 2.695 E_{\text{so}}$. When the value of the nanowire g-factor is extracted from experiment, the critical Zeeman splitting can be translated into a critical magnetic field. The magnetic field up to which the spin-orbit induced $2e^2/h$-plateau is still visible in experiment can then be used to set a *lower bound* on the spin-orbit energy. It is a lower bound, as for a given QPC potential the $2e^2/h$ may not be visible any more despite in principle being present in the band structure. A more detailed transport calculation can be used to improve on this bound.
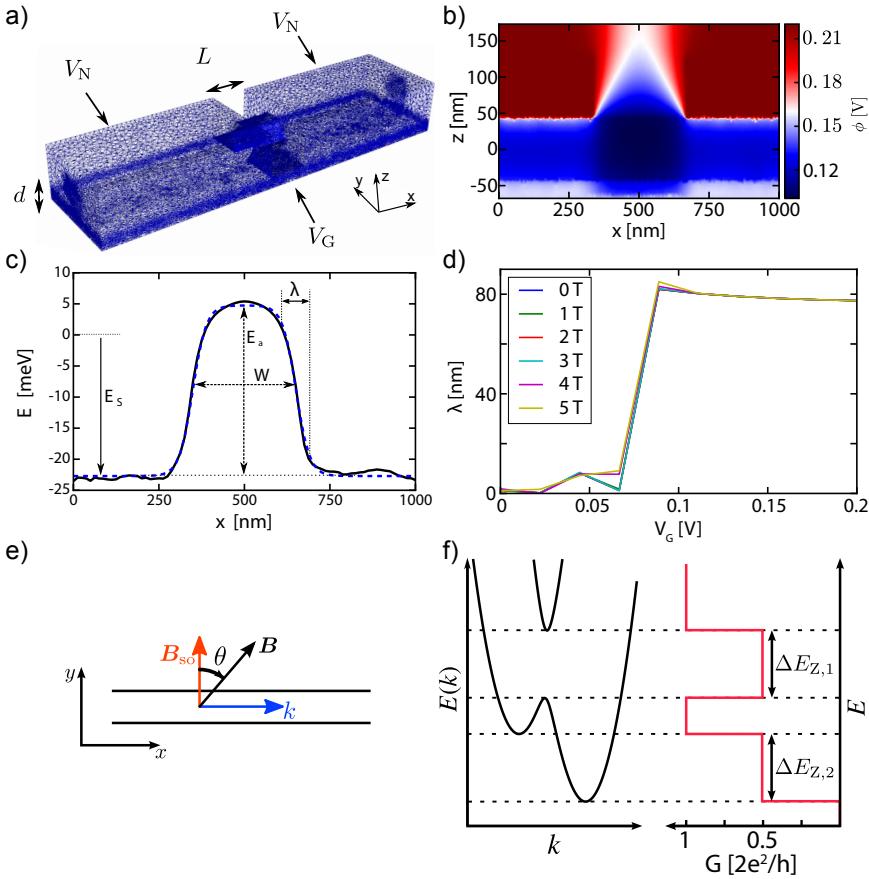
6

Figure 6.5: **a)** Example of a finite element mesh used for 3D Poisson calculations. L denotes the QPC length (spacing between the two contacts), d the thickness of the dielectric layer, which is set to 20 nm. L is set to 325 nm for the simulations in the main text, and varied from 175 to 425 nm to show the length dependence of the helical gap feature in Fig. 6.12. The two boundary conditions applied are a potential V_N on the contacts and a potential V_G underneath the dielectric layer. The mesh between the two contacts is left out for visibility purposes. **b)** Cross section plot of the 3D Poisson potential for $V_G = 0.156$ V and $V_N = 0.22$ V. The cross section is taken along the wire axis (x-axis) for fixed $y = 0$ nm in the middle of the wire. The effective QPC length runs from ~ 340 to ~ 660 nm. The nanowire is situated between $z = -50$ nm and $z = 50$ nm. **c)** Projected potential $\hat{\phi}(x)$ (black curve) and fitted potential $V(x)$ (blue dashed curve) for $V_G = 0.156$ V, corresponding to the potential of Fig. 6.5b). Indicated are the fitting parameters E_s, E_a, W and λ of the function Eq. 6.4. **d)** The fitting parameter λ as a function of back gate voltage V_G. Different colors denote different magnetic field strengths B. A jump in $\lambda \approx 0$ (abrupt step potential) to $\lambda \approx 80$ nm occurs when charge enters the wire, screening the electric field. **e)** Rashba nanowire in an external magnetic field: the one-dimensional nanowire is oriented along the x-axis, and the spin-orbit field $\mathbf{B}_{so}$ perpendicular, along the y-axis. The external magnetic field $\mathbf{B}$ forms an angle θ with respect to $\mathbf{B}_{so}$. **f)** Schematic picture of the band structure $E(k)$ of a Rashba nanowire in a magnetic field (left panel) and the corresponding quantum point conductance G (right panel).

6.7.3. DEVICE 1 - ADDITIONAL DATA
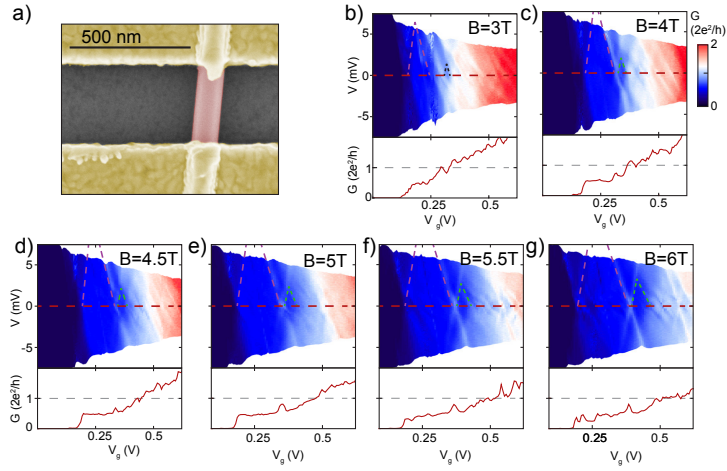
Figure 6.6: Voltage bias spectroscopy **a)** False color SEM image of device 1. The InSb nanowire is shown in red and Cr/Au contacts in yellow. **b)–g)** Conductance measurements as a function of QPC gate voltage V_g and source-drain bias voltage V_{sd} at increasing magnetic field. Dotted lines indicate the helical gap as well as the $0.5 \cdot G_0$ plateau. The helical gap shows as feature stable in V_{sd} and evolves linearly with magnetic field.

6
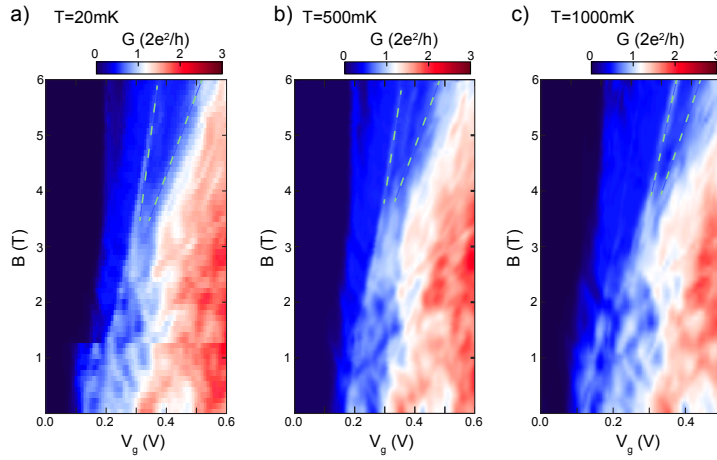
Figure 6.7: Temperature dependence of the helical gap. Measurements of the differential conductance dI/dV ($V_{sd} = 0\,\mathrm{mV}$) as function of magnetic field at **a)** T = 20 mK **b)** T = 500 mK **c)** T = 1000 mK. The helical gap (dotted lines) evolves similarly in all three measurements showing that it stays stable at increased temperatures as expected for the energy scale extracted for E_{SO}
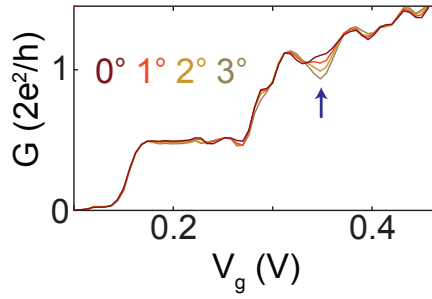
Figure 6.8: Additional linecuts of the angle dependence. A small remaining conductance dip can be seen in the linecut at 0° in Fig. 6.4c). This is likely due to imperfect alignment between the external magnetic field and B_{SO}, either due to the limited range of the vector magnet or due to a small misalignment between the sample plane and the magnets x-y plane. Linecuts of Fig. 6.4c) taken at 0°, 1°, 2° and 3° further emphasize the strong angle dependence of the observed reentrance feature.

6.7.4. DEVICE 2 - DATA
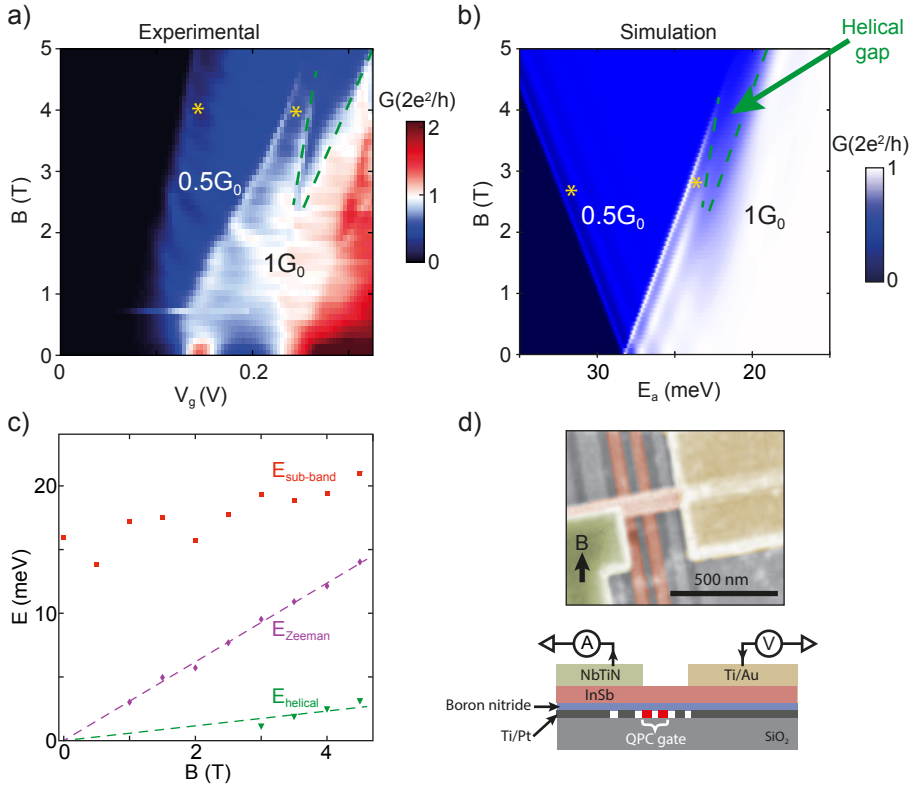
Figure 6.9: Measurements of a second device. **a)** Differential conductance dI/dV as function of QPC gate Voltage V_g and magnetic field B. Around B = 2 T a gap opens in the $1 \cdot G_0$ plateau and increases linearly with magnetic field. At the onset of the $0.5 \cdot G_0$ and the $1 \cdot G_0$ plateaus Fabry-Perot resonances are visible (yellow asterisk). In contrast to the helical gap the width of the resonances stays constant at changing magnetic field. **b)** Numerical simulations of the helical gap with $\theta = 10°$, $g = 53$ and $E_{SO} = 5.6$ meV. We use the potential parametrization as for the device discussed in the main text and find a good agreement with the data shown in a) for $\lambda = 40$ nm and $W = 300$ nm. **c)** Evolution of the energy levels with magnetic field extracted from the scans shown in Fig. 6.10. Dotted lines show fits with intercept fixed at zero and we find a subband spacing $E_{subband} = 18 \pm 2$ meV and g-factor $g = 53 \pm 1$. By comparing the slopes of $E_{Zeeman} \sim E_Z \cos\theta$ and $E_{helical} \sim E_Z \sin\theta$ we find $\theta = 10° \pm 2°$. **d)** Cross section and false color SEM image of device 2. An InSb nanowire (orange) is contacted by one Ti/Au electrode (yellow) and one NbTiN electrode (green). Two bottom gates (red) are combined to form the QPC constriction. The black arrow indicates the orientation of the applied magnetic field. Measurements are taken at 20 mK with the use of standard lock-in technique (100 μV excitation at 73 Hz).
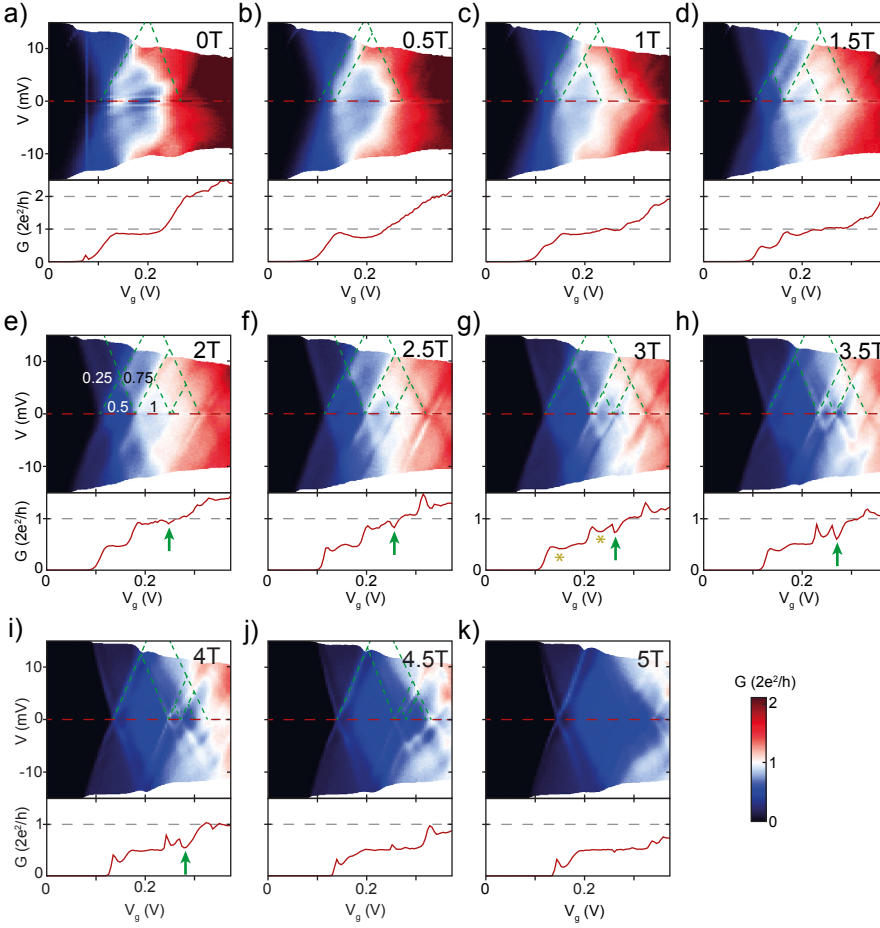
Figure 6.10: Voltage bias spectroscopy of device 2 at increasing magnetic field. **a) – k)** (Top) Differential conductance dI/dV as a function of QPC gate voltage V_g and bias voltage V_{sd}. Conductance plateaus show up as diamond shaped region indicated by dashed green lines and can be used to extract the energy spacings shown in Fig. 6.9c). Conductance traces in the bottom panels show line cuts taken at $V_{sd} = 0$ mV. Green arrows in **e)–i)** indicate the position of the helical dip. Yellow asterisks in **g)** indicate conductance dips originating from Fabry-Perot resonances also visible in Fig. 6.9a). Numbers in **e)** denote conductance in units of $2e^2/h$.

6.7.5. CONTROL DEVICES

QPC LENGTH DEPENDENCE
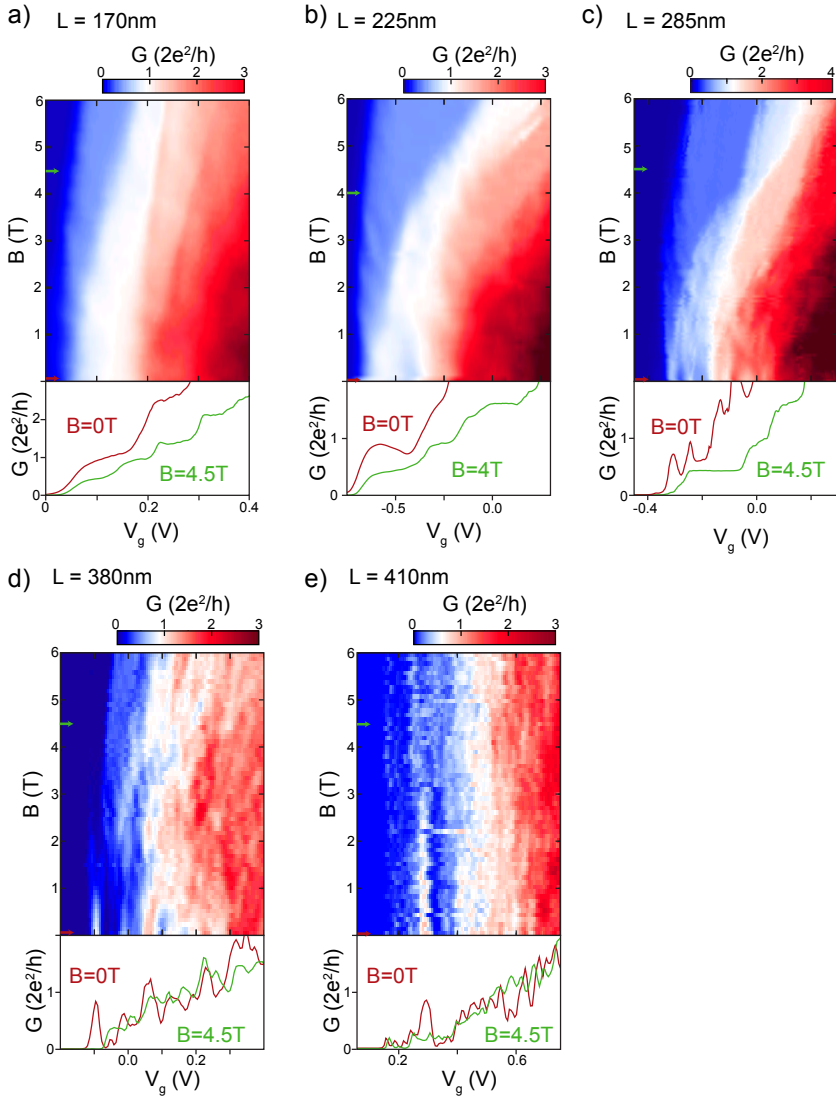
Figure 6.11: Length dependence of nanowire QPCs. Magneto-conductance measurements (at $V_{sd} = 0\,\text{mV}$) of QPCs with increasing length. The contact spacing L is changed in Steps of ~ 50 nm. **a) – c)** are shorter and **d),e),** longer than device 1 (L = 325 nm). Line traces at 0 T and finite field are added in the bottom panel. The short channel devices **a),b)** show well defined and flat plateaus throughout the full magnetic field range. For intermediate channel lengths, **c)**, resonances start to appear and modify the conductance at low magnetic fields. Long channel devices, **d),e)**, are dominated by backscattering and conductance fluctuations dominate for the full magnetic field range.

SIMULATIONS - LENGTH DEPENDENCE
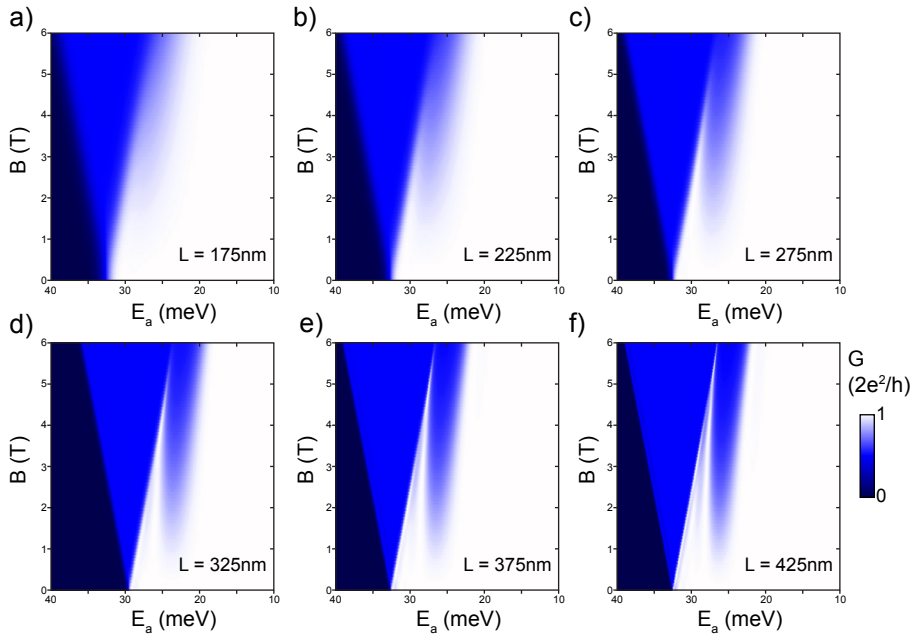
Figure 6.12: Simulations for a QPC of different lengths at fixed angle $\theta = 17°$, $l_{SO} = 20$ nm. The contact spacing L is increased in steps of 50 nm starting from $L = 175$ nm (**a**), up to $L = 425$ nm (**f**). The simulations demonstrate the reduced visibility of the helical gap in short devices. At increasing channel length the conductance dip becomes sharper and sets on at lower magnetic fields. A clear reentrant feature can only be seen in **d),e),f)** which are at the limit of experimental capabilities (Fig. 6.11).

6.7.6. Simulations - Angle Dependence
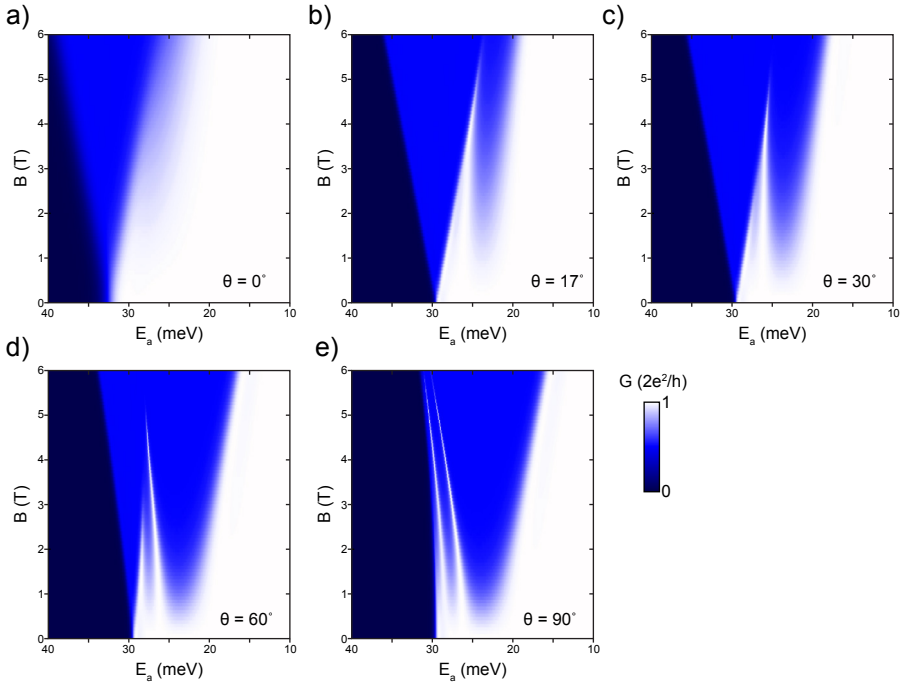
Figure 6.13: Simulations of the angle dependence for a QPC with fixed length $L = 325$ nm. θ is the angle between B_{SO} and the applied magnetic field as defined in the main text. **a)** For $\theta = 0°$, $B_{ext} \parallel B_{SO}$ and the helical gap disappears. **b) – e)** at increasing angles θ the width of the helical gap increases and the width of the initial $0.5 \cdot G_0$ plateau decreases.

6.7.7. SIMULATIONS - SPIN-ORBIT STRENGTH
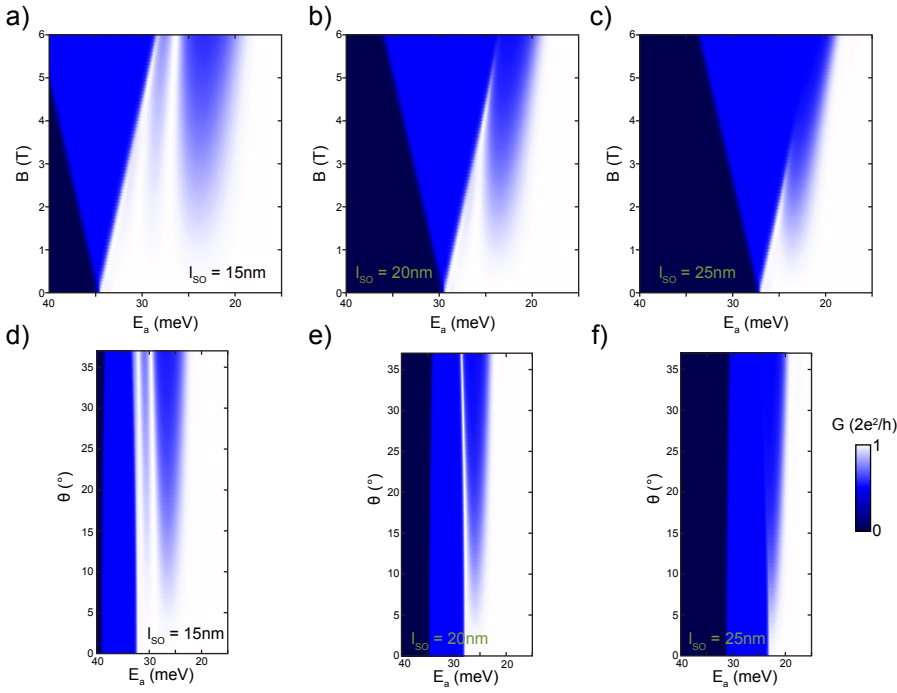
Figure 6.14: Simulations of the magnetoconductance for varying l_{SO}. Variations of $l_{SO} = 1/k_{SO}$ strongly influence the visibility of the helical gap in QPC conductance measurements. The simulations for **a),b),c)** used identical QPC length L = 325 nm and offset angle $\theta = 17°$

REFERENCES

[1] P. Středa and P. Šeba, "Antisymmetric spin filtering in one-dimensional electron systems with uniform spin-orbit coupling," *Phys. Rev. Lett.*, vol. 90, p. 256601, Jun 2003.

[2] Y. V. Pershin, J. A. Nesteroff, and V. Privman, "Effect of spin-orbit interaction and in-plane magnetic field on the conductance of a quasi-one-dimensional system," *Phys. Rev. B*, vol. 69, p. 121306, Mar 2004.

[3] K. Sato, D. Loss, and Y. Tserkovnyak, "Cooper-pair injection into quantum spin hall insulators," *Phys. Rev. Lett.*, vol. 105, p. 226401, Nov 2010.

[4] R. I. Shekhter, O. Entin-Wohlman, M. Jonson, and A. Aharony, "Rashba splitting of cooper pairs," *Phys. Rev. Lett.*, vol. 116, p. 217001, May 2016.

[5] J. Alicea, Y. Oreg, G. Refael, F. Von Oppen, and M. P. Fisher, "Non-abelian statistics and topological quantum information processing in 1d wire networks," *Nature Physics*, vol. 7, no. 5, pp. 412–417, 2011.

[6] C. Nayak, S. H. Simon, A. Stern, M. Freedman, and S. Das Sarma, "Non-abelian anyons and topological quantum computation," *Rev. Mod. Phys.*, vol. 80, pp. 1083–1159, Sep 2008.

[7] Y. Oreg, G. Refael, and F. von Oppen, "Helical liquids and majorana bound states in quantum wires," *Phys. Rev. Lett.*, vol. 105, p. 177002, Oct 2010.

[8] G. Dresselhaus, "Spin-orbit coupling effects in zinc blende structures," *Phys. Rev.*, vol. 100, pp. 580–586, Oct 1955.

[9] E. Rashba and V. Sheka, "Symmetry of energy bands in crystals of wurtzite type ii. symmetry of bands with spin-orbit interaction included," *Fiz. Tverd. Tela: Collected Papers*, vol. 2, p. 162–176, 1959.

[10] R. Winkler, S. Papadakis, E. De Poortere, and M. Shayegan, *Spin-Orbit Coupling in Two-Dimensional Electron and Hole Systems*, vol. 41. Springer, 2003.

[11] M. König, S. Wiedmann, C. Brüne, A. Roth, H. Buhmann, L. W. Molenkamp, X.-L. Qi, and S.-C. Zhang, "Quantum spin hall insulator state in hgte quantum wells," *Science*, vol. 318, no. 5851, pp. 766–770, 2007.

[12] K. C. Nowack, E. M. Spanton, M. Baenninger, M. König, J. R. Kirtley, B. Kalisky, C. Ames, P. Leubner, C. Brüne, H. Buhmann, *et al.*, "Imaging currents in hgte quantum wells in the quantum spin hall regime," *Nature materials*, vol. 12, no. 9, pp. 787–791, 2013.

[13] C. Quay, T. Hughes, J. Sulpizio, L. Pfeiffer, K. Baldwin, K. West, D. Goldhaber-Gordon, and R. De Picciotto, "Observation of a one-dimensional spin–orbit gap in a quantum wire," *Nature Physics*, vol. 6, no. 5, pp. 336–339, 2010.

[14] J. Klinovaja, M. J. Schmidt, B. Braunecker, and D. Loss, "Helical modes in carbon nanotubes generated by strong electric fields," *Physical review letters*, vol. 106, no. 15, p. 156809, 2011.

[15] J. Klinovaja, P. Stano, A. Yazdani, and D. Loss, "Topological superconductivity and majorana fermions in rkky systems," *Physical review letters*, vol. 111, no. 18, p. 186805, 2013.

[16] V. Mourik, K. Zuo, S. M. Frolov, S. R. Plissard, E. P. A. M. Bakkers, and L. P. Kouwenhoven, "Signatures of majorana fermions in hybrid superconductor-semiconductor nanowire devices," *Science*, vol. 336, no. 6084, pp. 1003–1007, 2012.

[17] S. M. Albrecht, A. Higginbotham, M. Madsen, F. Kuemmeth, T. S. Jespersen, J. Nygård, P. Krogstrup, and C. Marcus, "Exponential protection of zero modes in majorana islands," *Nature*, vol. 531, no. 7593, pp. 206–209, 2016.

[18] D. Rainis and D. Loss, "Conductance behavior in nanowires with spin-orbit interaction: A numerical study," *Phys. Rev. B*, vol. 90, p. 235415, Dec 2014.

6

[19] J. Kammhuber, M. C. Cassidy, H. Zhang, Ö. Gül, F. Pei, M. W. de Moor, B. Nijholt, K. Watanabe, T. Taniguchi, D. Car, *et al.*, "Conductance quantization at zero magnetic field in insb nanowires," *Nano letters*, vol. 16, no. 6, pp. 3482–3486, 2016.

[20] S. Heedt, W. Prost, J. Schubert, D. Grützmacher, and T. Schäpers, "Ballistic transport and exchange interaction in inas nanowire quantum point contacts," *Nano letters*, vol. 16, no. 5, pp. 3116–3123, 2016.

[21] I. van Weperen, S. R. Plissard, E. P. A. M. Bakkers, S. M. Frolov, and L. P. Kouwenhoven, "Quantized conductance in an insb nanowire," *Nano Lett.*, vol. 13, no. 2, pp. 387–391, 2012.

[22] S. Nadj-Perge, V. Pribiag, J. Van den Berg, K. Zuo, S. Plissard, E. Bakkers, S. Frolov, and L. Kouwenhoven, "Spectroscopy of spin-orbit quantum bits in indium antimonide nanowires," *Physical review letters*, vol. 108, no. 16, p. 166801, 2012.

[23] I. Van Weperen, B. Tarasinski, D. Eeltink, V. Pribiag, S. Plissard, E. Bakkers, L. Kouwenhoven, and M. Wimmer, "Spin-orbit interaction in insb nanowires," *Physical Review B*, vol. 91, no. 20, p. 201413, 2015.

[24] S. Koelling, A. Li, A. Cavalli, S. Assali, D. Car, S. Gazibegovic, E. P. Bakkers, and P. M. Koenraad, "Atom-by-atom analysis of semiconductor nanowires with parts per million sensitivity," *Nano Lett.*, vol. 17, no. 2, pp. 599–605, 2017.

[25] J. Cayao, E. Prada, P. San-Jose, and R. Aguado, "Sns junctions in nanowires with spin-orbit coupling: Role of confinement and helicity on the subgap spectrum," *Physical Review B*, vol. 91, no. 2, p. 024514, 2015.

[26] J. Heyder, F. Bauer, E. Schubert, D. Borowsky, D. Schuh, W. Wegscheider, J. von Delft, and S. Ludwig, "Relation between the 0.7 anomaly and the kondo effect: Geometric crossover between a quantum point contact and a kondo quantum dot," *Physical Review B*, vol. 92, no. 19, p. 195401, 2015.

[27] O. Goulko, F. Bauer, J. Heyder, and J. von Delft, "Effect of spin-orbit interactions on the 0.7 anomaly in quantum point contacts," *Phys. Rev. Lett.*, vol. 113, p. 266402, Dec 2014.

[28] J. D. Sau, S. Tewari, and S. D. Sarma, "Experimental and materials considerations for the topological superconducting state in electron-and hole-doped semiconductors: Searching for non-abelian majorana modes in 1d nanowires and 2d heterostructures," *Physical Review B*, vol. 85, no. 6, p. 064512, 2012.

[29] S. R. Plissard, D. R. Slapak, M. A. Verheijen, M. Hocevar, G. W. G. Immink, I. van Weperen, S. Nadj-Perge, S. M. Frolov, L. P. Kouwenhoven, and E. P. A. M. Bakkers, "From insb nanowires to nanocubes: Looking for the sweet spot," *Nano Lett.*, vol. 12, no. 4, pp. 1794–1798, 2012.

[30] A. Logg, K.-A. Mardal, and G. Wells, *Automated solution of differential equations by the finite element method: The FEniCS book*, vol. 84. Springer Science & Business Media, 2012.

6

[31] C. W. Groth, M. Wimmer, A. R. Akhmerov, and X. Waintal, "Kwant: a software package for quantum transport," *New J. Phys.*, vol. 16, no. 6, p. 063065, 2014.

[32] N. March, "The thomas-fermi approximation in quantum mechanics," *Advances in Physics*, vol. 6, no. 21, pp. 1–101, 1957.

[33] V. Eyert, "A comparative study on methods for convergence acceleration of iterative vector sequences," *Journal of Computational Physics*, vol. 124, no. 2, pp. 271 – 285, 1996.

6

7

ENHANCED CHARGE-CAVITY COUPLING IN AN INSB NANOWIRE QUANTUM DOT SYSTEM

M. C. Cassidy, J. Kammhuber, D. de Jong, D. Car, S. R. Plissard, E. P. A. M Bakkers and L. P. Kouwenhoven

We present measurements of an InSb nanowire double quantum dot coupled to a superconducting half-wave resonator. Precise nanowire alignment at the electric field antinodes maximizes the electric field along the nanowire without compromising the intrinsic quality factor of the cavity, allowing us to measure a charge cavity coupling rate of $g_c/2\pi = 150\,\mathrm{MHz}$.

7.1. INTRODUCTION

Superconducting coplanar waveguide (CPW) resonators are sensitive probes of their electromagnetic environment, and have found applications in astronomical detection [1], electron spin resonance [2] and quantum information processing [3–5]. Recently, they have been integrated with mesoscopic quantum devices, where small changes in the cavity transmission have been used to probe the energy spectrum of single and double quantum dot devices [6–11]. Typically coupling strengths between the semiconductor quantum dot system and the cavity photons are in the range 10–50 MHz, and so the strong coupling regime has only been achievable in material systems where charge noise is low, such as 2-dimensional electron gases (2DEGs) grown via molecular beam epitaxy (MBE) [10, 11]. Directly increasing the coupling strength, either through the use of high inductance resonators [11, 12] or by careful device design provides an alternative route to reaching the strong coupling regime in systems where charge noise is significant, or for the exploration of more sophisticated quantum effects such as squeezed light or reaching the ultra-strong coupling regime in hybrid devices.

The strong spin-orbit interaction and large g-factor in InAs and InSb nanowires [13, 14] together with their ability to be proximitized by a nearby superconductor [15, 16] makes them ideal candidates for topological quantum devices. Recently, several proposals have emerged for coupling nanowires hosting Majorana bound states to superconducting resonators [17–22]. Here, the resonator can be used for detecting the presence of Majorana bound states in individual nanowires [19–21], or for reading out the qubit state in more complex topological qubit devices [17, 18, 22]. An architecture that combines existing nanowire devices with superconducting microwave resonators while maximizing the charge-photon interaction is of great interest for topological quantum computation.

Here we report microwave measurements of a InSb nanowire double quantum dot embedded inside a $\lambda/2$ resonator. Precise and deterministic nanowire deposition maximizes the interaction between the dipole moment of an electron in the quantum dot and the cavity photons resulting in a coupling strength of ~ 150 MHz. Our efficient device fabrication minimizes the required number of fabrication step which reduces the exposure to fabrication residues and ensures high device yield.

7.2. DEVICE LAYOUT

Figure 7.1a) shows an optical microscope image of our device. It consists of the $\lambda/2$ CPW resonator (l = 6650 μm) formed from a sputtered NbTiN film with a central conductor width of 10 μm and ground plane gap of 1.5 μm. At each end of the cavity the central conductor is interrupted with a finger capacitor, which provides a coupling to the external transmission lines at a rate $\kappa_{in} = \kappa_{out} = 15$ MHz. At the electric field antinodes of the cavity, the electric field is strongly enhanced due to the small mode volume of the resonator. At these antinodes we define a small cutout with five fine gates (60 nm/80 nm pitch) where the nanowire DQD is located (Fig. 7.1b). A spiral inductor located at the electric field node of the cavity allows for a DC bias to applied directly to the device [6, 23]. The resonator, spiral inductor, ground plane patterning, fine gate structure and bondpads are defined by electron beam lithography followed by a reactive SF_6/O_2 dry
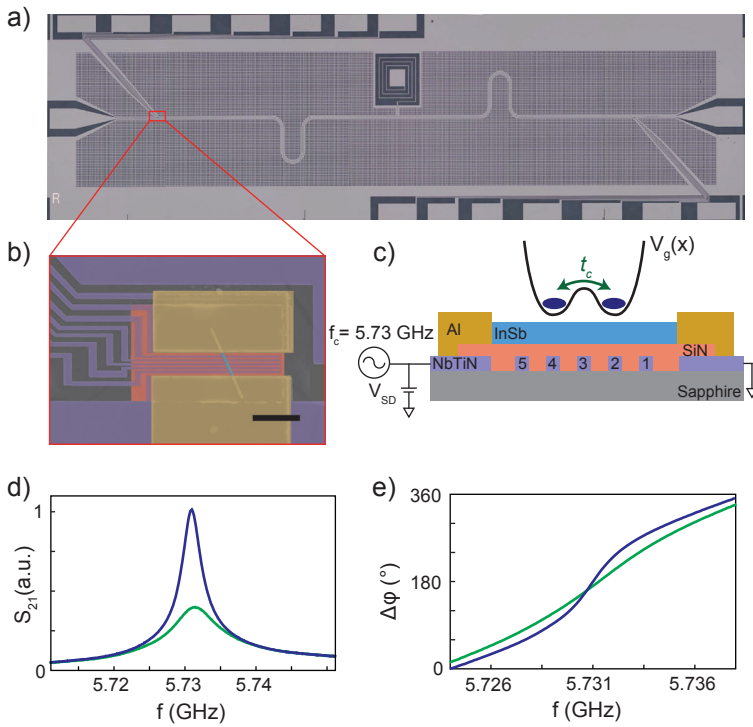
Figure 7.1: **a)** Optical microscope image of the hybrid nanowire-resonator device. The $\lambda/2$ resonator and gate structure are formed by reactive ion etching of a NbTiN film in a single fabrication step. **b)** False colored scanning electron micrograph and **c)** schematic cross-section of the nanowire double quantum dot device located at the electric field antinode of the cavity. The scale bar in (b) is $1\,\mu m$. Normalized **d)** amplitude and **e)** phase of the transmitted microwave signal when the double quantum dot is in coulomb blockade (blue) or at an interdot transition (green).

etch. Using a very thin superconducting film (~ 25 nm) together with a high resolution resist (CSAR ARP 6001) enables us to define and etch all these structures in a single fabrication step. Additionally, making the gates out of a thin, narrow superconductor with high kinetic inductance such as NbTiN minimizes radiative losses from the resonator that have limited previous hybrid devices [6, 7] and avoids the need for additional LC filtering on the gates [24]. Following the definition of the resonator and fine gate structure, a small window is opened up above the fine gates, 30 nm Si_3N_4 is sputtered as a gate dielectric, and a single InSb nanowire is deposited on top of the gates using a micro manipulator [25], as shown in Fig. 7.1b,c). This deterministic deposition technique allows for the nanowire to be positioned with high spatial and rotational accuracy, further enhancing the coupling to the cavity and resulting in near perfect device yield. Finally, aluminium contacts are added to define the electrochemical potential in the nanowire with one end directly connected to the central resonator to further increase the coupling strength. Once again, the use of a superconducting material rather than a normal metal for the contacts reduces radiative losses from the cavity.

The finished device is bonded in a custom printed circuit board and encased in a radiation tight shield painted with Aeroglaze Z306 to further suppresses spurious cavity modes. Measurements were carried out using a dilution refrigerator with 15 mK base temperature using standard heterodyne demodulation techniques [3]. Briefly, a probe frequency, f_P , is applied to the cavity at an input power (P_{in} = -130 dBm), amplified and mixed with a local oscillator at frequency f_{LO} resulting in an intermediate frequency ($f_{IF} = f_{LO}$-f_P = 1 MHz) before being further amplified, filtered and digitized with a fast acquisition card (Alazar). From this we extract the in-phase (I) and quadrature (Q) components of the cavity response, and calculate the amplitude and phase of the transmitted signal $Ae^{i\phi} = I + iQ$. A Lorentzian fit to the bare cavity transmission when the nanowire is tuned deeply into Coulomb blockade gives the resonance frequency f_0 = 5.7308 GHz and linewidth δf_0 = 2.45 MHz as shown in Fig. 7.1d,e) (blue), corresponding to a loaded quality factor of Q = 2300. In contrast, when the double quantum dot is tuned such that electron tunneling events between the two quantum dots or between a quantum dot and a lead result in an additional dissipative path for cavity photons, the cavity frequency shifts and the quality factor to reduces, as shown in Fig. 7.1d,e) (green).

7.3. RESULTS

Figure 7.2 shows a typical hexagonal charge stability diagram for the double quantum dot in the many electron regime when a finite bias voltage V_{SD} = 1 mV is applied across the device. Good agreement is seen between the signal acquired using standard DC transport techniques (Fig. 7.2a), with that seen in the amplitude (Fig. 7.2b) and phase (Fig. 7.2c) response of the transmitted microwave signal at a probe frequency of f_P = 5.3077 GHz. At fixed occupancy (N,M) of the double dot, transport is blocked when the individual energy level are misaligned with each other and with the source and drain contacts. At the charge degeneracy points where three hexagons meet, all energy levels are aligned and transport through both dots is allowed. Due to the finite bias voltage these points expand into triangular regions of finite conductance [26], which we use to extract the lever arm of gates 2 and 4 $E_{l(r)} = \eta_{4(2)} V_{g4(g2)}$. In the DC transport data, the four remaining edges of the hexagons are almost invisible because cotunneling of electrons
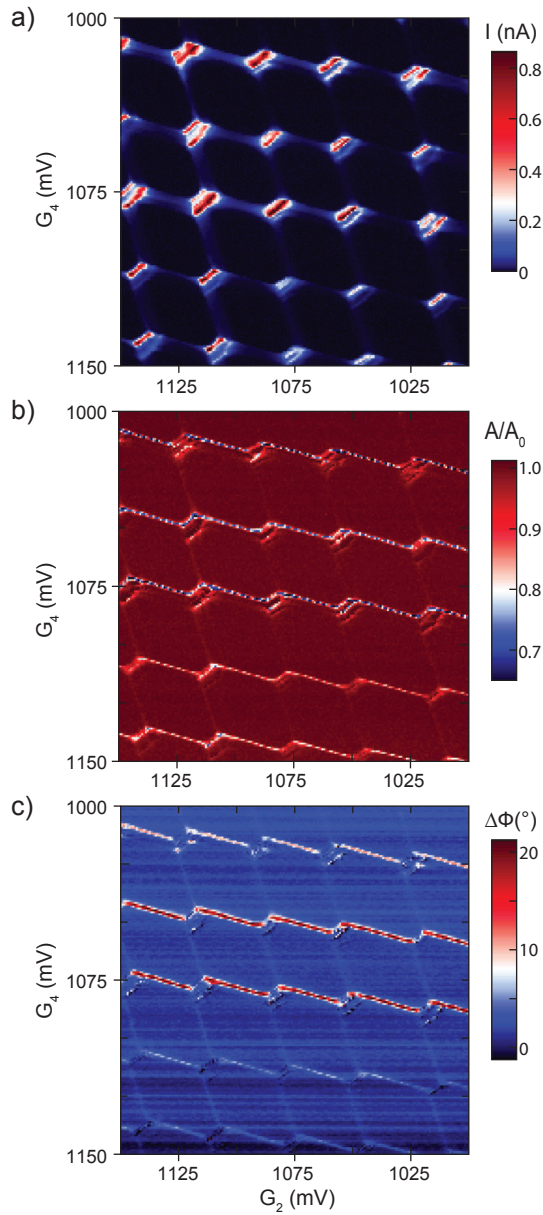
Figure 7.2: Charge stability diagram of the double dot. **a)** Current flowing through the double quantum dot device measured as function of the plunger gates g_2 and g_4 at bias voltage $V_{SD} = 1\,\text{mV}$. **b)** Amplitude and **c)** phase response of the microwave transmission recorded simultaneously to a).

through the misaligned dot is necessary to observe a transport signal. In contrast, all edges of the hexagon can be clearly resolved in the resonator response as the resonator is also sensitive to electron tunneling events in only one of the two quantum dots. The quantum dot closest to the cavity, controlled by V_{g4} displays an enhanced response, similar to earlier reports [7, 27]. The cross coupling between gates 4 and 5 means that the tunnel barrier closest to the resonator increases at more positive V_{g4} which decreases the observed asymmetry between gate 2 and gate 4.

Close to the interdot charge transition between $(N + 1, M)$ into $(N, M + 1)$, the two charge states hybridize and the DQD device can be considered as a charge qubit with an energy splitting $\Omega = \sqrt{\epsilon^2 + 4t_c^2}$, where ϵ is the detuning controlled by the tunnel coupling t_c (Fig. 7.3a,b). Close to this detuning point, the amplitude and phase of the resonator response depends critically on t_c, as the qubit moves from below the resonator frequency (Fig. 7.3c), to on resonance (Fig. 7.3d), to well above the resonator frequency (Fig. 7.3e). To quantify the charge-cavity coupling, we systematically study the evolution of the cavity response as a function of interdot detuning as t_c is tuned from far below the resonator frequency to far above it, as shown in Fig. 7.4. For each case, we compensate the values of V_{g2} and V_{g4} for the change of V_{g3} so that we study the same charge transition across the same detuning range. A distinct suppression in the transmitted signal's amplitude and a change in the sign of the signal's phase is seen as t_c approaches the resonator frequency. The double quantum dot coupled to the microwave photons in the cavity can be described by a Jaynes-Cummings hamiltonian [6] with the two qubit states $\Omega_\pm = \pm\frac{1}{2}\Omega$ interacting with the quantized electric field of the cavity.

$$H_{tot} = \hbar\Delta_C a^\dagger a + \frac{\hbar\Delta_\Omega}{2}\sigma_Z + \hbar g_{eff}(a\sigma_+ + a^\dagger\sigma_-)$$

where $g_{eff} = g_c\frac{2t_c}{\Omega}$ is strength of the effective photon-qubit interaction, $\Delta_C = \omega_0 - \omega_R$ is the cavity detuning from the probe field, $\Delta_\Omega = \Omega/\hbar - \omega_R$ is the qubit detuning from the probe field and $\hbar$ the reduced Plank constant. The output field of the cavity

$$\frac{a_{out}}{\alpha} = \frac{-i\sqrt{\kappa_1\kappa_2}}{\Delta_C - i\kappa/2 + g_{eff}\chi}$$

is convoluted with a gaussian distribution of width σ_e to account for charge noise acting on the quantum dot. We simultaneously fit the amplitude $A = |a_{out}/\alpha|^2$ and change in phase $\Delta\phi = -arg(a_{out}/\alpha)$ of each trace to extract t_c as well as the fixed global parameters $\sigma_e \sim 6\,\text{GHz}$ (qubit dephasing), $\gamma \sim 300\,\text{MHz}$ (qubit decoherence) and $g_c/2\pi \sim 150\,\text{MHz}$ (electron photon coupling).

Our results indicate that the system remains far in the dispersive weak coupling regime, due to the strong qubit dephasing rate induced by local charge noise. However, the strength of the measured electron photon interaction is amongst the strongest reported in hybrid systems, it is even comparable to that obtained using high inductance resonators [11] which are much more complex to fabricate, and cannot be used in a strong magnetic environment. We anticipate that the strong coupling regime may be reached in this system by using a higher quality gate dielectric such as hexagonal Boron Nitride, or completely eliminating the gate dielectric by suspending the nanowire above a vacuum gap.
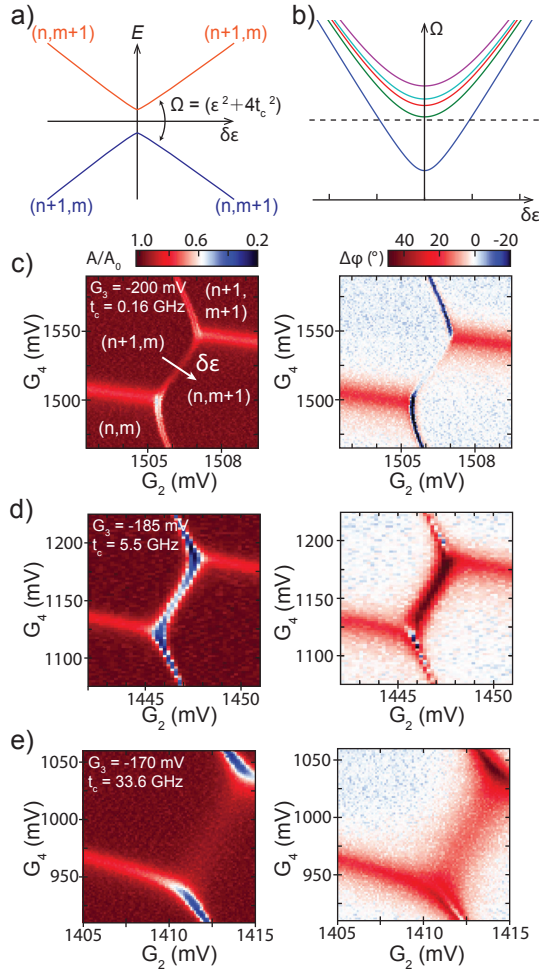
Figure 7.3: Measurements of a single interdot transition at $V_{SD} = 0\,$mV. **a),b)** Close to the transition the energy levels in both dots hybridize into two energy levels Ω with minimal energy spacing determined by the tunnel coupling t_c. **c)–e)** Amplitude and Phase measurements of one transition as the voltage on $g3$ is decreased. t_c values added for each scan are extracted from the fits in Fig 7.4.
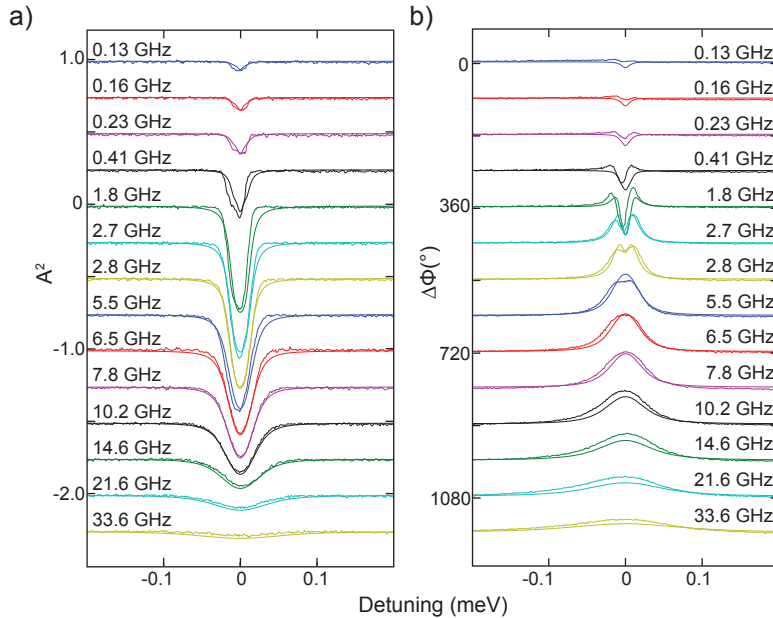
Figure 7.4: Linecuts of the **a)** amplitude and **b)** phase at varying tunnel coupling as function of the double dot level detuning ϵ. Individual traces are offset for clarity and fits to the data are drawn as solid lines.

The exceptionally strong spin-orbit interaction of InSb nanowires would make this system a good candidate to achieve strong spin-photon coupling. Alternatively, minor modifications to the gate pattern in combination with superconducting leads create an attractive system to study light emission from Majorana bound states [28, 29] and a platform for reading out topological qubit devices [17, 18, 22].

REFERENCES

[1] P. K. Day, H. G. LeDuc, B. A. Mazin, A. Vayonakis, and J. Zmuidzinas, "A broadband superconducting detector suitable for use in large arrays," *Nature*, vol. 425, pp. 817–821, oct 2003.

[2] A. Bienfait, J. J. Pla, Y. Kubo, M. Stern, X. Zhou, C. C. Lo, C. D. Weis, T. Schenkel, M. L. W. Thewalt, D. Vion, D. Esteve, B. Julsgaard, K. Moelmer, J. J. L. Morton, and P. Bertet, "Reaching the quantum limit of sensitivity in electron spin resonance," *Nature Nanotechnology*, vol. 11, no. December, p. 10, 2015.

[3] A. Wallraff, D. I. Schuster, A. Blais, L. Frunzio, R.-S. Huang, J. Majer, S. Kumar, S. M. Girvin, and R. J. Schoelkopf, "Strong coupling of a single photon to a superconducting qubit using circuit quantum electrodynamics," *Nature*, vol. 431, no. 7005, pp. 162–167, 2004.

[4] R. Schoelkopf and S. Girvin, "Wiring up quantum systems," *Nature*, vol. 451, no. 7179, pp. 664–669, 2008.

[5] J. Majer, J. Chow, J. Gambetta, J. Koch, B. Johnson, J. Schreier, L. Frunzio, D. Schus-
     ter, A. Houck, A. Wallraff, *et al.*, "Coupling superconducting qubits via a cavity bus,"
     Nature, vol. 449, no. 7161, pp. 443–447, 2007.

[6] K. D. Petersson, L. W. McFaul, M. D. Schroer, M. Jung, J. M. Taylor, A. A. Houck, and
     J. R. Petta, "Circuit quantum electrodynamics with a spin qubit," *Nature*, vol. 490,
     no. 7420, pp. 380–383, 2012.

[7] T. Frey, P. Leek, M. Beck, A. Blais, T. Ihn, K. Ensslin, and A. Wallraff, "Dipole cou-
     pling of a double quantum dot to a microwave resonator," *Physical Review Letters*,
     vol. 108, no. 4, p. 046807, 2012.

[8] M. R. Delbecq, V. Schmitt, F. D. Parmentier, N. Roch, J. J. Viennot, G. Fève, B. Huard,
     C. Mora, A. Cottet, and T. Kontos, "Coupling a quantum dot, fermionic leads, and a
     microwave cavity on a chip," *Phys. Rev. Lett.*, vol. 107, p. 256804, Dec 2011.

[9] V. Ranjan, G. Puebla-Hellmann, M. Jung, T. Hasler, A. Nunnenkamp, M. Muoth,
     C. Hierold, A. Wallraff, and C. Schönenberger, "Clean carbon nanotubes coupled
     to superconducting impedance-matching circuits," *Nature communications*, vol. 6,
     2015.

[10] X. Mi, J. Cady, D. Zajac, P. Deelman, and J. Petta, "Strong coupling of a single electron
     in silicon to a microwave photon," *Science*, p. aal2469, 2016.

[11] A. Stockklauser, P. Scarlino, J. V. Koski, S. Gasparinetti, C. K. Andersen, C. Reichl,
     W. Wegscheider, T. Ihn, K. Ensslin, and A. Wallraff, "Strong coupling cavity qed with
     gate-defined double quantum dots enabled by a high impedance resonator," *Phys.
     Rev. X*, vol. 7, p. 011030, Mar 2017.

[12] N. Samkharadze, A. Bruno, P. Scarlino, G. Zheng, D. P. DiVincenzo, L. DiCarlo, and
     L. M. K. Vandersypen, "High-Kinetic-Inductance Superconducting Nanowire Res-
     onators for Circuit QED in a Magnetic Field," *Physical Review Applied*, vol. 5, no. 4,
     p. 044004, 2016.

[13] J. Kammhuber, M. Cassidy, F. Pei, M. Nowak, A. Vuik, D. Car, S. Plissard, E. Bakkers,
     M. Wimmer, and L. Kouwenhoven, "Conductance through a helical state in an InSb
     nanowire," *arxiv 1701.06878*.

[14] S. Heedt, N. Traverso Ziani, F. Crepin, W. Prost, S. Trellenkamp, J. Schubert, D. Grutz-
     macher, B. Trauzettel, and T. Schapers, "Signatures of interaction-induced helical
     gaps in nanowire quantum point contacts," *Nat Phys*, vol. advance online publica-
     tion, mar 2017.

[15] W. Chang, S. Albrecht, T. Jespersen, F. Kuemmeth, P. Krogstrup, J. Nygård, and
     C. Marcus, "Hard gap in epitaxial semiconductor–superconductor nanowires," *Nat
     Nano*, vol. 10, pp. 232–236, mar 2015.

[16] Ö. Gül, H. Zhang, F. K. de Vries, J. van Veen, K. Zuo, V. Mourik, S. Conesa-Boj, M. P.
     Nowak, D. J. van Woerkom, M. Quintero-Pérez, M. C. Cassidy, A. Geresdi, S. Kölling,

D. Car, S. R. Plissard, E. P. A. M. Bakkers, and L. P. Kouwenhoven, "Hard superconducting gap in InSb nanowires," 2017.

[17] T. Karzig, C. Knapp, R. Lutchyn, P. Bonderson, M. Hastings, C. Nayak, J. Alicea, K. Flensberg, S. Plugge, Y. Oreg, C. Marcus, and M. H. Freedman, "Scalable Designs for Quasiparticle-Poisoning-Protected Topological Quantum Computation with Majorana Zero Modes," pp. 1–26, 2016.

[18] S. Plugge, A. Rasmussen, R. Egger, and K. Flensberg, "Majorana box qubits," *New Journal of Physics*, vol. 19, no. 1, p. 12001, 2017.

[19] A. Cottet, T. Kontos, and B. Dou\ifmmode \mbox\cc\else ç\fiot, "Squeezing light with Majorana fermions," *Phys. Rev. B*, vol. 88, p. 195415, nov 2013.

[20] M. C. Dartiailh, T. Kontos, B. Dou\ifmmode \mbox\cc\else ç\fiot, and A. Cottet, "Direct Cavity Detection of Majorana Pairs," *Phys. Rev. Lett.*, vol. 118, p. 126803, mar 2017.

[21] C. Ohm and F. Hassler, "Microwave readout of Majorana qubits," *Phys. Rev. B*, vol. 91, p. 85406, feb 2015.

[22] T. Hyart, B. van Heck, I. C. Fulga, M. Burrello, A. R. Akhmerov, and C. W. J. Beenakker, "Flux-controlled quantum computation with Majorana fermions," *Phys. Rev. B*, vol. 88, p. 35121, jul 2013.

[23] F. Chen, A. J. Sirois, R. W. Simmonds, and A. Rimberg, "Introduction of a dc bias into a high-q superconducting microwave cavity," *Applied Physics Letters*, vol. 98, no. 13, p. 132509, 2011.

[24] X. Mi, J. Cady, D. Zajac, J. Stehlik, L. Edge, and J. Petta, "Circuit quantum electrodynamics architecture for gate-defined quantum dots in silicon," *arXiv preprint arXiv:1610.05571*, 2016.

[25] K. Flöhr, M. Liebmann, K. Sladek, H. Y. Günel, R. Frielinghaus, F. Haas, C. Meyer, H. Hardtdegen, T. Schäpers, D. Grützmacher, and M. Morgenstern, "Manipulating inas nanowires with submicrometer precision," *Rev. Sci. Instrum.*, vol. 82, no. 11, p. 113705, 2011.

[26] W. G. Van der Wiel, S. De Franceschi, J. M. Elzerman, T. Fujisawa, S. Tarucha, and L. P. Kouwenhoven, "Electron transport through double quantum dots," *Reviews of Modern Physics*, vol. 75, no. 1, p. 1, 2002.

[27] R. Wang, R. S. Deacon, D. Car, E. Bakkers, and K. Ishibashi, "Insb nanowire double quantum dots coupled to a superconducting microwave cavity," *Applied Physics Letters*, vol. 108, no. 20, p. 203502, 2016.

[28] M. Dartiailh, T. Kontos, B. Douçot, and A. Cottet, "Direct cavity detection of majorana pairs," *arXiv preprint arXiv:1702.01637*, 2017.

[29] C. Ohm and F. Hassler, "Majorana fermions coupled to electromagnetic radiation," *New Journal of Physics*, vol. 16, no. 1, p. 015009, 2014.

8

DEMONSTRATION OF AN AC JOSEPHSON JUNCTION LASER

M. C. Cassidy, A. Bruno, S. Rubbert, M. Irfan, J. Kammhuber,
R. N. Schouten, A. R. Akhmerov and L. P. Kouwenhoven

Superconducting electronic devices have reemerged as contenders for both classical and quantum computing due to their fast operation speeds, low dissipation, and long coherence times. An ultimate demonstration of coherence is lasing. We use one of the fundamental aspects of superconductivity, the ac Josephson effect, to demonstrate a laser made from a Josephson junction strongly coupled to a multimode superconducting cavity. A dc voltage bias applied across the junction provides a source of microwave photons, and the circuit's nonlinearity allows for efficient down-conversion of higher-order Josephson frequencies to the cavity's fundamental mode. The simple fabrication and operation allows for easy integration with a range of quantum devices, allowing for efficient on-chip generation of coherent microwave photons at low temperatures.

8.1. Introduction

Josephson junctions are natural voltage to frequency converters via the AC Josephson effect. For a Josephson junction without an applied DC voltage bias, Cooper pairs tunnel coherently from one superconducting condensate to the other, resulting in a supercurrent flowing without dissipation. However, for a nonzero DC voltage bias (V_b) less than the superconducting energy gap, transport is prohibited unless the excess energy ($hf = 2eV_b$, where h is Planck's constant, f is frequency, and $2e$ is the charge of the Cooper par) can be dissipated into the environment. The analogy between a single Josephson junction and a two-level atom was first proposed theoretically in the 1970's [1]. The voltage difference across the junction provides the two energy levels for the Cooper pairs, and spontaneous emission as well as stimulated emission and absorption were predicted to occur [1, 2]. Emission from Josephson junctions into low-quality cavities (either constructed artificially or intrinsic to the junction's environment) in the so-called weak-coupling regime has been studied extensively[3–8]. However, because the total output power of these systems is low, coherent radiation has not been directly demonstrated. By using a tightly confined cavity mode coherent interaction of a single Josephson junction and the cavity can be achieved. Lasing results when the transfer rate of Cooper pairs across the junction, Γ_{CP}, exceeds the cavity decay rate, κ, of the microwave photons (Fig. 8.1a)). Photon emission from alternative single emitters coupled to superconducting resonators has been the subject of several recent investigations [8–10].

We demonstrate lasing in the microwave frequency domain from a dc voltage-biased Josephson junction strongly coupled to a superconducting coplanar waveguide resonator. Our device obeys several properties present in conventional optical lasers, including injection locking, and frequency comb generation, with an injection locked linewidth of $\lesssim 1\,\text{Hz}$, which exceeds performance of other state of the art laser systems. The laser consists of a half-wave coplanar waveguide (CPW) resonator with resonant frequency $f_0 \approx 5.6\,\text{GHz}$ made from thin (20 nm) NbTiN (Fig. 8.1, b) and c)). A DC superconducting quantum interference device (SQUID), located at the electric field anti-node of the cavity, effectively acts as a single junction with Josephson energy tunable via the magnetic flux ϕ threading its loop: $E_J = E_{J0}|\cos(\pi\phi/\phi_0)|$, where $E_{J0} \sim 78\,\text{GHz}$, and $\phi_0 = h/2e$ the superconducting flux quantum. One side of the SQUID is tied to the central conductor of the CPW, with the other end attached directly to the ground plane to enhance the coupling to the cavity. An on-chip inductor positioned at the electric field node of the cavity allows for a stable DC voltage bias to be applied across the SQUID [11]. Coupling capacitors at each end of the cavity provide an input and output for microwave photons at a rate of κ_{in} and κ_{out}, respectively, as in standard circuit-QED experiments [12]. The device is mounted in a dilution refrigerator with base temperature $T = 15\,\text{mK}$, and the magnetic flux through the SQUID is tuned via a superconducting vector magnet (See further details in chapter 8.5).

8.2. Microwave Emission and Lasing

We first examine the response of the device without applying any microwave power to the cavity input. At the output, we measure the power spectral density, *S(f)*, of the emit-
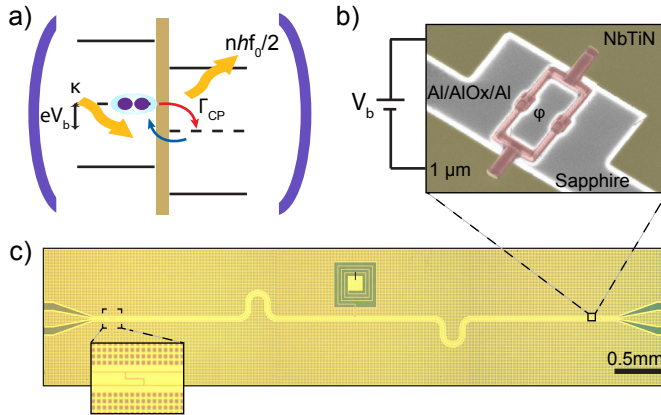
Figure 8.1: An ac Josephson laser. **a)** Illustration of the operating principle of the device. A DC voltage bias V_b applied across the Josephson junction results in photon emission into the cavity when twice the bias voltage is equal to a multiple of the cavity frequency. If the emission rate Γ_{CP} into the cavity exceed the cavity lifetime κ, these photons can be reabsorbed and reemitted by the junction, a process akin to stimulated emission in atomic laser systems. Dashed lines depict the superconducting condensate; solid lines represent the superconducting gap, Δ. **b)** Scanning electron microscope (false color) and **c** optical microscopy images of the device. A DC SQUID (red), acting as a tunable Josephson junction, is strongly coupled to the electric field antinode of a half-wave superconducting coplanar waveguide resonator (yellow).

ted microwave radiation as a function of voltage bias V_b. Simultaneously, we record the corresponding current flowing through the device, $I_D = 2e\Gamma_{CP}$. The coupling between a dc voltage-biased Josephson junction and a cavity $\lambda = E_J/\phi_0^2 L$ is set by the junction's Josephson energy, E_J, together with the cavity inductance, $L = 1/C\omega_0^2$, where C is the cavity capacitance and $\omega_0 = 2\pi f_0$ (chapter 8.5). When the device is configured in the weak Josephson coupling regime ($\lambda \ll 1$, Fig. 8.2a)), by tuning the external flux close to $\phi = \phi_0$, a series of discrete microwave emission peaks are visible at bias voltages corresponding to n multiples of the bare cavity resonance V_r: $V_b = nV_r = nhf_0/2e \approx n \times 11.62\,\mu$V. At each of these emission bursts, we observe an increase in dc current (Fig. 8.2b)), a measure of inelastic Cooper pair transport across the Josephson junction. In this weak coupling regime, both the current and microwave emission are dominated by linear effects, with the rate of photon emission determined by the environmental impedance [7, 13] (Fig. 8.2c)).

We increase the microwave emission by increasing E_J via the applied flux, to the extent that the junction and cavity become strongly coupled and the system transitions to nonlinear behavior ($\lambda \gg 1$) [14]. In contrast to the discrete emission peaks seen at low Josephson energy, the emission now shifts to higher bias voltages, persisting continuously even when the voltage bias is detuned from resonance (Fig. 8.2d)), and is accompanied by a constant flow of Cooper pairs tunneling across the junction (Fig. 8.2e)). The emission peaks at voltages corresponding to multiples of the cavity resonance, exhibiting bifurcations common to non-linear systems under strong driving. Between these points of instability, the emission linewidth narrows to $\sim 22\,$kHz, well below the bare cavity linewidth of $\sim 5\,$MHz (see chapter 8.5), corresponding to a phase coherence time
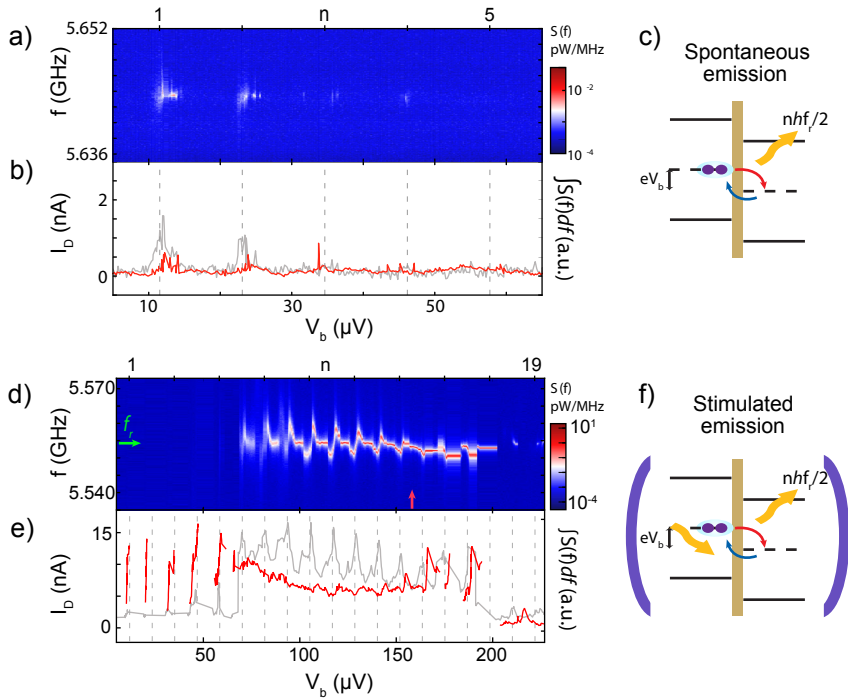
Figure 8.2: Microwave emission from the Josephson laser. **a)** Power spectrum of the emitted radiation $S(f)$, **b)** integrated emission (grey) and corresponding current flowing through the Josephson junction (red) as a function of V_b when the coupling strength $\lambda \ll 1$. **c)** Cooper pair transport can occur at discrete voltage biases corresponding to multiples of the cavity resonance frequency f_0, resulting in spontaneous photon emission into the cavity. When $\lambda > 1$, the emission **d)** and corresponding current flow **e)** become continuous across a range of bias values, peaking at bias voltages corresponding to multiples of the cavity frequency. **f)** Cooper pair transport is accompanied by the release of multiple photons into the cavity at the fundamental frequency, as well as emission of photons into the higher-order resonator modes, resulting in a cavity photon occupancy large enough for stimulated emission to occur.

$\tau_c = 1/\pi\nabla f_0 = 15\,\mu s$. The enhancement in emission originates from stimulated emission, as a larger photon number in the cavity increases the probability of reabsorption and coherent reemission by the junction. Notably, the emission power increases here by more than three orders of magnitude, while the average dc power input, $P_{in} = V_b I_D$, varies by only a factor of three. By comparing P_{in} with the integrated output power, we estimate a power conversion efficiency $P_{out}/P_{in} > 0.3$ (see chapter 8.5), several orders of magnitude greater than achieved for single junctions without coupling to a cavity [4] and comparable only to arrays containing several hundred synchronized junctions [5]. Similar power conversion efficiencies have been seen in other strongly coupled single emitter-cavity systems [8, 9]. Application of a larger perpendicular magnetic field adjusts the cavity frequency, directly tuning the laser emission frequency by more than 50 MHz (see chapter 8.5).

To understand the strong emission characteristics, we numerically simulate the time evolution of the coupled resonator-Josephson junction circuit for increasing E_J (see chapter 8.5). If the cavity only supports a single mode, the emission power at $n = 1$ grows with increasing E_J; however there is only weak emission for bias voltages corresponding to $n > 1$. Higher-order cavity modes allow for direct emission of higher frequency photons that can be down-converted to the fundamental cavity frequency via the nonlinearity of the Josephson junction. Simulations for $n = 20$ modes show that for weak coupling ($\lambda \ll 1$), disconnected resonant peaks are visible in the response, in agreement with the experimental data (Fig. 8.2a)). Only when combining strong coupling ($\lambda \gg 1$) with the presence of many higher-order modes do we find a continuous narrow emission line as observed experimentally (Fig. 8.2b)). Simulations show that this behavior persists even if the mode spacing is inhomogeneous, as under strong driving the presence of harmonics and subharmonics for each mode means that down-conversion to the frequency of the fundamental mode of the cavity is always possible (see chapter 8.5).

To directly confirm lasing, we measure the emission statistics in the high-Josephson coupling regime at $V_b = 192.5\,\mu V$. The emitted signal is mixed with an external local oscillator and the resulting quadrature components digitized with a fast acquisition card (Fig 8.3a)). A time series of the demodulated free-running laser emission over a period of 100 μs (Fig. 8.3b)) shows a clear sinusoidal behavior, never entering a sub-threshold state.

This is in contrast to recently demonstrated lasers made from quantum dots [10] or superconducting charge qubits [8, 15], which are strongly affected by charge noise. Instead, we note that the coherence of our system is disrupted by occasional phase slips (Fig. 8.3, inset). To quantify the effect of these phase slips, we plot the autocorrelation $g^{(1)}$ (Fig. 8.33c)) and extract a phase coherence time of 14 μs, in good agreement with the value extracted from the free running linewidth.

To confirm coherence over longer time scales, we plot the in-phase and quadrature components of the downconverted signal from 5×10^5 samples on a two-dimensional histogram (Fig. 8.3d)). The donut shape of the histogram confirms lasing, with the radius $A = \sqrt{\bar{N}} = 172$ (where $\bar{N}$ is the average photon number) representing the average coherent amplitude of the system, whereas the finite width $\sigma_l = \sqrt{(2\delta A^2 + N_{noise})/2} = 6.89$ is a result of amplitude fluctuations in the cavity emission $\delta A = 2.66$ broadened by the thermal noise in the amplifier chain, N_{noise}. When the device is not lasing ($V_b = 18\,\mu V$ in

8
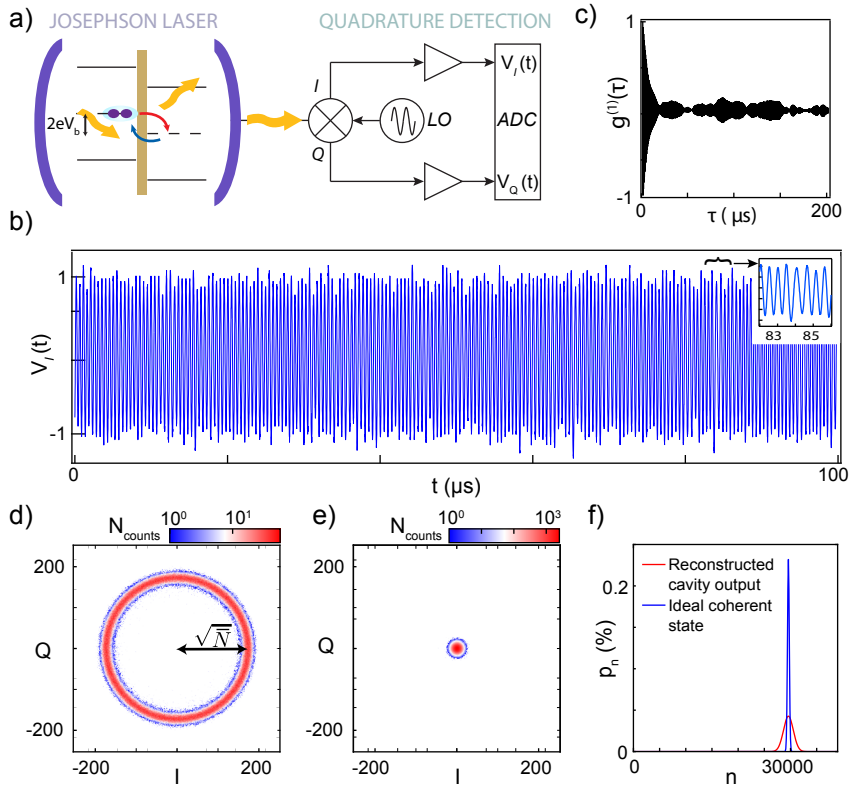
Figure 8.3: Coherence and emission statistics of the free running Josephson laser. **a)** Real-time evaluation of the emission statistics of the free-running Josephson laser is performed with a heterodyne measurement setup. **b)** Time series $V_I(t)$ of the emission over $100\,\mu s$ (Inset) Small phase slips in the emission result in loss of coherence, resulting in an artificially broadened emission line. **c)** Autocorrelation $g^{(1)}(\tau)$ of the time series shows a phase coherence of $\sim 14\,\mu s$. **d)** The IQ histogram acquired above the lasing threshold shows a clear donut shape, a characteristic of coherent emission. **e)** The IQ histogram obtained when the device is not emitting shows a Gaussian peak centered at zero, corresponding to thermal emission. **f)** The reconstructed photon number distribution p_n at the cavity output (red) is well fit by a single Gaussian peak centered around an average photon number $\bar{N} \approx 29\,600$, slightly broader than what expected for and ideal coherent source (blue).

Fig 8.2a)), we record a Gaussian peak of width $\sigma_{th} = \sqrt{N_{noise}/2} = 6.36$, corresponding to thermal emission (Fig 8.3e)).

To extract the photon number distribution at the output of the cavity, the contribution of thermal fluctuations due to the amplifier chain in Fig. 8.3e) is subtracted from the emission data in Fig. 8.3d). The extracted distribution takes the form $p_n \propto \exp\left[-(n-\bar{N})^2/(2\bar{N}(1+4\delta A^2))\right]$ and is centered $\bar{N} \approx 29\,600$, (red curve in Fig 8.3f)). In contrast, a perfectly coherent source is expected to show a shot noise limited Poissonian distribution, which tends to a Gaussian distribution of the form $p_n \propto \exp\left[-(n-\bar{N})^2/2\bar{N}\right]$ in the limit of large $\bar{N}$ (blue curve in Fig 8.3f)). The residual fluctuations in the cavity amplitude are most probably due to E_J fluctuations which change the instantaneous photon emission rate into the cavity.

8.3. INJECTION LOCKING

Emission linewidth is a key figure of merit for lasers. A narrow linewidth implies high frequency stability and resolution, which is important for a range of technologies including spectroscopy, imaging and sensing application. One technique commonly used for stabilizing lasers is injection locking [16, 17] (Fig. 8.4, a) and b)). The injection of a seed tone of frequency f_{inj} into the cavity generates stimulated emission in the Josephson junction at this injected frequency, narrowing the emission spectrum. Figure 8.4c) shows $S(f)$ as a function of input power P_{inj} for an injected signal with frequency $f_{inj} = 5.651\,\text{GHz}$, well within the emission bandwidth of the free running source [linecuts at $P_{inj} = -127\,\text{dBm}$ and $P_{inj} = -90\,\text{dBm}$ (Fig. 8.4d)]. For very low input power, $P_{inj} < -140\,\text{dBm}$, the average photon occupation of the cavity is $\bar{N} < 1$, and the device remains unaffected by the input tone. Once the photon occupancy exceeds $\bar{N} \approx 1$, the injected microwave photons drive stimulated emission in the device, causing the emission linewidth to narrow with increasing power, reaching an ultimate (measurement-limited) linewidth of $1\,\text{Hz}$ (Fig. 8.4d), inset), which is more than three orders of magnitude narrower than the free-running emission peak and approaches the Schawlow-Tones limit of ~ 15 mHz (see chapter 8.5). In this regime, our device acts as a quantum limited amplifier, similar to other Josephson junction based amplifiers [18, 19]; however, no additional microwave pump tone is required to provide amplification. Figure 8.4e) shows the effect when the input tone is applied at a frequency $f_{inj} = 5.655\,\text{GHz}$, outside the cavity bandwidth. At low input powers the emission remains unaffected, similar to the on-resonant case shown earlier. When $P_{inj} > -130\,\text{dBm}$, distortion side-bands appear at both positive and negative frequencies, and the free running emission peak is pulled towards the input tone, eventually being locked when $P_{inj} > -85\,\text{dBm}$ [linecuts at $P_{inj} = -127\,\text{dBm}$ and $P_{inj} = -90\,\text{dBm}$ (Fig 8.4f)]. The positions and intensities of these emission sidebands are well described by the Adler theory for the synchronization of coupled oscillators [20], similar to what has been observed for both traditional and exotic laser systems [16, 17].

The frequency range over which the device can be injection locked is strongly dependent on the injected power. Figure 8.4g) shows the $S(f)$ as a function of f_{inj} at an input power $P_{inj} = -90\,\text{dBm}$, with an injection locking range Δf of almost 5 MHz. Here, the distortion sidebands span more than 100 MHz (see chapter 8.5). Measurements of Δf as a function of P_{inj} are shown in the inset of Fig. 8.4g). Adler's theory predicts that the injection locking range should fit a square-root relation $\Delta f = \alpha\sqrt{P_{inj}}$, with a measured
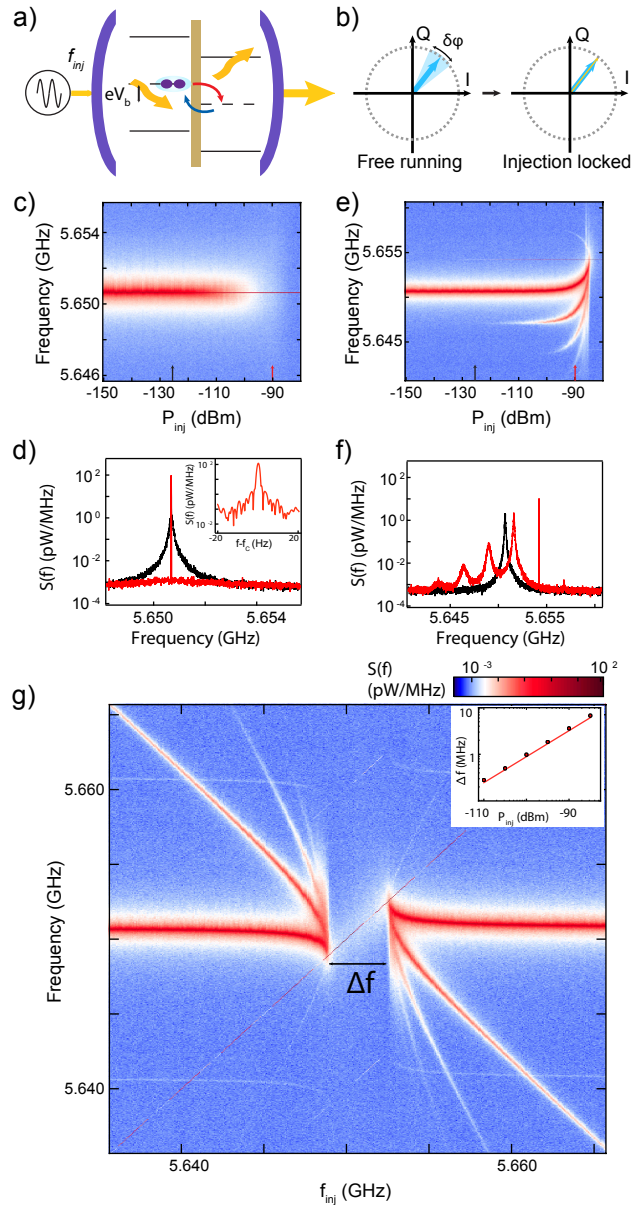
Figure 8.4: Injection locking of the Josephson laser. **a)** Schematic illustration and **b)**, phasor diagram of the injection-locking process. Injection of a low-power input tone into the cavity drives stimulated emission of photons synchronous with the input tone, reducing the phase fluctuations $\delta\phi$ experienced in the free running mode. **c)** $S(f)$ as a function of input power (P_{inj}) for an on-resonance input tone. **d)** Linecuts of c) at $P_{inj} = -90\,$dBm (red) and $-127\,$dBm (black). (Inset) The linewidth of the injection-locked laser is $\lesssim 1\,$Hz **e)** $S(f)$ as a function of P_{inj} for an off-resonance input tone, demonstrating frequency pulling. **f)** Linecuts of e at $P_{inj} = -90\,$dBm (red) and $-127\,$dBm (black). **g)** $S(f)$ at fixed input power $P_{inj} = -90\,$dBm as the frequency of the input tone f_{inj} is swept. For probe frequencies f_{inj} in the range Δf, the laser emission frequency locks to the frequency of the input signal. (Inset) The bandwidth of frequency locking Δf scales proportionally with the square root of the input power, in agreement with the Adler theory of coupled oscillators.

prefactor $\alpha = 3.66(193)\,\text{MHz}/\sqrt{\text{W}}$.

8.4. DISCUSSION

We can also use the device to generate a microwave frequency comb, an alternative to recently demonstrated four-wave-mixing methods [21] The time-frequency duality implies that a voltage modulation applied to the junction will create a comb in the frequency domain [22]. By configuring the device in the on-resonance injection-locked regime ($P_{inj} = -110\,\text{dBm}$ in Fig. 8.4c) and applying a small ac excitation frequency $f_{\text{mod}} = 111\,\text{Hz}$ to the dc bias (see chapter 8.5), we generate a comb around the central pump tone, with frequency separation 111 Hz. The total width of the comb is set by the amplitude of the modulation, as well as the input power of the injection lock.

Our results conclusively demonstrate lasing from a dc-biased Josephson junction in the strong coupling regime. Analysis of the output emission statistics shows 15 μs of phase coherence, with no sub-threshold behavior. The Josephson junction laser does not suffer from charge-noise-induced linewidth broadening inherent to semiconductor gain media [10, 23], and thus reaches an injection locked linewidth of < 1 Hz. The device produces frequency tunability over 50 MHz via direct tuning of the cavity frequency and over > 100 MHz through the generation of injection-locking sidebands. Additional frequency control may be achieved by using a broadband tunable resonator [24], and pulse control may be provided with a tunable coupler. The phase coherence is likely limited by fluctuations in E_J, either due to $1/f$-dependent flux noise from magnetic impurities[25], or due to defects within the Josephson junction, as well as thermal fluctuations in the biasing circuit that vary V_b. We anticipate that improvements to the magnetic shielding and passivating magnetic fluctuators, together with using a cryogenically generated voltage bias will further stabilize the emission. In this case the device would perform at the quantum limit, with a linewidth that would then only be limited by residual fluctuations in the photon number in the cavity. Along with the high efficiency, the possibility of engineering the electromagnetic environment and guiding the emitted microwaves on demand lends this system to a versatile cryogenic source for propagating microwave radiation.

8.5. SUPPLEMENTARY MATERIALS

8.5.1. DEVICE DESIGN AND FABRICATION

A 20nm NbTiN film was reactively sputtered on a cleaned 2" sapphire substrate (C plane, 350 μm) in a N_2/Ar environment from a NbTi target (65:35 Nb:Ti, 99.95% purity). An SF_6/O_2 dry etch was then used to define the CPW resonator, coupling capacitors and spiral inductor. The Al/AlOx/Al SQUID (Al thicknesses 35 nm/65 nm) was then formed using standard double angle evaporation and lift off techniques. To ensure good electrical contact between the Al and NbTiN layers, the sample was exposed to a short HF wet etch (30 s, 21:1 H_2O:Buffered HF) to remove residual oxides and resist residue from the surface of the NbTiN film prior to the Al double angle evaporation. The junction sizes were ∼ 180 nm × 150 nm, and had a total normal state resistance of $R_D = 2.4\,\text{k}\Omega$, with an estimated junction capacitance $C_J = 2\,\text{fF}$ per junction. The device is therefore in the strongly underdamped regime ($\beta_C = 2eI_cR_D^2C_J/\hbar \gg 1$).

The emission frequency of the laser is set by the resonant frequency of the bare cavity $\omega_0 = 2\pi f_0 = 1/\sqrt{LC}$, which is determined by its geometric design as well as the kinetic inductance of the thin NbTiN film ($L = L_g + L_k$). For our geometry, which consists of a 30 μm wide central conductor of length $\lambda/2 = 5650$ μm, with 1.5 μm spacings to the ground plane, with $C \sim 1.4$ pF and $L_g \sim 1.2$ nH determined using elliptical integrals [26], while $L_k \sim 4.2$ nH is determined experimentally for the film from characterization resonators. Based on this we calculate a kinetic inductance fraction $\alpha = 0.78$. The total impedance $Z(\omega)$ seen by the tunneling Cooper pairs consists of the combination of the impedance of the Josephson junction and that of the parallel LC resonance with finite Q factor. As the capacitance of the resonator is much greater than the junction ($C \gg C_J$), the impedance is dominated by that of the resonator. The capacitance of each of the coupling capacitors was simulated to be 11.1 fF, which results in a calculated coupling quality factor of $Q_c \sim 10^4$, giving $\kappa_{in} = \kappa_{out} = 0.27$ MHz. The intrinsic quality factor of the resonator without the SQUID was much higher. Bare resonators fabricated on the same film showed $Q_i > 10^5$. However, the presence of the SQUID provides an additional damping mechanism due to the finite resistance, reducing the loaded quality factor $Q_l^{-1} = Q_c^{-1} + Q_i^{-1} + Q_r^{-1} \sim 1200$, resulting in a total cavity decay rate $\kappa = 4.7$ MHz.

8.5.2. MEASUREMENT CIRCUIT

A complete circuit showing both the low frequency and microwave measurement schemes is shown in Figure 8.5. The device was mounted on the mixing chamber of a dilution refrigerator inside a light-tight radiation shield painted with Aeroglaze Z306, with an additional tight-fitting lid encasing the PCB to suppress unwanted environmental modes. The components marked in the dashed box are located on the PCB close to the sample in order to minimize parasitic capacitances and additional resonances in the circuit.

LOW NOISE BIASING SCHEME

We adopt a similar approach to Refs [7, 8] for the design of the low noise biasing scheme to measure the tunneling current and provide a stable voltage bias to the device. The bias voltage is provided by an on-chip voltage divider circuit consisting of a 100 Ω shunt resistor and 1 kΩ resistor in series with the device which is driven by a low noise optically isolated DC current source I_{BIAS} located at room temperature. The current through the device I_D is then measured via the voltage drop across the 1 kΩ reference resistor. Calibration of the resistors at low temperature was performed by measuring the circuit with the SQUID flux biased to a point of minimum Josephson coupling. All data presented has the applied bias voltage corrected for the voltage drop over the 1 kΩ resistor according to $V_b = 100 I_{BIAS} - 1100 I_D$. Additional filtering for the circuit is provided by the two 100 μF chip capacitors, which reduces the voltage fluctuations due to thermal noise across the 1 kΩ resistor to approximately 40 pV, reducing the corresponding noise in the frequency domain, $\delta f = \frac{2e\delta V_n}{h}$, from several MHz to ~ 30 kHz, which is well within the bare linewidth of the resonator. Additionally, all low frequency lines are heavily filtered outside the PCB with multi-pole RC and PI low pass filters located on the mixing chamber of the dilution refrigerator that filter in the range 80 kHz – 80 GHz.
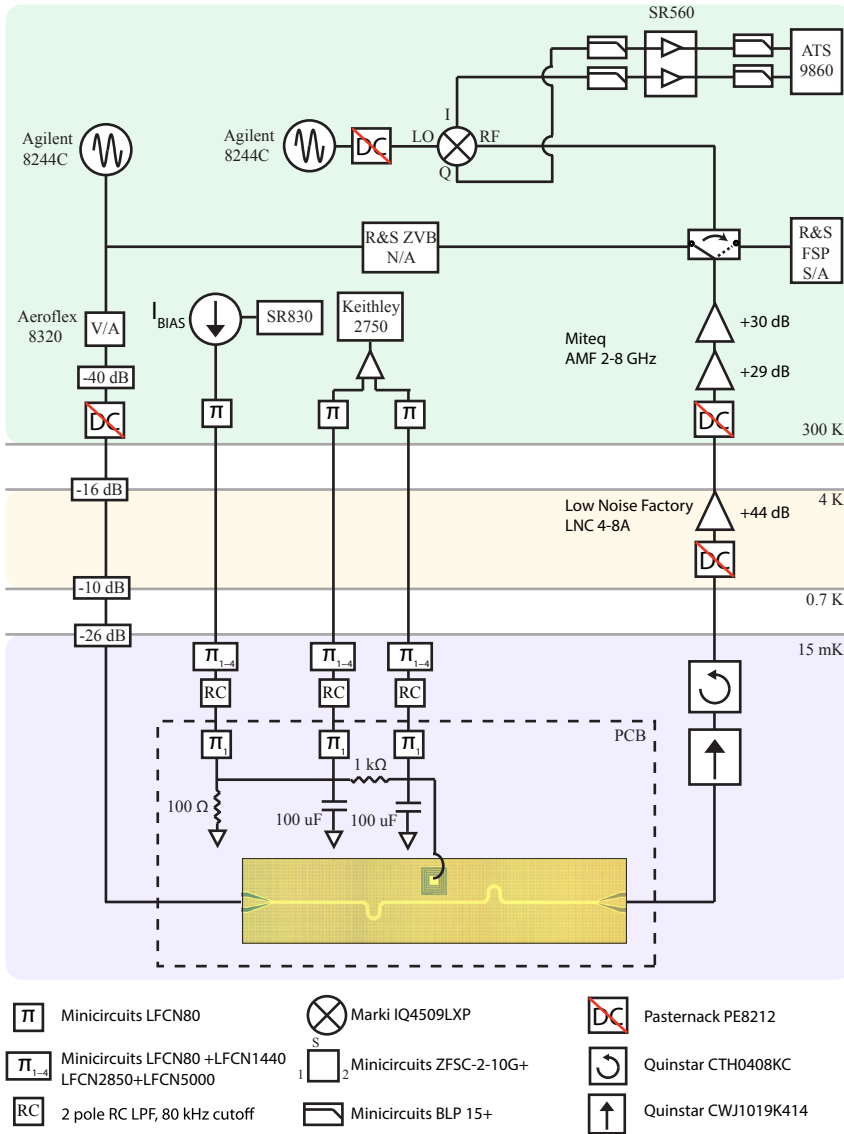
Figure 8.5: Measurement circuit schematic.

MICROWAVE MEASUREMENTS

Measurements of the free running laser emission shown in Fig. 8.2 and Fig. 8.7-8.9 of the Supplementary Information were recorded with a Rohde and Schwarz FSP spectrum analyzer with a resolution bandwidth of 10 kHz, well below the bare emission linewidth. During these measurements the input line to the cavity was terminated with a 50 Ω impedance at the top of the fridge. This together with the significant cold attenuation inline assures that the thermal contribution of photons to the cavity is negligible.

Measurements of the emission statistics shown in Fig. 8.3 were performed with a standard heterodyne demodulation setup. Briefly, the amplified output of the free running laser emission was mixed with a local oscillator signal down to an intermediate frequency ($f_{IF} = 2$ MHz in Fig. 8.3 b)-c), $f_{IF} = 12.5$ MHz in Fig. 8.3 d)-f)). The individual I and Q components were then filtered, further amplified, and then digitized using a fast acquisition card (Alazar 9850). The digitized signal was Fourier transformed in software before being stored. The input to the cavity was terminated with a 50 Ω impedance during these measurements. In the injection locking measurements in Fig. 8.4 and Fig. 8.14, a microwave tone was applied at the input of the cavity, and the response again recorded with the spectrum analyzer. In Fig 8.4 the resolution bandwidth was 3 kHz, while in Fig. 8.14 the resolution bandwidth was 10 Hz. During these measurements, the input power was adjusted with an inline variable attenuator (Aeroflex 8320). The injection-locked linewidth measurements in Fig 8.11 were carried out with a Rohde and Schwarz FSV spectrum analyzer with a resolution bandwidth of 1 Hz and applied power $P_{inj} = -113$ dBm. We believe that this linewidth is still measurement limited. The bare cavity linewidth in Fig 8.10 was recorded by measuring the cavity transmission using a Rohde and Schwartz ZVB network analyzer and applied power $P_{inj} = -140$ dBm.

SHOT NOISE CALIBRATION OF THE AMPLIFIER CHAIN

To calibrate the amplifier chain, we measure the shot noise emitted from the device when it is biased in the resistive regime, well above the superconducting gap $V_b > 2\Delta \sim 400\mu$eV [27]. The shot noise current spectral density in this regime is given by $S_I = eI_D = \frac{eV_b}{R_D}$. The measured shot noise is perturbed by the presence of the cavity, as well as the coupling capacitors. To account for this, we model the cavity as a parallel LCR circuit coupled to a dissipative resistance R_D and assume the cavity is driven by the shot noise current I_D. The spectral density of the voltage noise at the cavity output is $S_V(f) = \frac{\omega}{C} \frac{S_I}{i(\omega_0^2 - \omega^2)^2 + (\omega\omega_0/Q_{l'})^2}$. Here $Q_{l'} = \omega_0 R_D C \approx 35$ is the measured loaded quality factor taking into account the additional dissipative resistance in the high bias regime. The voltage noise is given by integrating over the cavity resonance, $V_n^2 = \int_f S_V(f) df = eI_D Q_{l'}/4\omega_0 C^2$. The noise power at the output of the cavity is given by $P_C = \kappa_{out} E = \kappa_{out} C V_n^2$, where $\kappa_{out} = \kappa_{tot}/2$ is the decay rate of photons out of the output port of the cavity. This noise is then amplified by the amplifier chain with gain G to give the noise power $P_N = GP_C = G\frac{eI_D Q_{l'}}{2Q_c C}$ after amplification. Here $Q_c = \omega_0/\kappa_{tot}$ is the coupling quality factor of the circuit. The measured noise power P_N as a function of I_D integrated across a resolution bandwidth of 10 MHz is shown in Fig. 8.6. A linear fit to this data gives $G = (P_N/P_C) \approx 89$ dB.
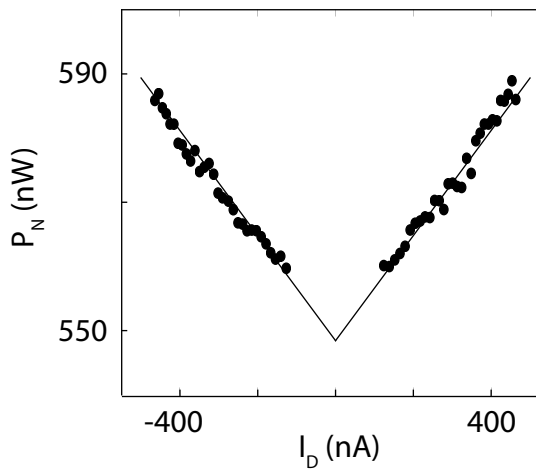
Figure 8.6: Shot noise characterization of the microwave setup. The noise power P_N emitted from the device is measured when it is biased in the resistive regime, well above the superconducting gap $V_b > 2\Delta \sim 400\mu eV$. A linear fit to this data gives $G = (P_N/P_C) \approx 89\,dB$.

8

8.5.3. EXTENDED DATA

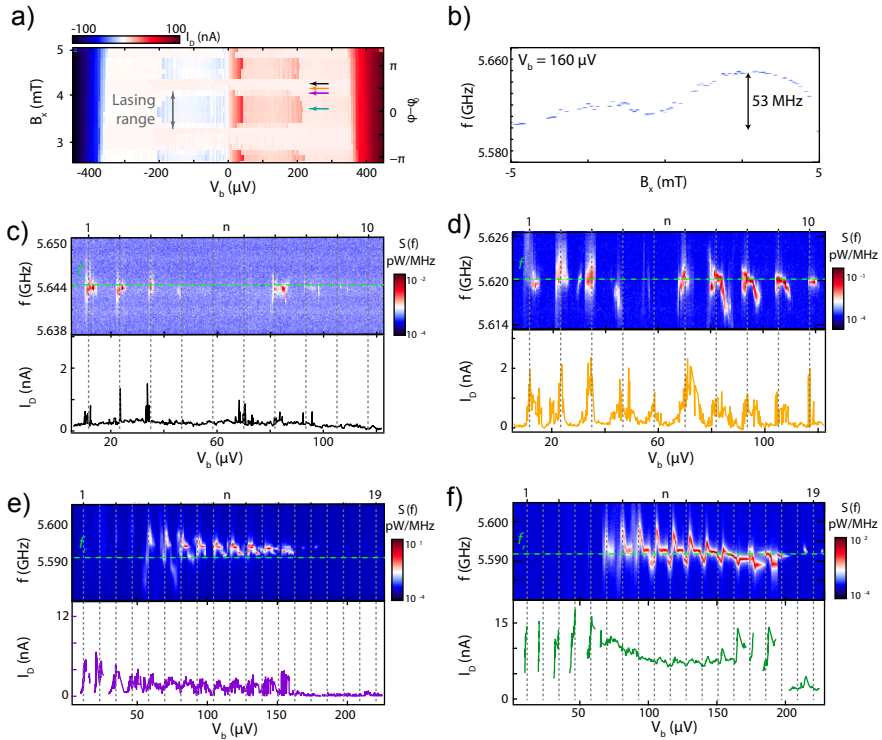**FLUX TUNING OF THE JOSEPHSON COUPLING AND EMISSION FREQUENCY**

Figure 8.7: Flux tuning of the Josephson coupling and emission frequency. **a)** The Josephson coupling strength is tuned by the application of a perpendicular magnetic field through the SQUID loop. The supercurrent and subgap emission features show a characteristic SQUID oscillation with periodicity ~ 1 mT, which is in good agreement for a SQUID of area ~ 1.5 μm^2. The arrows show the approximate values for the magnetic flux tuning for the data shown in (c – f). **b)** Application of a larger perpendicular magnetic field shifts the resonant frequency of the cavity, tuning the laser emission over a frequency range of more than 50 MHz. Shown is the power spectral density $S(f)$ as a function of perpendicular magnetic field B_x at fixed voltage bias $V_b =$ 160 μV. In a) and b), the applied external magnetic field has a small offset from the true magnetic field due to hysteresis in the superconducting magnet and residual magnetic fields in the setup. **c) – f)** Power spectral density $S(f)$ of the emission for increasing Josephson couplings corresponding to the location of arrows in a). By tuning the applied magnetic flux, the device evolves from weak coupling between the SQUID and the cavity to being strongly coupling, where significant line narrowing takes place. The current spikes present at low bias voltages in f) occur due to instabilities in the load circuit at low bias, and correspond to retrapping to the zero-voltage state, as is common for many measurements of voltage biased Josephson junctions. As these points are analogous to the case of a zero bias supercurrent flow, they are not accompanied by photon emission.

OPERATING REGIMES UNDER LASING
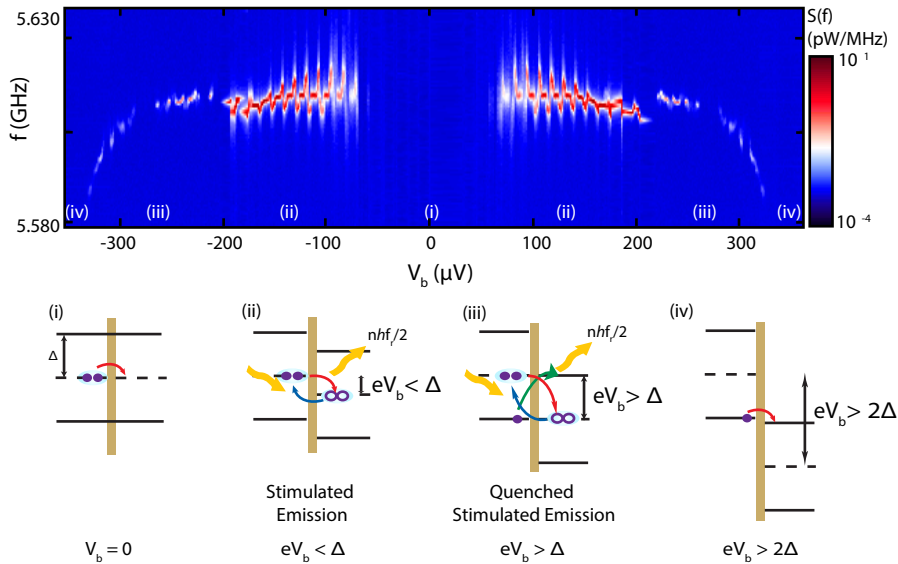
Figure 8.8: Operating regimes of the Josephson laser. Power spectral density *S(f)* over a wider range of applied voltage bias at large Josephson coupling. (i) Dissipationless supercurrent. At $V_b = 0$, Cooper pairs can directly tunnel across the junction without additional energy being dissipated. (ii) Stimulated emission. At a large Josephson coupling and a voltage bias equal to a multiple of the cavity resonance, many photons are released into the cavity. The cavity photon population is large enough that the junction can reabsorb and re-emit some of these photons. (iii) Quenched stimulated emission. When the voltage bias exceeds the superconducting gap $eV_b > \Delta$, absorption of cavity photons can also allow quasiparticles to tunnel across the junction, damping the junction and quenching the emission (iv) Resistive transport. When the voltage bias exceeds twice the superconducting gap $eV_b > 2\Delta$, direct quasiparticle transport can take place without any accompanying photon emission.

TEMPERATURE DEPENDENCE OF LASING
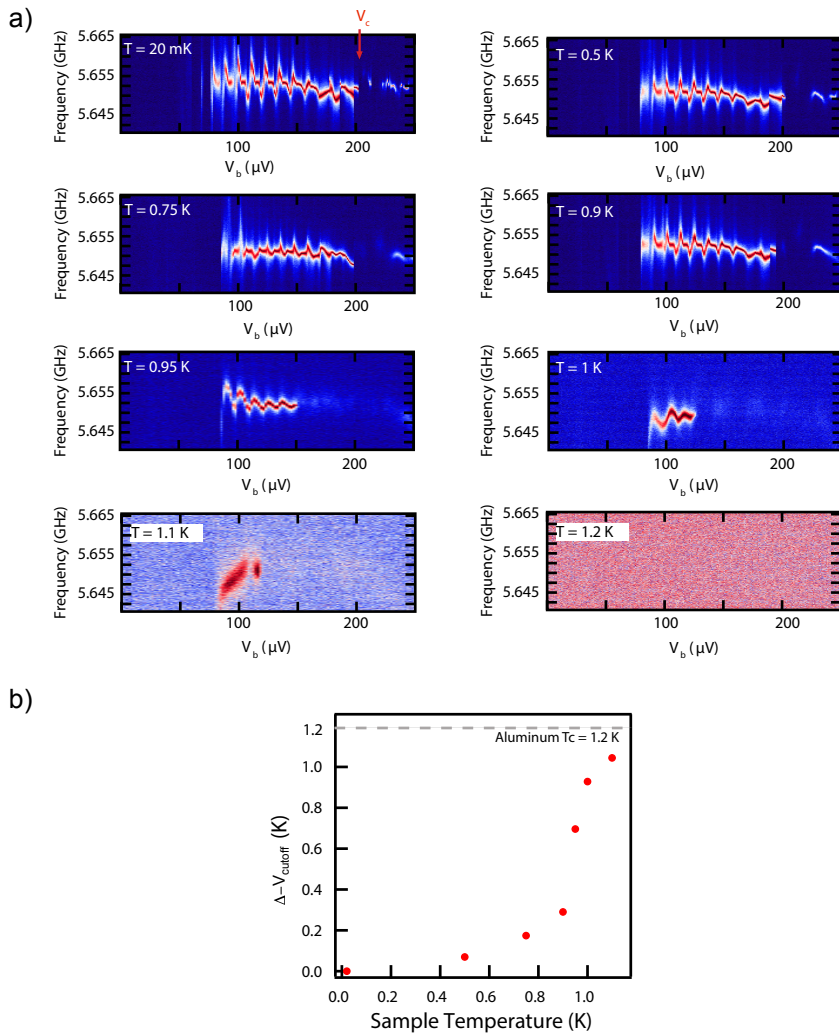
Figure 8.9: Temperature dependence of the emission. **a)** Power spectral density $S(f)$ of the emission as a function of voltage bias for different sample temperatures. **b)** The emission cutoff point V_c scales strongly with temperature close to the superconducting critical temperature of Aluminium, indicating that the upper cutoff of the emission V_c is set by excitation of quasiparticles that damp the junction.

LINEWIDTH AND OUTPUT POWER MEASUREMENTS

Figure 8.10: Linewidth narrowing under lasing. Normalized cavity transmission with the device lasing (red) and with the device off (grey). The device shows linewidth narr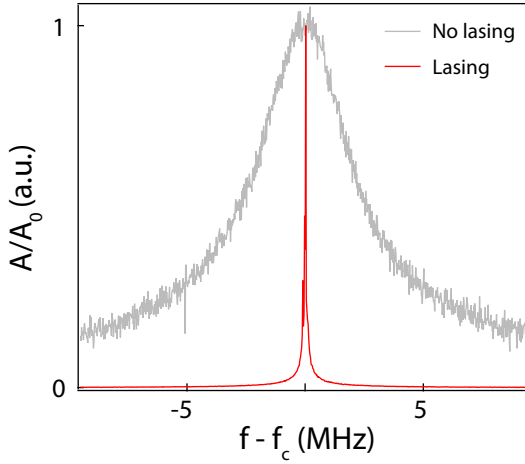owing of more than two orders of magnitude when configured for lasing. The transmission when the laser was not lasing was measured at $V_b = 31\,\mu\text{V}$, between the second and third emission peaks in Fig. 8.2a), while the trace when the laser was emitting was recorded at $V_b = 162\,\mu\text{V}$ in Fig. 8.2c). For both measurements $P_{inj} = -140\,\text{dBm}$, below the single photon power in the cavity.

By integrating the emission data in Fig. 8.11a), we estimate the output power $P_{out} = \int S(f)df = 0.255\,\text{pW}$. The DC input power to the device is calculated as $P_{in} = I_D V_b = 0.81\,\text{pW}$, where $I_D = 5\,\text{nA}$ and $V_b = 162\,\mu\text{V}$, which gives a power conversion efficiency $P_{out}/P_{in} > 0.3$.

The quantum limited laser linewidth is predicted by the Schawlow-Townes formula [28]:

$$\sigma_{ST} = hf_0 \frac{\gamma^2}{P_{out}} \tag{8.1}$$

Here, P_{out} is the power at the cavity output and γ the linewidth of the atomic transition, and is valid in the limit where $\gamma \ll \kappa$, where κ is the cavity linewidth. In the case where $\kappa \leq \gamma$, as is common for many semiconductor-based laser systems, this expression is modified by replacing γ with an effective linewidth $l_{ST}^{-1} = \gamma^{-1} + \kappa^{-1}$, which tends to $l_{ST} = \kappa$ for $\kappa \ll \gamma$ [29]. In our case, the atomic transition is the voltage bias on the Josephson junction V_b, and its linewidth is set by the residual voltage noise, which is of order 30 kHz (see Section 8.5.2), much less than κ. Using the output power calculated from by integrating the emission data in Fig. 8.11a), we calculate the Schawlow-Townes linewidth to be $\sim 14\,\text{mHz}$.

NOISE BACKGROUND CALIBRATION AND PHOTON NUMBER DISTRIBUTION

The measured power spectral density is given by $N(f) = G[N_{offset} + N_{vac} + \eta S(f)/hf]$, where G is the gain of the amplifier chain, N_{vac} is the occupation of the cavity due to
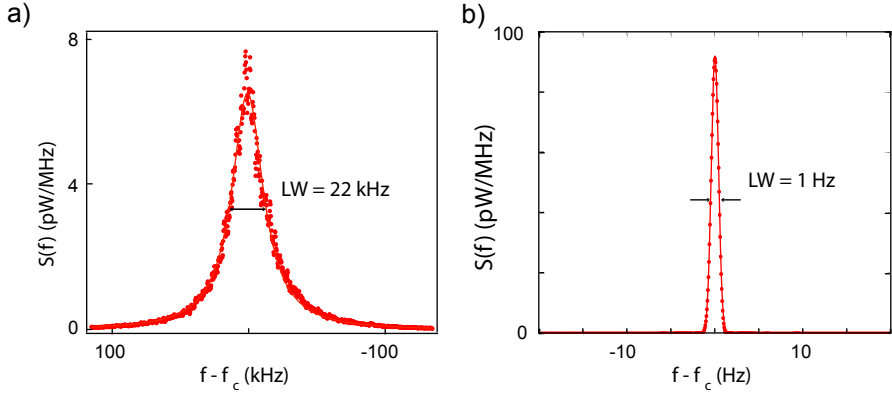
Figure 8.11: Emission linewidth of the Josephson laser. Power spectral density $S(f)$ of **a)** the free running laser and **b)** the injection locked laser, measured in the large Josephson coupling regime. In free running mode, the laser is well fit by a Lorentzian function from which we extract a full-width at half maximum linewidth $\sigma = 21.4\,\mathrm{kHz}$. This corresponds to a laser coherence time $\tau_{coh} = 1/(\pi\sigma) = 15\,\mu s$ and a coherence length $l_{coh} = \tau_{coh} c = 4.45\,\mathrm{km}$. When injection locked, the injection locked linewidth of the laser is $\sim 1\,\mathrm{Hz}$, which is limited by the linewidth of the injected tone.

thermal photons, and N_{offset} is the additional number of photons generated by the circuit including the first stage of amplification referenced back to the output of the cavity. We assume a collection efficiency $\eta = \eta_{cable}\eta_{cavity} \approx 0.013$. Here $\eta_{cavity} = \kappa_{out}/\kappa = 0.06$ describes the proportion of photons in the cavity escaping from one port of the cavity, while $\eta_{cable} \approx 0.2$ is due to the finite attenuation between the output of the cavity and input to the cryogenic amplifier due to the insertion loss of the circulator and isolator as well as additional cable losses, which we estimate to be $\sim 7\,\mathrm{dB}$. We estimate $N_{vac} = 1/(e^{\frac{hf}{k_B T}} - 1) \approx 0.015$ assuming an effective cavity temperature $T = 65\,\mathrm{mK}$. The additional photons generated by the cryogenic amplifier with noise temperature $T_{amp} = 2.1\,\mathrm{K}$ is $N_{amp} = 1/(e^{\frac{hf}{k_B T_{amp}}} - 1) \approx 7$. The noise offset is calculated as $N_{offset} = (1 + N_{amp})/\eta_{cable} - 1 \approx 40$, from which we calculate a noise number $N_{noise} = 2N_{offset} = 80$ [30]. As it is difficult to properly calibrate the mixer for such low input power, we only use the data from one mixer port in this calibration. Since we do not detect the radiation at the second output port of the mixer the noise level is effectively increased by a factor of two. This is due to the backfolding of noise at frequencies which had a positive detuning from the local oscillator

We first calibrate the additional noise of the detection circuit by measuring the emission from the cavity when the laser is off, corresponding to a bias point $V_b = 18\,\mu V$ in Fig. 8.2a). The IQ histogram $\int D(I, Q)(I^2 + Q^2)\, dI dQ$ of the radiation emitted from the cavity, shown in Fig. 8.3d), is well fit by a 2D Gaussian distribution of the form $\exp\left(\frac{-(I^2 + Q^2)}{2\sigma_{th}^2}\right)$. We scale the axes of the histogram such that the width $\sigma_{th} = \sqrt{N_{noise}/2} = 6.36$, as expected for thermal amplifier noise. In contrast, when the device is lasing, the IQ histogram takes on a distinctly different shape, resembling a donut of radius $A = \sqrt{\bar{N}} = 172$ and width $\sigma_l = 6.89$. Here the radius A corresponds to the average coherent amplitude of
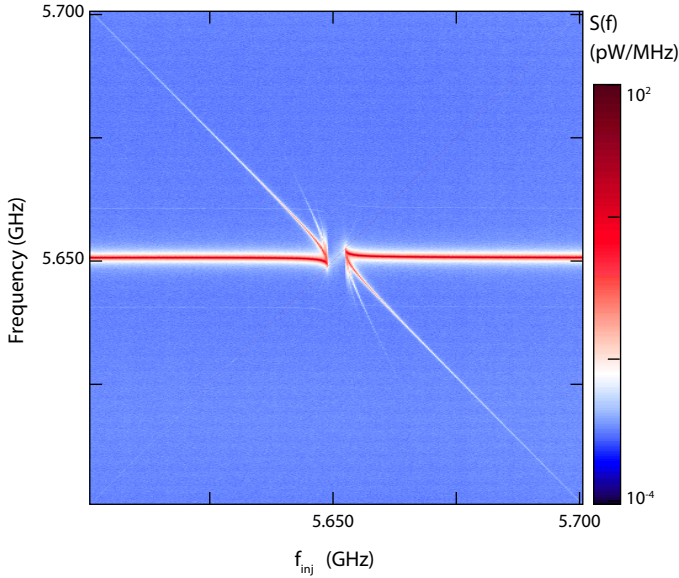
Figure 8.12: Injection locking - Sideband range. Power spectral density $S(f)$ as a function of frequency of the injected tone for an input power $P_{inj} = -90\,\text{dBm}$ showing creation of sidebands spanning more than 100 MHz.

the system, while the finite width $\sigma_l = \sqrt{(2\delta A^2 + N_{noise})/2}$ is a result of amplitude fluctuations in the cavity emission $\delta A = 2.66$ being broadened by the thermal noise from the amplifier chain. The axes of the IQ histogram acquired in Fig. 8.3e) is scaled consistently with the one acquired in Fig. 8.3d).

To extract the photon number distribution we average the acquired signal across all phase configurations $\int_0^{2\pi} \frac{d\theta}{2\pi} \exp\left[-[I + A\cos\theta]^2/2\sigma_l^2 - [Q + A\sin\theta]^2/2\sigma_l^2\right]$. By removing the effect of thermal noise from the amplifier chain, we can reconstruct the distribution at the output of the cavity, which takes the form of a broadened Gaussian $p_n \propto \exp\left[-(n-\bar{N})^2/(2\bar{N}(1+4\delta A^2))\right]$, centered around $\bar{N} \approx 29600$, as shown in the red curve in Fig. 8.3f). In contrast, for a perfectly coherent source, we would expect the emission to be in the form of a shot noise limited Poissonian distribution, which can be approximated by a Gaussian distribution of the form $p_n \propto \exp\left[-(n-\bar{N})^2/2\bar{N}\right]$ in the limit of large $\bar{N}$, as shown in the blue curve in Fig. 8.3f). The residual fluctuations in the cavity amplitude are most probably due to E_J fluctuations due to materials imperfections in the junction.

8.5.4. INJECTION LOCKING

We compare our injection locking data in Fig. 8.4 to the predictions of the Adler theory for coupled oscillators [20]. Following from [17, 31], for a given input power P_{inj}, the frequency range Δf over which the input signal can be locked is given by

$$\Delta f = C_\kappa \kappa_t \sqrt{P_{inj}/P_{out}} = \alpha \sqrt{P_{inj}}. \tag{8.2}$$

Here the prefactor $C_\kappa = 2\sqrt{\kappa_{in}\kappa_{out}}/\kappa = 0.11$ accounts for internal cavity losses. This gives $\alpha = 1.07\,\text{MHz}/\sqrt{W}$, which is in reasonable agreement with the experimentally determined value of $\alpha = (3.66 \pm 1.93)\,\text{MHz}/\sqrt{W}$, as extracted from the fit to the data in Fig. 8.4. Outside the region of injection locking, the injection of an off-resonant tone at frequency f_{inj} results in generation of higher harmonics to the bare emission at frequency $f_0 = 5.65067\,\text{GHz}$. As the frequency of the injected signal approaches that of the bare emission, both the emitted signal and higher harmonics are pulled towards the injected tone until they are locked across the frequency range Δf. The positions of the pulled emission signal and the nth harmonics are given by

$$f_n = f_{inj} + (n+1)f_h \tag{8.3}$$

where

$$f_h = (f_0 - f_{inj})\sqrt{1 - \left(\frac{\Delta f/2}{f_0 - f_{inj}}\right)}. \tag{8.4}$$

Figure 8.13a) shows the calculated positions of the pulled emission signal f_e (n = 0) and higher harmonics located at n=-2,1,2,3,4 overlaying the raw data for an input power P = $-90\,\text{dBm}$, which results in an injection locking frequency range of $\Delta f \approx 5\,\text{MHz}$. As seen from Eq. 8.3, the harmonic at $n = -1$ overlaps with the injected input tone, and so is not observed.

Adler's equation also predicts the relative powers of the sidebands when compared to the free emission power.

$$P_n/P_0 = |a_n/a_0|^2 = \left(\frac{(-f_0 + f_{inj} + f_h) + i\Delta f/2}{(f_0 - f_{inj} + f_h) - i\Delta f/2}\right)^{2n} \tag{8.5}$$

Linecuts of the injection locking data in Fig. 8.13a) are shown in Fig. 8.13b)-d). Fits to the experimental data are shown as black solid lines. Each emission peak is fit with a Lorentzian lineshape, with the input frequency fit with a Gaussian of width $\sigma = 10\,\text{kHz}$. Table 8.1 shows a comparison of the experimental and calculated harmonic frequencies f_n for each of the sidebands and the pulled emission, together with their relative emission power P_n/P_0 from solving Eq. 8.5. Frequencies are extracted by fitting the raw data with a multi-peaked Lorentzian function.

FREQUENCY COMB GENERATION

Optical frequency combs have generated significant interest in recent years [32], making it possible to extend the accuracy of the atomic clocks from the radio to the optical frequency region, leading to breakthroughs in optical metrology, high precision spectroscopy and telecommunication technologies. Recently, microwave frequency combs have also been generated using four-wave mixing in superconducting resonators [21]. Here we demonstrate a similar frequency comb by applying a voltage modulation to the Josephson junction (Fig. 8.14a), as recently described theoretically in [22]. As an example, we configure the device in the on-resonance injection locked regime ($P_{inj} = -110\,\text{dBm}$ in Fig. 8.4c) and apply a small ac excitation of frequency $f_{\text{mod}} = 111\,\text{Hz}$ to the DC bias. This generates a comb around the central pump tone with frequency separation 111 Hz, as seen in Fig. 8.14b). The total width of the comb is set by the amplitude of the modulation (Inset, 8.14b), as well as the input power of the injection lock signal.

f_{in} (GHz)	5.6447		5.6481		5.6619	
	Calc.	Exp.	Calc.	Exp.	Calc.	Exp
f_e (GHz)	5.650	5.650	5.650	5.650	5.651	5.651
f_1 (GHz)	5.656	5.656	5.651	5.652	5.640	5.640
f_2 (GHz)	5.662	5.662	5.653	5.654	5.629	-
f_3 (GHz)	5.667	-	5.654	5.656	5.618	-
f_4 (GHz)	5.673	-	5.656	5.658	5.607	-
f_{-2} (GHz)	5.639	-	5.647	5.646	5.673	-
P_1/P_0	2.9×10^{-2}	1.1×10^{-2}	2.2×10^{-1}	1.2×10^{-1}	8.1×10^{-3}	3.5×10^{-3}
P_2/P_0	8.8×10^{-4}	3.2×10^{-4}	4.8×10^{-2}	1.0×10^{-2}	6.5×10^{-5}	-
P_3/P_0	2.6×10^{-5}	-	1.0×10^{-2}	1.6×10^{-3}	5.2×10^{-7}	-
P_4/P_0	7.7×10^{-7}	-	2.3×10^{-3}	9.3×10^{-4}	4.2×10^{-9}	-
P_{-2}/P_0	7.7×10^{-7}	-	2.3×10^{-3}	9.3×10^{-4}	4.2×10^{-9}	-

Table 8.1: Calculated and experimentally determined peak positions and relative intensities of sideband harmonics under injection locking.
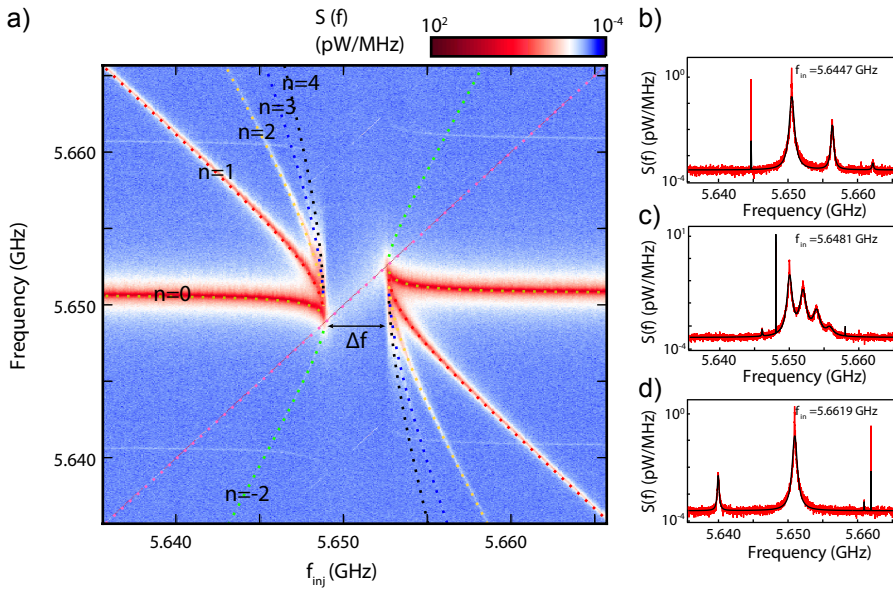
Figure 8.13: Injection locking - Comparison to theory. **a)** Power spectral density $S(f)$ as a function of frequency of the injected tone for an input power $P_{inj} = -90$ dBm. The emission is injection locked for a frequency range $\Delta f \approx 5$ MHz. Overlaying the data are the calculated positions of the pulled emission f_e and sidebands $f_{-2,1,2,3,4}$. Faint modulation sidebands can be seen at $f_e \pm 10$ MHz due to noise on the input line to the cavity. **b) – d)** Linecuts of a) corresponding to **b)** $f_{inj} = 5.6447$ GHz, **c)** $f_{inj} = 5.6481$ GHz and **d)** $f_{inj} = 5.6619$ GHz. The solid lines are fits to S(f).
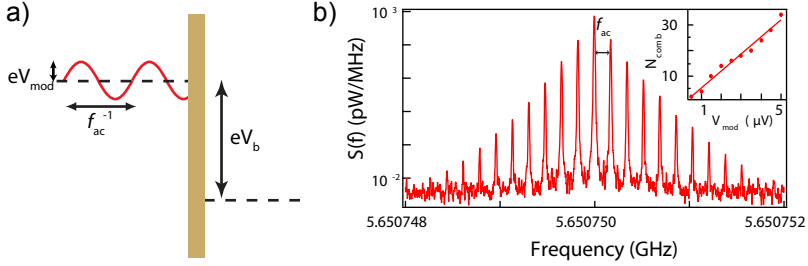
Figure 8.14: Frequency comb generation. **a) – b)** Low frequency ($f_{ac} = 111\,\text{Hz}$) modulation of the voltage bias across the SQUID under injection locking conditions generates a frequency comb of phase coherent signals spaced f_{ac} in frequency around the center emission frequency. (Inset) The comb width, N_{comb}, is controlled by V_{mod}, the amplitude of the modulation on the voltage bias.
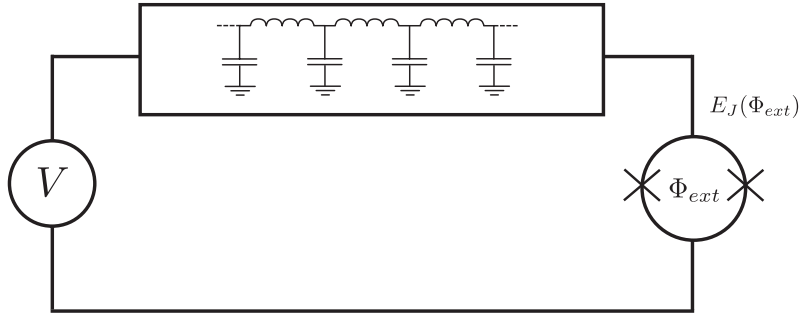
Figure 8.15: Circuit schematic. Circuit diagram of a voltage-biased Josephson junction in series with a resonator. The Josephson energy of the junction $E_J(\Phi_{ext})$ can be tuned by an external magnetic flux Φ_{ext}.

8

8.5.5. NUMERICAL MODEL

We model the circuit as an LC resonator in series with a dc-SQUID with an applied voltage bias shown in Fig. 8.15. We begin our analysis with the single mode resonator approximation as studied in Ref.'s [14, 33, 34], with the equations of motion

$$C\ddot{\varphi} = L^{-1}\varphi - \gamma\dot{\varphi} + \phi_0^{-2}E_J \sin\left(2\pi f_J t + \varphi\right), \tag{8.6}$$

with f_J the Josephson frequency, φ the resonator phase variable, C and L the capacitance and inductance of the main resonator harmonic $[f_0 = 1/(2\pi\sqrt{LC})]$, and γ the dissipation rate. The drive term is proportional to E_J and it is characterized by a dimensionless coupling strength $\lambda = E_J/\phi_0^2 C\omega_0^2$. Solving the time evolution numerically, we find that a strongly detuned drive $n \gg 1$ cannot produce a response that is only weakly dependent on f even for $\lambda \gtrsim 1$, contrary to the experimental observations (see left panels in Fig. 8.16).

Going beyond the approximation of Ref. [14] we find that a necessary extension of the model allowing for efficient down-conversion from large n is the effect of the higher

resonator modes leading us to:

$$C\ddot{\varphi}_i = i^2 L^{-1}\varphi_i - \gamma\dot{\varphi}_i + \phi_0^{-2}E_J\alpha_i \sin\left(2\pi f_J t + \sum_{i=1}^{M} \alpha_i\varphi_i\right), \tag{8.7}$$

with φ_i the phase variables of M resonator harmonics. Due to the strong nonlinearity of the equations of motion at small γ and large E_J, including the higher harmonics modes is a necessary extension of Eq. (8.6). We also verify that including Kerr nonlinearity or including the load circuit in the single mode dynamics (8.6) are not alone sufficient to reproduce the lasing behavior. The variation of the coupling strengths α_i of different modes to the Josephson junction is geometry-dependent, however we verify that the specific ratios of α_i do not influence our conclusions. For simplicity we present the results for $\alpha_i = 1$. A precise simulation of the coupling to the transmission line is beyond the scope of Eq. 8.7. In order to estimate the emitted power we therefore assume that all of the dissipation happens due to emission into the transmission line. This is supported by comparing the intrinsic resonator quality factor $Q \approx 10^5$ with the quality factor of the resonator coupled to the transmission line $Q \approx 2 \cdot 10^4$. This allows us to estimate the emitted power spectrum using $S(f) = \gamma f^2 \varphi_f^2$, with φ_f the Fourier component of φ at frequency f. Our numerical results are summarized in Fig. 8.16. The mode mixing results in approximate equipartition of emission power between the different resonator modes, and the number of available resonator modes determines the higher cutoff for the efficient down-conversion of f_J into the main harmonic of the resonator. A low E_J produces a series of disconnected peaks, as shown in the top panels of Fig. 8.16.

Studying the response of the lowest resonator harmonic more closely (see Fig. 8.17), we observe several features similar to the experimental observations. Specifically, the linewidth exhibits periodic modulation, becoming broader on resonance. The emission amplitude is continuous until a certain upper threshold, above which it separates into disconnected intervals.

Finally, we relax the assumption of equal mode spacing, unexpected in a realistic line resonator. To study the effect of incommensurate mode frequencies, we consider the detuning of mode frequencies by a small random amount: $\omega_i = (i + r_i)\omega_0$ for $i > 1$. We choose detuning r_i to be a uniformly distributed random variable in the interval $[-0.1, 0.1]$ or $[-0.3, 0.3]$. Our results are shown in Fig. 8.18. We observe that the detuning of the higher harmonics does not change the overall spectral shape of the emitted signal, except for washing out the resonant peaks corresponding to the frequencies of the higher modes.
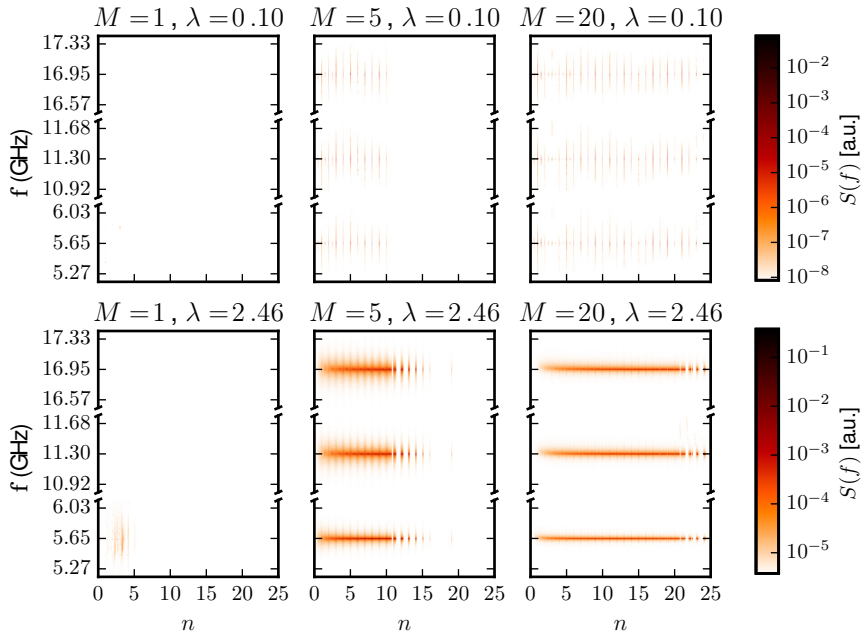
Figure 8.16: Dependence of the numerical emission spectra for different coupling strength and numbers of modes of the lowest three resonator modes.
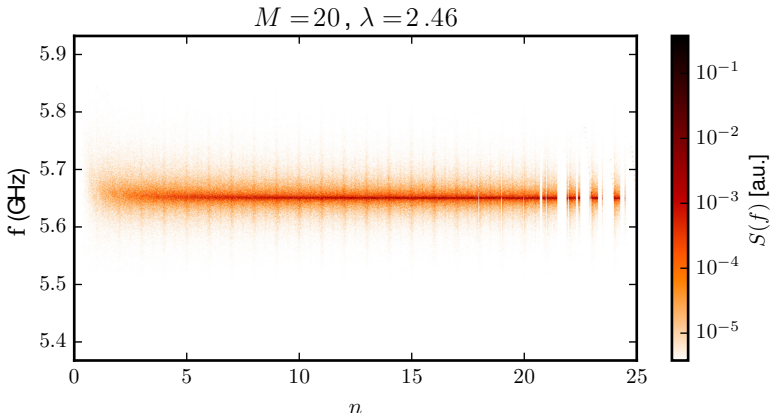
8

Figure 8.17: The emission spectrum of the lowest resonator mode for large coupling and in presence of multiple resonator modes.
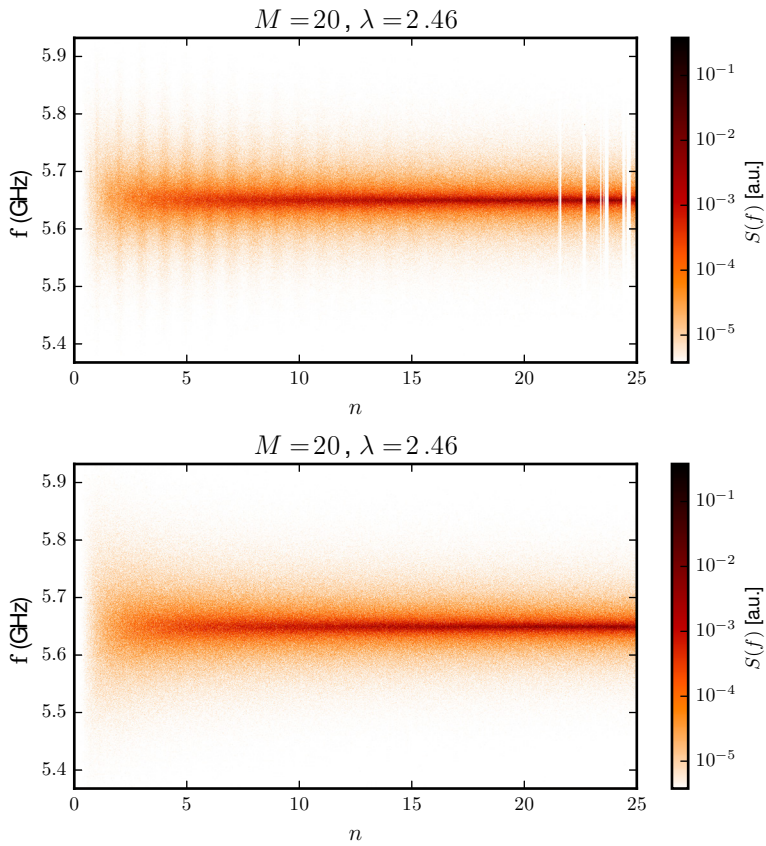
Figure 8.18: Emission spectrum of the lowest mode with **a)** 10% detuning, or **b)** 30% detuning

REFERENCES

[1] D. R. Tilley, "Superradiance in arrays of superconducting weak links," *Physics Letters A*, vol. 33, no. 4, pp. 205–206, 1970.

[2] D. Rogovin and M. Scully, "Superconductivity and macroscopic quantum phenomena," *Physics Reports*, vol. 25, no. 3, pp. 175–291, 1976.

[3] N. F. Pedersen, O. H. Soerensen, J. Mygind, P. E. Lindelof, M. T. Levinsen, and T. D. Clark, "Direct detection of the Josephson radiation emitted from superconducting thinfilm microbridges," *Applied Physics Letters*, vol. 28, no. 9, pp. 562–564, 1976.

[4] C. Varmazis, J. E. Lukens, and T. F. Finnegan, "Broadband generation of tunable Josephson radiation at microwave frequencies," *Applied Physics Letters*, vol. 30, no. 12, p. 660, 1977.

[5] P. Barbara, A. B. Cawthorne, S. V. Shitov, and C. J. Lobb, "Stimulated Emission and Amplification in Josephson Junction Arrays," *Physical Review Letters*, vol. 82, pp. 1963–1966, mar 1999.

[6] L. Ozyuzer, A. E. Koshelev, C. Kurter, N. Gopalsami, Q. Li, M. Tachiki, K. Kadowaki, T. Yamamoto, H. Minami, H. Yamaguchi, T. Tachiki, K. E. Gray, W.-K. Kwok, and U. Welp, "Emission of Coherent THz Radiation from Superconductors," *Science*, vol. 318, pp. 1291–1293, nov 2007.

[7] M. Hofheinz, F. Portier, Q. Baudouin, P. Joyez, D. Vion, P. Bertet, P. Roche, and D. Esteve, "Bright Side of the Coulomb Blockade," *Physical Review Letters*, vol. 106, p. 217005, may 2011.

[8] F. Chen, J. Li, A. D. Armour, E. Brahimi, J. Stettenheim, A. J. Sirois, R. W. Simmonds, M. P. Blencowe, and A. J. Rimberg, "Realization of a single-Cooper-pair Josephson laser," *Physical Review B*, vol. 90, p. 20506, jul 2014.

[9] O. Astafiev, K. Inomata, A. O. Niskanen, T. Yamamoto, Y. A. Pashkin, Y. Nakamura, and J. S. Tsai, "Single artificial-atom lasing," *Nature*, vol. 449, no. 7162, pp. 588–590, 2007.

[10] Y.-Y. Liu, J. Stehlik, C. Eichler, M. J. Gullans, J. M. Taylor, and J. R. Petta, "Semiconductor double quantum dot micromaser," *Science*, vol. 347, pp. 285–287, jan 2015.

[11] F. Chen, A. J. Sirois, R. W. Simmonds, and A. J. Rimberg, "Introduction of a dc bias into a high-q superconducting microwave cavity," *Applied Physics Letters*, vol. 98, no. 13, p. 132509, 2011.

[12] A. Wallraff, D. I. Schuster, A. Blais, L. Frunzio, R.-S. Huang, J. Majer, S. Kumar, S. M. Girvin, and R. J. Schoelkopf, "Strong coupling of a single photon to a superconducting qubit using circuit quantum electrodynamics," *Nature*, vol. 431, pp. 162–167, sep 2004.

8

[13] M. H. Devoret, D. Esteve, H. Grabert, G.-L. Ingold, H. Pothier, and C. Urbina, "Effect of the electromagnetic environment on the Coulomb blockade in ultrasmall tunnel junctions," *Physical Review Letters*, vol. 64, pp. 1824–1827, apr 1990.

[14] S. Meister, M. Mecklenburg, V. Gramich, J. T. Stockburger, J. Ankerhold, and B. Kubala, "Resonators coupled to voltage-biased Josephson junctions: From linear response to strongly driven nonlinear oscillations," *Physical Review B*, vol. 92, p. 174532, nov 2015.

[15] O. Astafiev, K. Inomata, A. O. Niskanen, T. Yamamoto, Y. A. Pashkin, Y. Nakamura, and J. S. Tsai, "Single artificial-atom lasing," *Nature*, vol. 449, no. 7162, pp. 588–590, 2007.

[16] H. L. Stover, "Locking of laser oscillators by light injection," *Applied Physics Letters*, vol. 8, no. 4, p. 91, 1966.

[17] Y.-Y. Liu, J. Stehlik, M. J. Gullans, J. M. Taylor, and J. R. Petta, "Injection locking of a semiconductor double-quantum-dot micromaser," *Physical Review A*, vol. 92, p. 053802, nov 2015.

[18] B. Yurke, P. G. Kaminsky, R. E. Miller, E. A. Whittaker, A. D. Smith, A. H. Silver, and R. W. Simon, "Observation of 4.2-K equilibrium-noise squeezing via a Josephson-parametric amplifier," *Physical Review Letters*, vol. 60, pp. 764–767, feb 1988.

[19] I. Siddiqi, R. Vijay, F. Pierre, C. M. Wilson, M. Metcalfe, C. Rigetti, L. Frunzio, and M. H. Devoret, "RF-Driven Josephson Bifurcation Amplifier for Quantum Measurement," *Physical Review Letters*, vol. 93, p. 207002, nov 2004.

[20] R. Adler, "A Study of Locking Phenomena in Oscillators," *Proceedings of the IRE*, vol. 34, pp. 351–357, jun 1946.

[21] R. P. Erickson, M. R. Vissers, M. Sandberg, S. R. Jefferts, and D. P. Pappas, "Frequency Comb Generation in Superconducting Resonators," *Physical Review Letters*, vol. 113, p. 187002, oct 2014.

[22] P. Solinas, S. Gasparinetti, D. Golubev, and F. Giazotto, "A Josephson radiation comb generator," *Scientific Reports*, vol. 1, p. 12260, jul 2015.

[23] J. Faist, F. Capasso, D. L. Sivco, C. Sirtori, A. L. Hutchinson, and A. Y. Cho, "Quantum Cascade Laser," *Science*, vol. 264, pp. 553–556, apr 1994.

[24] Z. L. Wang, Y. P. Zhong, L. J. He, H. Wang, J. M. Martinis, A. N. Cleland, and Q. W. Xie, "Quantum state characterization of a fast tunable superconducting resonator," *Applied Physics Letters*, vol. 102, no. 16, p. 163503, 2013.

[25] F. C. Wellstood, C. Urbina, and J. Clarke, "Low frequency noise in dc superconducting quantum interference devices below 1 K," *Applied Physics Letters*, vol. 50, no. 12, pp. 772–774, 1987.

8

[26] R. N. Simons, *Coplanar Waveguide Circuits, Components, and Systems*. Wiley Series in Microwave and Optical Engineering, Wiley, 2004.

[27] L. Spietz, K. W. Lehnert, I. Siddiqi, and R. J. Schoelkopf, "Primary Electronic Thermometry Using the Shot Noise of a Tunnel Junction," *Science*, vol. 300, no. 5627, pp. 1929–1932, 2003.

[28] A. L. Schawlow and C. H. Townes, "Infrared and Optical Masers," *Physical Review*, vol. 112, pp. 1940–1949, dec 1958.

[29] H. Wiseman, "Light amplification without stimulated emission: Beyond the standard quantum limit to the laser linewidth," *Physical Review A*, vol. 60, no. 5, pp. 4083–4093, 1999.

[30] C. Eichler, *Experimental characterization of quantum microwave radiation and its entanglement with a superconducting qubit.* PhD thesis, ETH Zurich, 2013.

[31] M. Armand, "On the output spectrum of unlocked driven oscillators," *Proceedings of the IEEE*, vol. 57, pp. 798–799, may 1969.

[32] S. T. Cundiff and J. Ye, "Colloquium: Femtosecond optical frequency combs," *Reviews of Modern Physics*, vol. 75, no. 1, pp. 325–342, 2003.

[33] V. Gramich, B. Kubala, S. Rohrer, and J. Ankerhold, "From Coulomb-Blockade to Nonlinear Quantum Dynamics in a Superconducting Circuit with a Resonator," *Physical Review Letters*, vol. 111, p. 247002, dec 2013.

[34] A. D. Armour, M. P. Blencowe, E. Brahimi, and A. J. Rimberg, "Universal quantum fluctuations of a cavity mode driven by a Josephson junction," *Physical Review Letters*, vol. 111, no. 24, pp. 1–5, 2013.

8

9

OUTLOOK AND DISCUSSION

9.1. RESULTS

The main conclusions from the previous chapters are:

chapter 4 Measurements of QPC devices with varying contact preparations show that both dry etching steps, O_2-plasma and He milling, are essential to create high quality contacts. Moreover we find that electron scattering in our nanowire QPCs is dominated by surface scattering which can be strongly reduced by extended sample evacuation immediately before cool down. This enabled the observation of ballistic transport in devices with channel lengths of up to 400 nm.

chapter 5 By using the improved contact recipe discussed in chapter 4 in combination with a high quality dielectric we are able to reliably fabricate ballistic InSb nanowire devices. We find the energy spacing of the first subband $E_1 \approx 17$ meV and the g-factor of the first three subbands $g_1 = 39 \pm 1$ and $g_{2,3} = 40 \pm 1$. Studying the subband evolution reveals the emergence of an orbital degeneracy between the second and third subband for magnetic fields aligned perpendicular to the nanowire axis.

chapter 6 We observe a reentrant conductance feature in a InSb nanowire QPC consistent with the expected signature of a helical gap. By measuring the evolution in a linearly increasing as well as a rotating magnetic field we confirm that this feature originates from spin-orbit interaction. Comparisons with simulations extract an estimated spin-orbit energy $E_{SO} = 6.5$ meV which corresponds to $l_{SO} = 20.48$ nm and $\alpha_R = 2.66$ eVÅ. Measurements of a second device give $E_{SO} = 5.6$ meV, $l_{SO} = 22.04$ nm and $\alpha_R = 2.47$ eVÅ. This is significantly larger than earlier values extracted for the spin-orbit strength in our nanowires.

chapter 7 We demonstrate microwave readout of a InSb nanowire double quantum dot using a superconducting CPW resonator and extract a electron-photon coupling strength of $g_c/2\pi \sim 150$ MHz.

chapter 8 We conclusively demonstrate lasing from a dc-biased Josephson junction in the strong coupling regime. Analysis of the output emission statistics shows 15 µs of phase coherence, with no sub-threshold behavior. The Josephson junction laser does not suffer from charge-noise-induced linewidth broadening and reaches an injection locked linewidth of < 1 Hz. The device produces frequency tunability over 50 MHz via direct tuning of the cavity frequency and over > 100 MHz through the generation of injection-locking sidebands

9.2. STRENGTH OF THE SPIN-ORBIT INTERACTION

Most approaches to model SOI in nanowires start with well understood models for three and two dimensional systems [1] and reduce them down to one dimension, similar to the approach take in chapter 2. In nanowires, however, confinement effects are very pronounced and can strongly modify such simple models [1]. Because Rashba SOI arises from broken structural inversion symmetry, it is particularly sensitive to differences in the device geometry and nanowire surface which change the confinement potential. In

	E_{SO}	l_{SO} [nm]	α_R [eVÅ]
Spin-orbit qubit [2]	28–51 µeV	230–310	0.18–0.24
Weak antilocalization [3]	0.25–1 meV	50–100	0.5–1
Helical gap (chapter 6)	5.6–6.5 meV	20–22	2.47–2.66

Table 9.1: Comparison of E_{SO}, l_{SO} and α_R

experiments this is reflected by the fact that three different measurements of the SOI in similar InSb nanowires found variation of α_R (E_{SO}) by a factor of more than 10 (100). Table 9.1 summarizes the experimental values extracted from these measurements. In the following paragraph I will compare the different experiments and discuss the observed differences.

The first experiment that could directly extract the strength of the SOI was performed in InSb nanowire spin-orbit qubits [2]. SOI induces an anticrossing between the hybridized energy levels inside a double quantum dot which could be measured through qubit spectroscopy. Additionally, angle dependent measurements resolved the orientation of B_{SO}, which was found to be oriented perpendicular to the nanowire and parallel to the substrate. This is consistent with Rashba SOI caused by a broken structural inversion asymmetry from an electric field oriented perpendicular to the substrate plane. The measured spin-orbit strength α_R = 0.18–0.26 eVÅ, l_{SO} = 230–310 nm and E_{SO} = 28–51 µeV is significantly smaller than the values we extract in chapter 6. To understand this difference one needs to consider the different measurement regimes which directly influence SOI. The confinement inside a quantum dot produces a very different electrostatic environment than a QPC, where electrons propagate freely along the nanowire. In a second experiment, weak-antilocalization (WAL) was measured in dual (top and bottom) gated InSb nanowires [3]. WAL typically assumes diffusive bulk transport and to account for this, long diffusive channels were used. Additionally, a new model was developed which is applicable in a quasi 3D nanowire system, when the nanowire width W is comparable to the electron mean free path ($W/l_e \approx 1 - 2$). These measurements provide a more realistic estimate for the spin-orbit strength of 1D electron transport in a high conductance regime, where many subbands are occupied. In agreement with the earlier argument about the role of confinement, the extracted strength of the SOI is about ten times larger than the value measured in quantum dots; α_R = 0.5–1 eVÅ, l_{SO} = 50–100 nm and E_{SO} = 0.25–1 meV. These measurements provide a first estimate of the SOI experienced by propagating electrons inside the nanowire which, however, only apply in a diffusive multi subband regime. Compared to this the first subband experiences the lowest confinement and is therefore expected to experience the strongest SOI.

Besides this we also have to take the selectivity of our experiments into account. The simulations in Fig.6.12 and 6.14 show that the visibility of a helical gap depends crucially on the QPC channel length. Within the current experimental limits, only devices with exceptionally strong SOI will show up in measurements. For our results we fabricated a large number of QPCs and only two devices showed clear signatures of a helical gap. It is possible that some of them did not show a helical signature because they had weaker SOI. In that case it would very valuable to understand what factors caused such excep-

9

tionally strong SOI. This could be either due to external factors like a specific distribution of surface dopands causing stronger electric field gradients or it could also be intrinsic to the nanowires. Very recent measurements of InSb nanowires with atom probe spectroscopy [4], found a residual Arsenic content of up to 4 % in nanowires grown under similar conditions. Such contaminations could further modify SOI. It has also been proposed that a finite Dresselhaus SOI component might reemerge in nanowires. Typically Dresselhaus SOI is assumed to be negligible because it vanishes for electrons moving along the [111] direction [1] - the growth direction of our nanowires. This assumption in only strictly true in translationally invariant 2D systems. Symmetry breaking because of the finite system size may be enough to induce a finite Dresselhaus component in our devices. We believe that in combination these effect can explain the surprisingly large values of the SOI in our measurements.

In the topological regime, the size of the induced topological gap strongly depends on E_{SO} and a good understanding SOI in nanowires is important to optimize the homogeneity and size of the topological gap. The measurements presented in chapter 6 are therefore not only important as experimental confirmation for the non superconducting side of Majorana zero modes (MZM), they also take the first step towards a better understanding of the SOI in the lowest subband. The biggest remaining difficulty is identifying a reliable technique that can reliably measure and compare the SOI of individual subbands across many different nanowires. Because helical gap measurements are too sensitive to the device geometry, they will not work for wires with weaker, SOI unless the mean free path can be significantly enhanced.

9.3. CONSEQUENCES FOR MAJORANA DEVICES.

The results presented in this thesis are exemplary for the impressive improvements that research on semiconducting nanowires has seen over the past years and demonstrate that InSb nanowires continue to be a promising platform for studying Majorana physics. After the initial signatures of Majorana bound states in tunnel spectroscopy [5–7], many follow up experiments have deepened our understanding of hybrid nanowire-superconducting devices [8, 9] and device simulations also continuously improve [10–12]. New experiments are now attempting to directly demonstrate the non-Abelian statistics of MZM for which many different designs have been suggested. First proposals used nanowire T-junctions to either physically move the topological edge with local gates [13] or to tune the interaction between different MZMs [14–16]. Motivated by this, the nanowire growth advanced enough to create X- and T-shaped nanowire structures [17, 18]. However, the interplay between diameter dependent confinement, orbital effects, and surface states can create a strongly anisotropic subband dispersion with magnetic field as was shown in chapter 5. In a T-structure, the magnetic field always has a perpendicular component to at least one of the nanowire arms which modifies the size of the topological gap through orbital effects and subband degeneracies [10]. To avoid this, newer designs for braiding circuits avoid T-shapes and use parallel nanowires where individual MZM are coupled by superconductors and gate defined quantum dots [19–22]. Readout of the quantum dots can then be performed either with a local charge sensor or with a superconducting resonator similar to chapter 7 and reference [23]. All the individual building blocks of these different braiding circuits have, in principle, been developed

and the research in the past years has significantly increased our understanding of the underlying physics . Nevertheless important questions such as the size and interactions strength of MZM and the relevant time scales of individual gate operations and braiding operations still remain open.

9.4. FUTURE EXPERIMENTS

In the final part of this chapter some additional follow up experiments are proposed. They can further improve the understanding of the physics and material properties in our nanowire devices and explore new physics that emerges through electron-photon interaction.

1. **Using QPCs for nanowire characterization.** The straightforward fabrication and high device yield make QPCs attractive as standard test devices to study nanowire properties and to benchmark fabrication steps. So far the individual device parameters like subband spacing, g-factor and orbital effects vary strongly between individual devices. Getting a better understanding of the underlying mechanisms by, for example, looking at the differences between individual growth batches, would be an important step to tailor the nanowire growth for braiding experiments.

2. **Spin-orbit induced subband anticrossings.** Measurements of the subband dispersion in a magnetic field, can not only be used to extract information about the subband spacing, g-factor and orbital effects. At the correct magnetic field orientation, the spin-orbit coupling also induces an anticrossing between subbands of opposite spin orientation. Measurements in GaAs hole QPCs [24] demonstrate this, and use it to extract a subband specific spin-orbit strength. In our nanowires, the limiting factor would be the reduced visibility of higher subbands, but in short QPCs it should be possible to observe an anticrossing in the lower subbands and get an independent estimate for E_{SO}, α and l_{SO}.

Over the past years there has been growing interest in embedding semiconducting structures inside microwave resonators. Many different experiments studied the emission of quantum dots and (superconducting) tunnel-junctions, as well as their interaction with microwave photons [25, 26]. Chapter 7 demonstrates that nanowires are perfect candidates for such experiments, because they are easy to integrate into the existing fabrication and provide efficient coupling to the resonator. A single semiconducting nanowire contacted by either normal or metallic contacts can act as a flexible and gate tunable emitter.

3. **Capacitative sensing of a QPC.** One simple, yet interesting experiment along such lines would be measurements of a nanowire QPC embedded inside a microwave resonator. They can be performed in the existing setup used in chapters 7 & 8 and would only require minor adjustments to the sample design. Simply replacing the five fine gates of the nanowire double quantum dot by one wide gate and using the new contact recipe is enough. The resonator response can be used to capacitively measure the nanowire subband dispersion, analogous to SET reflectometry measurements. As alternative method for detecting the helical gap, this circumvents the sensitive geometric requirements of conductance measurements.

9

4. **Nanowire Josephson junction laser.** Another possibility is to replace the nanowire contacts by a superconductor, which creates a gate tunable nanowire Josephson junction. At strong coupling, this is a direct extension of the results of chapter 8 only now with a coupling that can be tuned by a local gate that would allow much faster tuning of the emission and promises on-chip generation of fast microwave pulses. First experiments with this system are already on the way and have not only demonstrated gate control but also showed a reduced linewidth.

Even more fascinating experiments are possible when we transfer the methods developed in quantum optics into the microwave regime and use them to study solid-state emitters [27, 28]. Pioneering experiments have successfully demonstrated that this is possible with circuit QED and superconducting qubits. Two key quantities of interest in quantum optics are the first and second order correlation functions $g^{(1)}(\tau)$ and $g^{(2)}(\tau)$. The first order function measures amplitude correlations and is well known from classical interference experiments. In the second order function intensity correlations are measured, which gives information about photon statistics. Assuming the electric field inside the resonator consists of only a single mode, reduces $g^{(1),(2)}$ to a very simple form that only depends on the photon creation and annihilation operators a, $a^\dagger$:

$$g^{(1)}(\tau) = \frac{\langle a^\dagger(0) a(\tau) \rangle}{\langle a^\dagger a \rangle} \tag{9.1}$$

$$g^{(2)}(\tau) = \frac{\langle a^\dagger(0) a^\dagger(\tau) a(\tau) a(0) \rangle}{\langle a^\dagger a \rangle^2} \tag{9.2}$$

$g^{(2)}(\tau)$ measures the probability of a second detection (delayed by time τ) after a first photon was observed. In chaotic light, for example from a thermal source, photons bunch together which increases the change of a correlated detection around $\tau = 0$. In fact it can be shown that any light emitted from a classical source satisfies $g^{(2)}(0) \geq g^{(2)}(\tau) \geq 1$. Only quantum emitters which can create sub-poissonian photon distributions, for example anti-bunching, show $g^{(2)}(0) < 1$. Measurements of $g^{(2)}$ can therefore be used to identify single photon sources. Different from the two experiments suggested above, such measurements have to operate at the single photon level. In optical systems, efficient single photon detectors are available for this. However in the microwave regime, photon energies are orders of magnitude lower which makes single microwave photon detection difficult. In principle it is possible to extract $g^{(2)}$ in the existing heterodyne setup used for the measurements in chapters 7 and 8. However, the noise added in the detection chain will dominate the signal and require excessively long measurement times. Reference 29 estimates that the amplifier noise alone is 700 times stronger than the single-photon power. It also demonstrates an elegant way to improve on this by including an on chip beam-splitter at the cavity output and amplifying both output ports of the splitter independently. This significantly reduces the amplifier noise, because most of it is uncorrelated and will average out. In Reference 29 this improved the observed system noise temperature by over two orders of magnitude, from initially 10.6 K down to 80 mK. A second option is to replace the HEMT amplifier by a Josephson parametric amplifier which also significantly reduces noise.

5. **Quantum light bulb.** The photon emission of a voltage biased QPC has been stud-

ied theoretically in great detail [30–35]. However, to my knowledge, no experiment realization of this has been reported. Different to quantum dots, QPCs have no discreet energy levels but rather a continuum of states. Photon emission or absorption therefore requires a finite bias voltage and happens as electrons flow across the constriction and dissipate energy. Because the photon emission directly follows electron transport, this is a great tool to study the statistics of electron transport through the QPC. At large bias voltages and high temperatures, many modes inside the QPC are occupied and the emitted light is expected to mirror a thermal source with a gaussian photon distribution. If however the temperature can be lowered enough and only a single mode inside the QPC is occupied new interesting behavior is predicted. The electrons will then imprint their fermionic behavior on the microwave photons and one expects to observe photon anti-bunching which can be revealed by measuring the second order correlation function $g^{(2)}(\tau)$. Experimentally this requires operation at finite magnetic field to break the electron spin degeneracy and occupy only a single subbands. The high g-factor of InSb reduces the required field and CPW resonators made of NbTiN that can operate up to several Tesla have already been developed in our group. References [31, 33] estimate the visibility of antibunching at realistic experimental conditions and find that it is lost if the temperature exceeds the resonator bandwidth $k_B T > 0.25\hbar\gamma$. This means, overcoupled resonators are required such that individual photons are emitted fast enough before exciting a second photon inside the cavity.

6. **Josephson and Majorana radiation.** Emission from AL/AlO2/Al Josephson junctions also attracted great interest [36–40] and demonstrated emission of non-classical states of light. Similar effects can be expected from a nanowire Josephson junction, with the added advantage of gate tunability. Measurements at finite magnetic field can also be used to study the emission of a topological Josephson junction such as proposed in references [41–47].

REFERENCES

[1] R. Winkler, S. Papadakis, E. De Poortere, and M. Shayegan, *Spin-Orbit Coupling in Two-Dimensional Electron and Hole Systems*, vol. 41. Springer, 2003.

[2] S. Nadj-Perge, V. Pribiag, J. Van den Berg, K. Zuo, S. Plissard, E. Bakkers, S. Frolov, and L. Kouwenhoven, "Spectroscopy of spin-orbit quantum bits in indium antimonide nanowires," *Physical review letters*, vol. 108, no. 16, p. 166801, 2012.

[3] I. Van Weperen, B. Tarasinski, D. Eeltink, V. Pribiag, S. Plissard, E. Bakkers, L. Kouwenhoven, and M. Wimmer, "Spin-orbit interaction in insb nanowires," *Physical Review B*, vol. 91, no. 20, p. 201413, 2015.

[4] S. Koelling, A. Li, A. Cavalli, S. Assali, D. Car, S. Gazibegovic, E. P. Bakkers, and P. M. Koenraad, "Atom-by-atom analysis of semiconductor nanowires with parts per million sensitivity," *Nano Lett.*, vol. 17, no. 2, pp. 599–605, 2017.

[5] V. Mourik, K. Zuo, S. M. Frolov, S. R. Plissard, E. P. A. M. Bakkers, and L. P. Kouwen-

9

hoven, "Signatures of majorana fermions in hybrid superconductor-semiconductor nanowire devices," *Science*, vol. 336, no. 6084, pp. 1003–1007, 2012.

[6] H. O. H. Churchill, V. Fatemi, K. Grove-Rasmussen, M. T. Deng, P. Caroff, H. Q. Xu, and C. M. Marcus, "Superconductor-nanowire devices from tunneling to the multi-channel regime: Zero-bias oscillations and magnetoconductance crossover," *Phys. Rev. B*, vol. 87, p. 241401, Jun 2013.

[7] M. T. Deng, C. L. Yu, G. Y. Huang, M. Larsson, P. Caroff, and H. Q. Xu, "Anomalous zero-bias conductance peak in a nb–insb nanowire–nb hybrid device," *Nano Lett.*, vol. 12, no. 12, pp. 6414–6419, 2012.

[8] W. Chang, S. M. Albrecht, T. S. Jespersen, F. Kuemmeth, P. Krogstrup, J. Nygård, and C. M. Marcus, "Hard gap in epitaxial semiconductor–superconductor nanowires," *Nat. Nanotechnol.*, vol. 10, no. 3, pp. 232–236, 2015.

[9] S. M. Albrecht, A. Higginbotham, M. Madsen, F. Kuemmeth, T. S. Jespersen, J. Nygård, P. Krogstrup, and C. Marcus, "Exponential protection of zero modes in majorana islands," *Nature*, vol. 531, no. 7593, pp. 206–209, 2016.

[10] B. Nijholt and A. R. Akhmerov, "Orbital effect of magnetic field on the majorana phase diagram," *arXiv:1509.02675*, 2015.

[11] J. D. Sau, S. Tewari, and S. D. Sarma, "Experimental and materials considerations for the topological superconducting state in electron-and hole-doped semiconductors: Searching for non-abelian majorana modes in 1d nanowires and 2d heterostructures," *Physical Review B*, vol. 85, no. 6, p. 064512, 2012.

[12] A. Vuik, D. Eeltink, A. R. Akhmerov, and M. Wimmer, "Effects of the electrostatic environment on the majorana nanowire devices," *arXiv:1511.08044*, 2015.

[13] J. Alicea, Y. Oreg, G. Refael, F. Von Oppen, and M. P. Fisher, "Non-abelian statistics and topological quantum information processing in 1d wire networks," *Nature Physics*, vol. 7, no. 5, pp. 412–417, 2011.

[14] D. Aasen, M. Hell, R. V. Mishmash, A. Higginbotham, J. Danon, M. Leijnse, T. S. Jespersen, J. A. Folk, C. M. Marcus, K. Flensberg, *et al.*, "Milestones toward majorana-based quantum computing," *Physical Review X*, vol. 6, no. 3, p. 031016, 2016.

[15] F. Hassler, A. Akhmerov, and C. Beenakker, "The top-transmon: a hybrid superconducting qubit for parity-protected quantum computation," *New Journal of Physics*, vol. 13, no. 9, p. 095004, 2011.

[16] T. Hyart, B. Van Heck, I. Fulga, M. Burrello, A. Akhmerov, and C. Beenakker, "Flux-controlled quantum computation with majorana fermions," *Physical Review B*, vol. 88, no. 3, p. 035121, 2013.

[17] S. R. Plissard, I. van Weperen, D. Car, M. A. Verheijen, G. W. Immink, J. Kammhuber, L. J. Cornelissen, D. B. Szombati, A. Geresdi, S. M. Frolov, L. P. Kouwenhoven, and E. P. A. M. Bakkers, "Formation and electronic properties of InSb nanocrosses," *Nat. Nanotechnol.*, vol. 8, no. 11, pp. 859–864, 2013.

[18] D. Car, J. Wang, M. A. Verheijen, E. P. A. M. Bakkers, and S. R. Plissard, "Rationally designed single-crystalline nanowire networks," *Adv. Mater.*, vol. 26, no. 28, pp. 4875–4879, 2014.

[19] S. Plugge, A. Rasmussen, R. Egger, and K. Flensberg, "Majorana box qubits," *New Journal of Physics*, vol. 19, no. 1, p. 012001, 2017.

[20] T. Karzig, C. Knapp, R. Lutchyn, P. Bonderson, M. Hastings, C. Nayak, J. Alicea, K. Flensberg, S. Plugge, Y. Oreg, *et al.*, "Scalable designs for quasiparticle-poisoning-protected topological quantum computation with majorana zero modes," *arXiv preprint arXiv:1610.05289*, 2016.

[21] S. Vijay and L. Fu, "Teleportation-based quantum information processing with majorana zero modes," *Physical Review B*, vol. 94, no. 23, p. 235446, 2016.

[22] M. Hell, J. Danon, K. Flensberg, and M. Leijnse, "Time scales for majorana manipulation using coulomb blockade in gate-controlled superconducting nanowires," *Physical Review B*, vol. 94, no. 3, p. 035424, 2016.

[23] D. Ristè, C. Bultink, M. Tiggelman, R. Schouten, K. Lehnert, and L. DiCarlo, "Millisecond charge-parity fluctuations and induced decoherence in a superconducting transmon qubit," *Nature Communications*, vol. 4, p. 1913, 2013.

[24] F. Nichele, S. Chesi, S. Hennel, A. Wittmann, C. Gerl, W. Wegscheider, D. Loss, T. Ihn, and K. Ensslin, "Characterization of spin-orbit interactions of gaas heavy holes using a quantum point contact," *Phys. Rev. Lett.*, vol. 113, p. 046801, Jul 2014.

[25] K. D. Petersson, L. W. McFaul, M. D. Schroer, M. Jung, J. M. Taylor, A. A. Houck, and J. R. Petta, "Circuit quantum electrodynamics with a spin qubit," *Nature*, vol. 490, no. 7420, pp. 380–383, 2012.

[26] T. Frey, P. Leek, M. Beck, A. Blais, T. Ihn, K. Ensslin, and A. Wallraff, "Dipole coupling of a double quantum dot to a microwave resonator," *Physical Review Letters*, vol. 108, no. 4, p. 046807, 2012.

[27] A. Cottet, T. Kontos, and B. Douçot, "Electron-photon coupling in mesoscopic quantum electrodynamics," *Phys. Rev. B*, vol. 91, p. 205417, May 2015.

[28] C. Altimiras, F. Portier, and P. Joyez, "Interacting electrodynamics of short coherent conductors in quantum circuits," *Phys. Rev. X*, vol. 6, p. 031002, Jul 2016.

[29] D. Bozyigit, C. Lang, L. Steffen, J. Fink, C. Eichler, M. Baur, R. Bianchetti, P. Leek, S. Filipp, M. Da Silva, *et al.*, "Antibunching of microwave-frequency photons observed in correlation measurements using linear detectors," *Nature Physics*, vol. 7, no. 2, pp. 154–158, 2011.

[30] C. Beenakker and H. Schomerus, "Antibunched photons emitted by a quantum point contact out of equilibrium," *Physical review letters*, vol. 93, no. 9, p. 096801, 2004.

9

[31] I. Fulga, F. Hassler, and C. Beenakker, "Nonzero temperature effects on antibunched photons emitted by a quantum point contact out of equilibrium," *Physical Review B*, vol. 81, no. 11, p. 115331, 2010.

[32] A. V. Lebedev, G. B. Lesovik, and G. Blatter, "Statistics of radiation emitted from a quantum point contact," *Phys. Rev. B*, vol. 81, p. 155421, Apr 2010.

[33] F. Hassler and D. Otten, "Second-order coherence of microwave photons emitted by a quantum point contact," *Physical Review B*, vol. 92, no. 19, p. 195417, 2015.

[34] U. C. Mendes and C. Mora, "Electron-photon interaction in a quantum point contact coupled to a microwave resonator," *Physical Review B*, vol. 93, no. 23, p. 235450, 2016.

[35] A. L. Grimsmo, F. Qassemi, B. Reulet, and A. Blais, "Quantum optics theory of electronic noise in coherent conductors," *Physical review letters*, vol. 116, no. 4, p. 043602, 2016.

[36] M. Hofheinz, F. Portier, Q. Baudouin, P. Joyez, D. Vion, P. Bertet, P. Roche, and D. Estève, "Bright side of the coulomb blockade," *Physical review letters*, vol. 106, no. 21, p. 217005, 2011.

[37] G. Gasse, C. Lupien, and B. Reulet, "Observation of squeezing in the electron quantum shot noise of a tunnel junction," *Phys. Rev. Lett.*, vol. 111, p. 136601, Sep 2013.

[38] E. Zakka-Bajjani, J. Dufouleur, N. Coulombel, P. Roche, D. C. Glattli, and F. Portier, "Experimental determination of the statistics of photons emitted by a tunnel junction," *Phys. Rev. Lett.*, vol. 104, p. 206802, May 2010.

[39] J.-C. Forgues, C. Lupien, and B. Reulet, "Experimental violation of bell-like inequalities by electronic shot noise," *Phys. Rev. Lett.*, vol. 114, p. 130403, Apr 2015.

[40] J.-R. Souquet and A. Clerk, "Fock-state stabilization and emission in superconducting circuits using dc-biased josephson junctions," *Physical Review A*, vol. 93, no. 6, p. 060301, 2016.

[41] T. L. Schmidt, A. Nunnenkamp, and C. Bruder, "Microwave-controlled coupling of majorana bound states," *New journal of physics*, vol. 15, no. 2, p. 025043, 2013.

[42] C. Müller, J. Bourassa, and A. Blais, "Detection and manipulation of majorana fermions in circuit qed," *Physical Review B*, vol. 88, no. 23, p. 235401, 2013.

[43] A. Cottet, T. Kontos, and B. Douçot, "Squeezing light with majorana fermions," *Physical Review B*, vol. 88, no. 19, p. 195415, 2013.

[44] C. Ohm and F. Hassler, "Majorana fermions coupled to electromagnetic radiation," *New Journal of Physics*, vol. 16, no. 1, p. 015009, 2014.

[45] Z.-Y. Xue, M. Gong, J. Liu, Y. Hu, S.-L. Zhu, and Z. Wang, "Robust interface between flying and topological qubits," *Sci. Rep.*, vol. 5, no. 12233, 2014.

[46] C. Ohm and F. Hassler, "Microwave readout of majorana qubits," *Physical Review B,* vol. 91, no. 8, p. 085406, 2015.

[47] M. Dartiailh, T. Kontos, B. Douçot, and A. Cottet, "Direct cavity detection of majorana pairs," *arXiv preprint arXiv:1702.01637,* 2017.

9
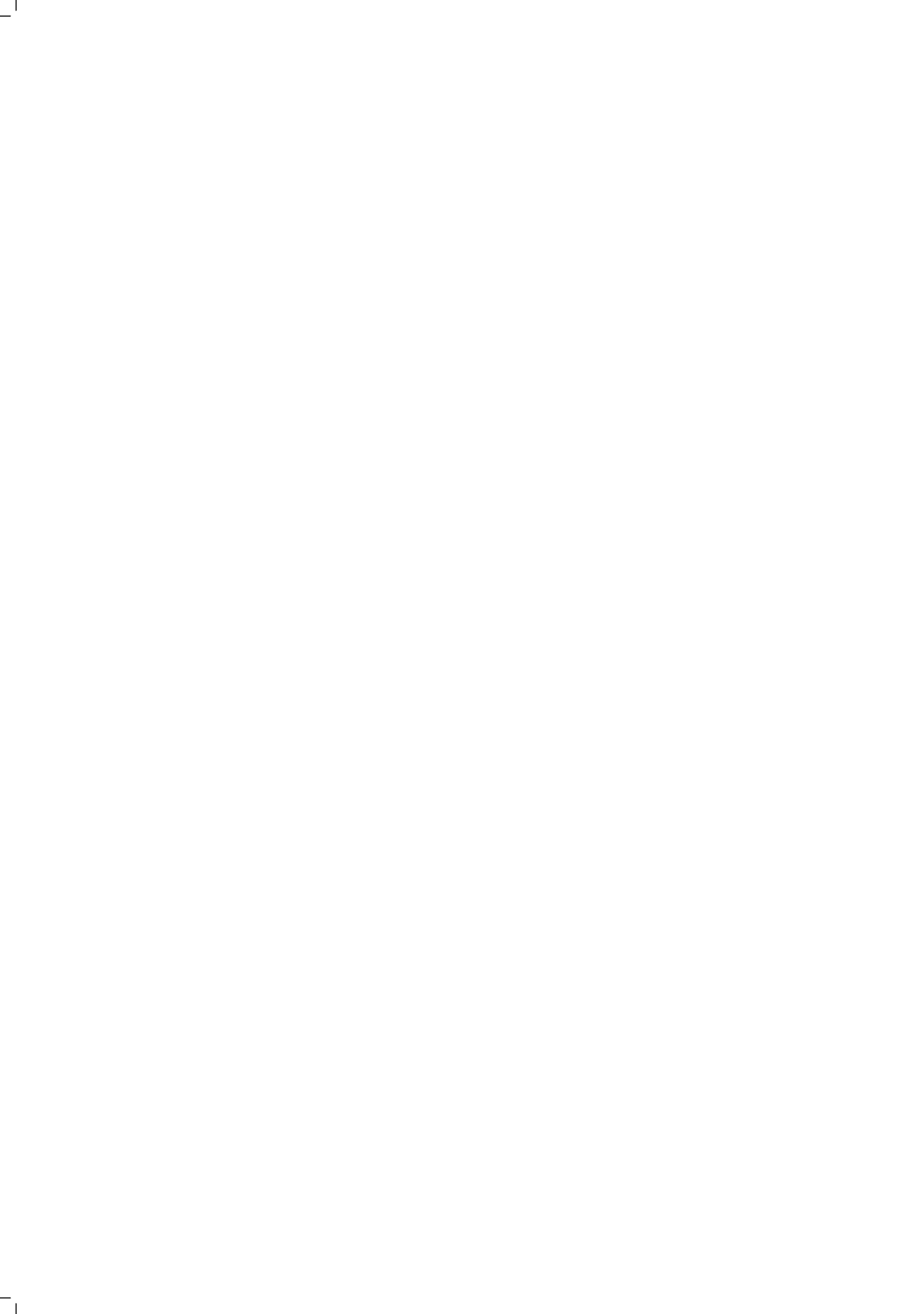
ACKNOWLEDGEMENTS

It is now more than five years ago since I moved to Delft to start my PhD in the spring of 2012. Those years passed by much faster than I would have imagined and taught me a lot about physics and about life. When I started, QuTech was still QT, a enthusiastic but (relatively) small collection of scientists which quickly expanded to the size it is today. The chance to experience and participate in this growth was truly unique and there were many people who supported me in this journey.

Leo, thank you for giving me the opportunity to come to Delft and for providing me with all the resources and the trust to succeed. Your scientific vision and intuiting are remarkable and your ability to inspire scientific and public audiences alike is impressive. Without your contributions QuTech surely would not have been as successful as it is today.

Maja, our collaboration started shortly after the beginning of my PhD, just after you arrived in Delft. Your help and support was invaluable for almost every part of my PhD; from cleanroom and lab techniques, to experiment design, writing, and attempts to find some source for good food on campus. I admire your unstoppable drive, spending almost every free minute in the lab or the cleanroom - even when you were nine months pregnant. I am glad that you found a position back home in Sydney and wish you and your new family all the best.

During the first years I got to spend time in one of the best offices in QT. Arjan, Julia and Önder, thank you for being part of that and for creating a small sanctuary within the sometimes crazy intense world of QuTech. Later this was expanded to the new open office space shared with everyone in the Topo team. By now its size has grown so large that there are too many people to thank everyone individually. All the postdocs, PhD and master students contribute to the atmosphere in the team and I wish you all the best for your future.

Our experiments depend on wires grown in Eindhoven. Eric, Diana, Sebastien and Sasha, it was always a great joy to collaborate and discuss with you. Without your support most of our experiments would be impossible. The input from our theorists is also vital. Michael, thank you for your support and patience when simulating our measurements and explaining the underlying theory. You always have an open door and it is a pleasure to discuss with you. Michal, Bas, and Adriaan, thank you for all the work you contributed.

QuTech has exceptional technical support staff, who ensure that every experiment can keep running day and night. Bram, Jelle, Jason, Mark, Olaf, and Remco, thank you for all your help. Raymond, your knowledge of electronic amazes me as much as your patience and clarity in explaining it. Marja, Yuki, Simone and Jenny, thank you for all the administrative support and your open door whenever I had a question or just wanted to chat. Many thanks to the cleanroom staff at VLL for teaching me and for doing your best to keep the cleanroom open and running.

There were, of course, also many occasions to socialize outside the lab and I am grateful for I all the friends I have found. Önder your scientific skills are as good as your taste in music and I am convinced that you will make a great professor one day, good luck in Boston. Kun, it was a pleasure to share a house with you and to spend most lunchbreaks of the past six months with you, I hope you enjoy living in Japan. Arjan, thank you for your friendship and good luck with your new job. David, you always did your best to create a good atmosphere in the Topo team, thank you for that and enjoy your time in Zürich. Willemijn and Alex, I always greatly enjoyed chatting with both of you and thank you for being my paranymphs and good luck with the rest of your PhDs. James, thank you for taking us to Skye it is a truly beautiful place. Stefan, I always had the most interesting conversations with you, it is good to see that you are also close to finishing. Anais, it was a great joy to teach you lindy hop, hopefully I will now have the time to come and visit you in Montpellier. I also want to thank Basia, Daniel, Hannes, Julia, Maaike, Pasquale, Stijn, Toivo, Tim, Vincent, and all other (former) QT and QuTech members for all the pleasant times.

Soon after arriving in Delft I started to take Lindy hop classes in Rotterdam which turned out to be one of the best decisions I could possibly make. It was the perfect distraction after long days in the cleanroom and the open and welcoming atmosphere of the swing dancing scene in Rotterdam never stops to amaze me. Many thanks to all the people who are involved in creating an maintaining this environment; all the members of Roffaswing, Swing in Rhythm, the students and everyone that I shared a drink, a chat or a dance with over the past years. Niels, thank you for help with proof reading. Zoe, thank you for all the fun classes we taught together and thank you for being a great friend. Ellen, thank you for all your loving support over the past months, hopefully there are more quiet times ahead now.

Zuletzt noch danke an alle meine Freunde und Verwandten in Deutschland. Selbst wenn ich es nur noch unregelmässig zurück schaffe, freue ich mich jedes mal euch zu sehen. Dan und Gloria, danke für eure Freundschaft und alles Gute für eure gemeinsame Zukunft zu dritt. Andrea, Flurina, Uli und Andreas, ihr seid wie eine zweite Familie für mich und habt mir gezeigt wie wahre Stärke aussieht. Ich wünsche euch viel Kraft, Gesundheit und hoffentlich bald wieder bessere Zeiten. Mein besonderer Dank gilt meiner Familie. Heidi, Franz und Lena, ihr habt mich immer unterstützt, mir aber auch den Freiraum gelassen meinen eigenen Weg zu gehen.

Curriculum vitae

Jakob Kammhuber

March, 1987	Born in Burghausen, Germany.
1997 – 2006	Secondary Education: *Kurfürst Maximilian Gymnasium*, Germany (1997 – 1999), *German European School*, Singapore (1999 – 2001), *Aventinus Gymnasium*, Germany (2001 – 2006).
2006 – 2009	B.Sc. Physics, ETH Zürich.
2009 – 2012	M.Sc. Physics, ETH Zürich. Advisor: Prof. dr. Atac Imamoglu, Quantum Photonics Group *'Growth and Optical Measurements of Ultraclean Carbon Nanotubes'*.
2012 – 2017	PhD research, Delft University of Technology Advisor: Prof. dr. ir. L. P. Kouwenhoven, QuTech *'Spin-Orbit Interaction in Ballistic Nanowire Devices'*.

LIST OF PUBLICATIONS

5. M. C. Cassidy, **J. Kammhuber**, D. de Jong, D. Car, S. R. Plissard, E. P. A. M. Bakkers, and L. P. Kouwenhoven *Enhanced charge-cavity coupling in an InSb nanowire quantum dot system*, in preparation.

4. **J. Kammhuber**, M. C. Cassidy, F. Pei, M. P. Nowak, A. Vuik, Ö. Gül, D. Car, S. R. Plissard, E. P. A. M. Bakkers, M. Wimmer and L. P. Kouwenhoven *Conductance through a helical state in an InSb nanowire*, accepted for publication in Nature Communications.

3. M. C. Cassidy, A. Bruno, S. Rubbert, M. Irfan, **J. Kammhuber**, R. N. Schouten, A. R. Akhmerov and L. P. Kouwenhoven *Demonstration of an ac Josephson junction laser*, Science **355**, 6328 (2017).

2. **J. Kammhuber**, M. C. Cassidy, H. Zhang, Ö. Gül, F. Pei, M. W. A. de Moor, B. Nijholt, K. Watanabe, T. Taniguchi, D. Car, S. R. Plissard, E. P. A. M. Bakkers and L. P. Kouwenhoven *Conductance Quantization at Zero Magnetic Field in InSb Nanowires*, Nano Letters **16**, 3482 (2016).

1. S. R. Plissard, I. van Weperen, D. Car, M. A. Immink, **J. Kammhuber**, L. J. Cornelissen, D. B. Szombati, A. Geresdi, S. M. Frolov, L. P. Kouwenhoven and E. P. A. M. Bakkers *Formation and electronic properties of InSb nanocrosses*, Nature Nanotechnology **16**, 859-864 (2013).